Synthesis of novel layered structures for magnetic tunnel junction applications

Jieyuan Song

July 2024

Synthesis of novel layered structures for magnetic tunnel junction applications

Jieyuan Song
Doctoral Program in Engineering Sciences
Subprogram in Materials Science and Engineering

Submitted to the
Degree Programs in Pure and Applied Sciences of the
Graduate School of Science and Technology,
in Partial Fulfillment of the Requirements
for the Degree of Doctor of Philosophy in
Engineering

at the
University of Tsukuba

Table of Contents

Chapter 1 Introduction *1*

1.1 Spintronics and magnetic devices **1**

1.2 Magnetic Tunnel Junctions and Tunnel Magnetoresistance **3**
1.2.1 Basis of tunnel magnetoresistance 3
1.2.2 In-plane MTJ 9
1.2.3 PMA and p-MTJ 17
1.2.4 Non-(001) MTJ 19
1.2.5 (111) MTJ 19

1.3 Spin-charge conversion **26**
1.3.1 Basis of spin-charge conversion 26
1.3.2 Spin orbital torque 27

1.4 Organization of this thesis **28**

Chapter 2 Experimental Methods *30*

2.1 Sample preparation **30**
2.1.1 Magnetron sputtering 30
2.1.2 Electron-beam evaporation 32
2.1.3 Microfabrication 33

2.2 Structural characterization **36**
2.2.1 Atomic force microscopy (AFM) 36
2.2.2 X-ray diffractometry (XRD) 37
2.2.3 Reflection high-energy electron diffraction (RHEED) 38

2.3 Magnetic property measurement **39**
2.3.1 Vibrating sample magnetometer (VSM) 40
2.3.2 Magneto-Optical Kerr Effect (MOKE) 41

2.4 Transport property measurement **41**
2.4.1 Current in-plane tunneling measurement (CIPT) 41
2.4.2 Four probe measurement 42
2.4.3 Unidirectional spin magnetoresistance (USMR) 43
2.4.4 Spin torque ferromagnetic resonance (ST-FMR) 46

Chapter 3 Fully epitaxial fcc(111) magnetic tunnel junctions with a $Co_{90}Fe_{10}$/MgAlO/$Co_{90}Fe_{10}$ structure *47*

3.1 Introduction **47**

3.2 Experiment procedures **48**

3.3 Results and Discussions **53**
3.3.1 Structural properties of $Co_{90}Fe_{10}$/MgAlO/$Co_{90}Fe_{10}$ stack 53
3.3.2 Microstructure analysis of $Co_{90}Fe_{10}$/MgAlO/$Co_{90}Fe_{10}$ stack 57
3.3.3 Transport properties of $Co_{90}Fe_{10}$/MgAlO/$Co_{90}Fe_{10}$ stack 61

3.4 Summary **66**

Chapter 4 Perpendicular Magnetic Tunnel Junctions with a Non-integer Monolayer Controlled CoPt(111) layer and a MgO(111) Barrier *67*

4.1 Introduction **67**

4.2 Experiment procedures **68**

4.3 Results and Discussions **70**
4.3.1 Structural properties with $L1_1$ superlattice of Co/Pt multilayers 70
4.3.2 Magnetic properties of Co/Pt multilayers 74
4.3.3 Structural properties of CoPt/MgO/CoFeB stack 77
4.3.4 Microstructure analysis and transport properties of CoPt/MgO/CoFeB stack 79
4.3.5 Fully fcc(111) perpendicular MTJ with CoPt/MgO/CoPt stack 82

4.4 Summary **83**

Chapter 5 Charge-to-spin conversion in fully epitaxial Ru/Cu hybrid nanolayers with interface control ***85***

5.1 Introduction **85**

5.2 Experiment procedures **86**

5.3 Results and Discussions **88**
5.3.1 Structural properties of Ru/Cu heterostructure 88
5.3.2 USMR measurement 94
5.3.3 ST-FMR measurement 96
5.3.4 Discussion 101

5.4 Summary **102**

Chapter 6 Summary and Outlook ***104***

Reference ***106***

List of publications and presentations ***114***

Acknowledgments ***116***

Chapter 1 Introduction

1.1 Spintronics and magnetic devices

In recent years, there has been a noteworthy memory revolution towards the stimulating cutting-edge technologies such as machine learning, artificial intelligence, and neuromorphic memory device applications et. al.[1,2] An outstanding candidate for the next-generation random access memory (RAM) known as MRAM offers benefits such as non-volatility, lower energy consumption, and high endurance. It works on the principles of spintronics, leveraging the spin characteristic of electrons for effective manipulation of data reading, writing, and storage. [2–4]

In history, since the electronic industry revolution changed the world a hundred years ago along with the boom of the semiconductor technology revolution, a new research field known as spintronics which utilizes spin and electronics draws people's attention with the next-generation trending inventions from memories to processors over the era of modern IoT (Internet of Things) technology. From the viewpoint of spintronics, the electrons' spin and charge are two of the most interesting properties, leading to some fascinating physical effects applied for microscopic functioning and quantum mechanical transporting. Alongside the prosperous electronic industry, the magnetic property rising from the intrinsic spin of electrons will play an important role since its unique contribution to device functionality such as non-volatility and ecologically friendly.

Back in the 1980s, the discovery of the giant magnetoresistance (GMR) effect[5,6] revealed the numerous potentials of spintronics since this novel effect was able to develop the memory industry significantly for the reduction of device sizes towards high-density with better sensitivity as utilized in products such as hard disk drives (HDDs). The storage industry was greatly inspired by

this research and just nine years later in 1997[3], GMR read head was introduced to the world with enhanced performance. This phenomenon describes the resistance difference when an external magnetic field in a multilayer structure is applied, and this multilayer structure consists of a very thin nonmagnetic (NM) layer sandwiched by two magnetic layers. And two independent finders of the GMR effect named Grunberg and Fert were jointly awarded the Nobel Prize in physics back in 2007, which proved the importance of this discovery.

Following the GMR effect, another promising magnetoresistance effect, which will be the most important concept of this thesis, called the tunneling magnetoresistance (TMR) effect with a substantially larger resistance difference value was realized in 1995[7] although this phenomenon was actually observed earlier than the GMR effect (in 1975 by Julliere[8]). Magnetic tunnel junction (MTJ) which consists of a multilayer structure with an insulating layer called a barrier sandwiched by two ferromagnetic (FM) layers is the nanostructure used here for achieving the TMR effect. The magnetization direction between two FM layers has different configurations, such as in the same direction or opposite direction, which are distinguished as parallel (P) state or antiparallel (AP) state. The value of the resistance difference between these two configurations is defined as tunnel magnetoresistance and this value is much larger than the conventional MR from GMR effect. For the application side, MTJ acts as the read head of hard disk drives (HDD) or the memory cells of magnetic random-access memory (MRAM)[9]. Apart from this, MTJ can also be used in some magnetic sensors and microwave devices[1,10]. As for the reading process of MRAM, the binary information such as the “1” state or the “0” state can be stored in these two P or AP states with different resistance. By changing the magnetization direction of one FM layer, the two states can be converted from one to another simply to achieve the writing process. A simple illustration of the development timeline for the spintronic memory device utilizing different

magnetoresistance effects is shown in Fig. 1. Anisotropic magnetoresistance (AMR) describes the changing of resistance from a ferromagnetic material with an intrinsic anisotropy between the angle of current flow and the direction of the magnetization. Following the relatively small MR value of around 1 or 2%, the GMR effect has an MR value of 5 to 15%. With the development of TMR, this value can be increased to over 600% and recently this value was refreshed again as we will introduce in the following content. The development of the TMR effect in MTJ is a promising way with the modern technology boom and the requirement of high performance and low energy consumption can be well satisfied by this phenomenon.

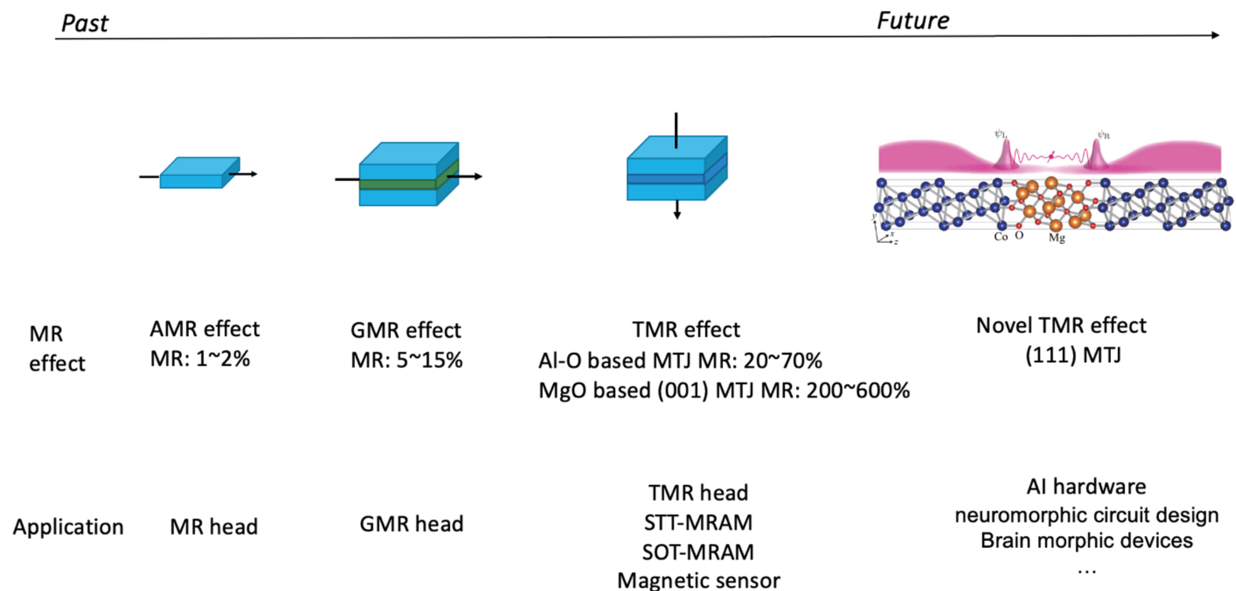

Figure 1.1 Timeline of the development of spintronics application, the picture of (111) MTJ is from[11]

1.2 Magnetic Tunnel Junctions and Tunnel Magnetoresistance

1.2.1 Basis of tunnel magnetoresistance

For understanding the development of TMR and MTJ properties, it is indispensable to learn the basic mechanism of this magnetoresistance effect. A conventional model known as the Julliere model provides a simplified view to understand the basic mechanism and some important concepts that define the TMR value. The description of the Julliere model will be introduced with illustration in the following paragraph and after that, the detailed explanation will be performed with some equations and derivations.

The magnetization of ferromagnetic materials can be explained by the band structure at the Fermi level with the imbalanced amount of majority spin and minority spin of different spin configurations. As illustrated in Fig. 1.2 (a), a large number of up-spin electrons is shown as red color and defined as the majority spin component and a small number of down-spin electrons are defined as the minority spin component with blue color. The color here only represents the spin up or spin down configuration and the majority or minority is the description for the number density of electrons with the same spin orientation. The magnetization direction is consistent with the spin orientation of the majority spin component.

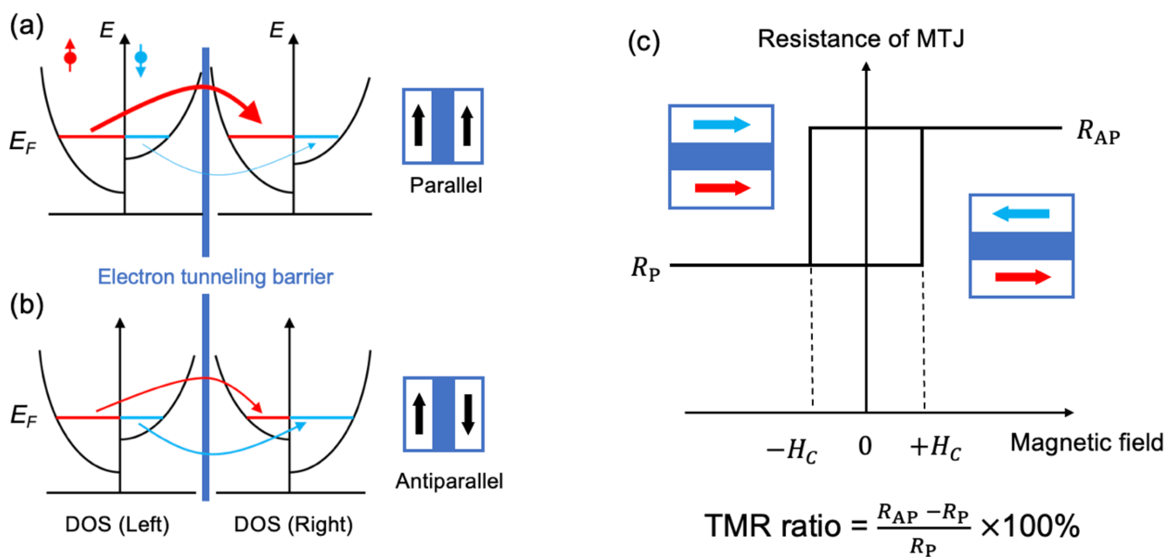

Figure 1.2 (a) Illustration of resistance difference between P and AP state, (b) (c) schematic illustration of Julliere model

There is a principle that most transport properties depend on the density of states (DOS) near the Fermi level (E_F). So we illustrate them in a simple behavior and analyze the transport process of different resistance states. Figure 1.2(a) shows a parallel state of MTJ with both two ferromagnetic layers having the same magnetization direction and both have a majority spin with spin-up orientation (red color). As for Fig. 1.2(b), the right side FM layer reversed the magnetization direction, so the right side of the band structure has a majority spin component with down spin (blue color).

There is an assumption that spin is conserved, which means that tunneling will only occur within electrons of similar spin orientation. In other words, from spin up to up (red color line) and from down to down (blue color line). Now the tunneling process is illustrated by the arrow line and the thickness of these lines here represents the quantity of electrons that are capable of tunneling through the barrier. For the parallel state as shown in Fig. 1.2(a), the consistency of similar orientation tunneling leads to lots of electrons as illustrated by a much thicker red line with up spin configuration and majority spin, which means that lots of electrons can tunnel through the barrier, yields a low electrical resistance.

As for the antiparallel state as shown in Fig. 1.2(b), the left FM layer has a reversed magnetization direction, so the majority spin is not up but down which means the red color electrons states became much smaller. The tunneling will happen from majority to minority (red line for spin-up) and from minority to majority (blue line for spin-down). This leads to either a lack of vacancies (red line with spin up) or a lack of tunneling electrons (blue line with spin down) and yields a much higher electrical resistance. That is the basic mechanism to describe the occurrence of resistance

difference when the MTJ changes from P to AP. A simple resistance curve with changing the external magnetic field (which will change the magnetization direction of the FM layer) is illustrated in Fig. 1.2(c). And the TMR ratio is defined as $(R_{AP} - R_P) / R_P \times 100\%$.

From the Julliere model, the TMR ratio can be further defined as:

$$\mathrm{TMR} = \frac{2P_{\mathrm{L}}P_{\mathrm{R}}}{1 - P_{\mathrm{L}}P_{\mathrm{R}}} \tag{1.1}$$

$$P = \frac{D_{\uparrow}(E_F) - D_{\downarrow}(E_F)}{D_{\uparrow}(E_F) + D_{\downarrow}(E_F)} \tag{1.2}$$

Here P means the spin polarization which describes the normalized difference in the density of states of spin majority band $D_{\uparrow}(E_F)$ and spins minority band $D_{\downarrow}(E_F)$ at the Fermi level E_F. The lower character R means right, L means left. This further revealed that a high spin polarization gives a larger TMR value[8].

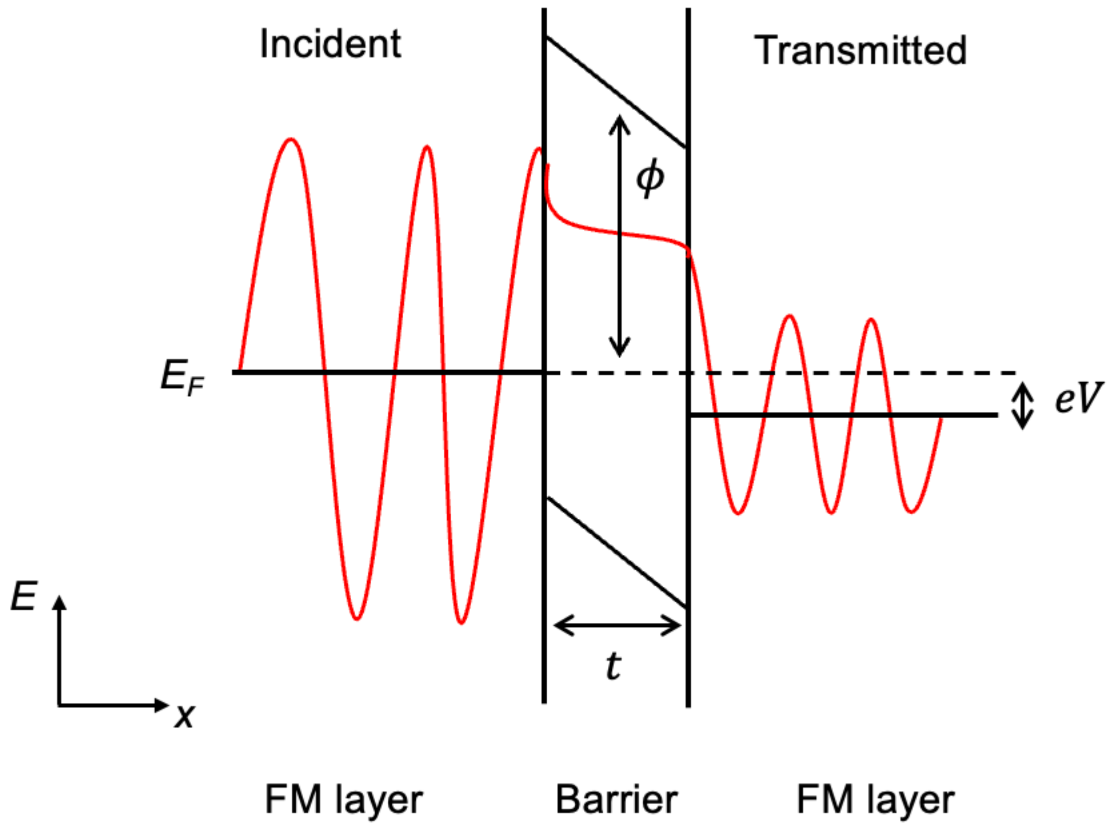

Figure 1.3 Schematic illustration of the tunneling process from the viewpoint of the wave function.

This is a detailed analysis of the physical transport process by utilizing the Wentzel-Kramers-Brilliouin (WKB) approximation. This approximation is valid when potentials varying slowly on the scale of electron wavelength. Now we focus on a tunneling electron and the transmission probability for tunneling through a potential barrier is derived by:

$$T(E) \approx \exp\left(-2\int_0^t \sqrt{\frac{2m_e[U(x)-E]}{\hbar^2}}\,\mathrm{d}x\right) \tag{1.3}$$

Here x direction is perpendicular to the sample surface, which also means that the electron tunnel direction is vertical to the sample surface. E is the electron energy, t is the barrier thickness, m_e is the mass of an electron, $U(x)-E$ is the energy barrier, $\hbar$ is the reduced Planck constant.

As Fig. 1.3 illustrates, we suppose a finite bias voltage V with a lower Fermi level at the right side, and the electrons can elastically tunnel from left to right in the empty state. For the barrier $U(x)$, the potential is assumed to be a constant ϕ over the barrier region, which is also above the Fermi energy. The barrier thickness is supposed to be 1 to 3 nanometers for inducing the tunneling effect in an MTJ structure. So, as we assumed that the electrons tunnel from left to right, the tunneling current can be written as the following formula where N is the density of states (DOS), $f(E)$ is the Fermi-Dirac factors.

$$I_{L\to R}(E) \propto N_L(E-eV)f(E-eV)T(E,V,\phi,t)N_R(E)[1-f(E)] \tag{1.4}$$

Then the total current is given by:

$$I \propto \int_{-\infty}^{+\infty} N_L(E-ev)T(E,V,\phi,t)N_R(E)[f(E-eV)-f(E)]dE \tag{1.5}$$

For a very small voltage compared with the barrier potential ($eV \ll \phi$), only the electrons near the Fermi level (E_F) are considered, and transmission T no longer depends on E and V. The density of state N also is independent of E, then the total current I will be reduced to:

$$I \propto N_L(E_F)N_R(E_F)T(\phi,t)\int_{-\infty}^{+\infty} [f(E-eV)-f(E)]dE \tag{1.6}$$

As for very low-temperature conditions ($k_B T \ll eV$), the integral over the Fermi functions equals eV, then we can get the tunnel conductance as the following expression, which is proportional to the density of states near the Fermi level $N_L(E_F)N_R(E_F)$ and the transmission probability $T(\phi,t)$.

$$G \equiv \mathrm{d}I/\mathrm{d}V \propto N_L(E_F)N_R(E_F)T(\phi,t) \tag{1.7}$$

If we assume the same transmission probability, the conductance (resistance) will only depend on the N_L and N_R. For the parallel state, as we mentioned before, the electrons tunnel from majority to majority and minority to minority, so the conductance will be given by:

$$G_P = G_\uparrow + G_\downarrow \propto N_{maj}^2(E_F) + N_{min}^2(E_F) \tag{1.8}$$

As for the antiparallel state, it will be from majority to minority and vice versa, so the conductance will be given by:

$$G_{AP} = G_\uparrow + G_\downarrow \propto 2N_{maj}(E_F)N_{min}(E_F) \tag{1.9}$$

Then the TMR will be normalized as follows:

$$\text{TMR} \equiv \frac{G_P - G_{AP}}{G_{AP}} = \frac{R_{AP} - R_P}{R_P} = \frac{\left[N_{maj}(E_F) - N_{min}(E_F)\right]^2}{2N_{maj}(E_F)N_{min}(E_F)} = \frac{2P_L P_R}{1 - P_L P_R} \tag{1.10}$$

$$P = \frac{D_\uparrow(E_F) - D_\downarrow(E_F)}{D_\uparrow(E_F) + D_\downarrow(E_F)} \tag{1.11}$$

That is how we can derive the classic explanation for the TMR effect by the Julliere model[3].

1.2.2 In-plane MTJ

Up to now, we understand the basic knowledge of the TMR effect. For the development of the TMR ratio, a lot of effort was made in history. In the beginning, in-plane MTJ was utilized for the realization of giant TMR ratio which has the magnetization direction parallel to the plane of the MTJ thin film stack. The first milestone was established by the discovery of a coherent tunneling mechanism in bcc (001) crystalline MTJ structure with Fe, CoFe, and CoFeB as a ferromagnetic layer and MgO as a barrier layer. Up to now, this mechanism is still the conventional way to induce the effective TMR ratio with almost no other competitor until the discovery of Co-based (111)

MTJ with interfacial induced giant TMR mechanism which is the main theoretical guidance followed by this thesis work. The theory of (111) MTJ will be introduced in chapter 1.2.5. To understand this kind of unique mechanism, it is necessary to start from the general amorphous MTJ with aluminum oxide barrier materials.

In the beginning, the preliminary MTJ stacks were made with aluminum oxide (Al-O) as a barrier material because of the simplicity of the fabrication process. The Al-O barrier material was always grown in amorphous structure and the TMR ratio is over 10% at room temperature which is not so bad at that moment[7,12]. Following this kind of study, several methods such as using CoFeB as a ferromagnetic layer increased the TMR value to 70% by using CoFeB as reported in 2004[13]. Nevertheless, it was rather difficult for this amorphous barrier since the theoretical calculation did not prove any giant TMR effect possibly exhibited and only incoherent tunneling exists in these structures. Later, the discovery of coherent tunneling greatly reveals the possibility of a giant TMR effect by crystal orientation-determined tunneling mechanism with high crystallinity MTJ structure.

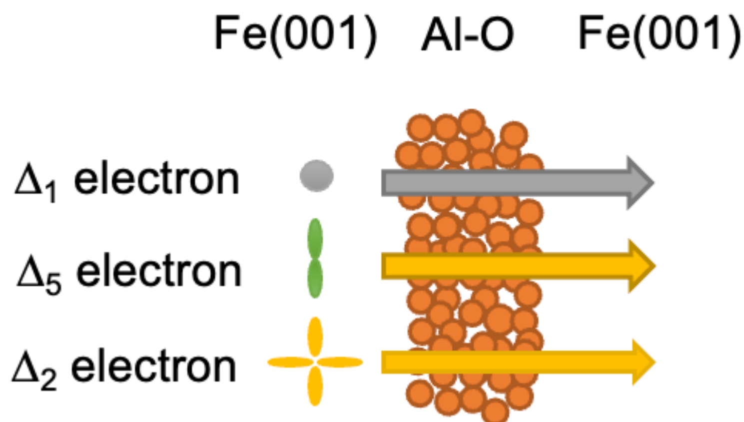

Figure 1.4 Schematic illustrations of amorphous Al-O barrier MTJ tunneling effect.

As an example, a schematic illustration of a Fe (001)/amorphous Al-O/Fe (001) MTJ structure with tunneling behavior was shown in Fig. 1.4. Since Fe is a 3d ferromagnet, it has various electron states with different symmetric property. These different wavefunctions in different Bloch states are named as Δ_1, Δ_5, and Δ_2. From Julliere's model, the spin polarization is the most important factor that defines the TMR value and only the density of states at the Fermi level should be considered. Here the incoherent tunneling in this amorphous Al-O MTJ means that the tunneling probabilities of each electron state are equal and have identical contributions. All these electrons can couple with the evanescent states in the Al-O barrier when they tunnel through. However, the theoretical study revealed that in this amorphous barrier without any crystallographic symmetry, the electrons in different Bloch states have different tunneling probabilities. For instance, the Δ_1 state with a large positive *P* value has a higher tunneling probability, but the Δ_2 states with negative *P* also contribute to the tunneling process and totally will reduce the final spin polarization *P*'s value. In conclusion, the final *P* value is defined by the combination of different electron states in different Bloch states, and the states with negative *P* reduce the total spin polarization which definitely inhibits a larger TMR value[1].

Then we can introduce the surprising effect of the coherent tunneling which yields a significant giant TMR value theoretically and experimentally from the bcc (001) MTJs[14,15]. As Figure 1.5 shows, the lattice mismatch between MgO as a barrier material epitaxially deposited on bcc (001) Fe is rather small when a 45° rotation exists between these two layers.

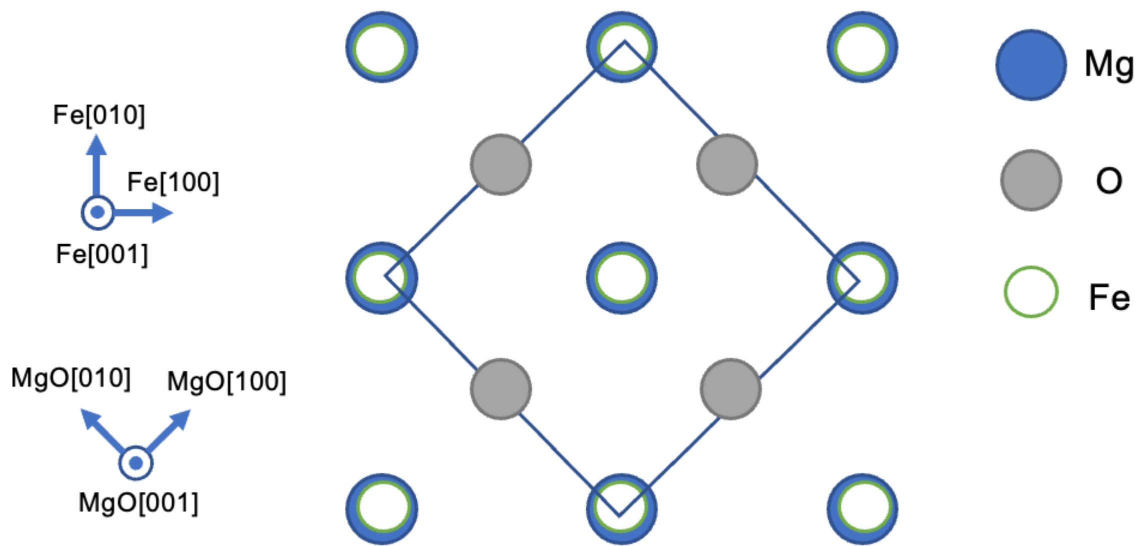

Figure 1.5 Crystallographic relationship of epitaxial Fe(001)/MgO(001), adapted from[1].

Then, we will discuss the coherent tunneling mechanism in this bcc (001) Fe/MgO/Fe epitaxial MTJ stack from the viewpoint of the band structure. Only the Δ_1 band electron coherently tunnels through the barrier and the dominant influence from this Δ_1 band is the fully spin-polarized band structure at the Fermi level, so a giant TMR is predicted ideally.

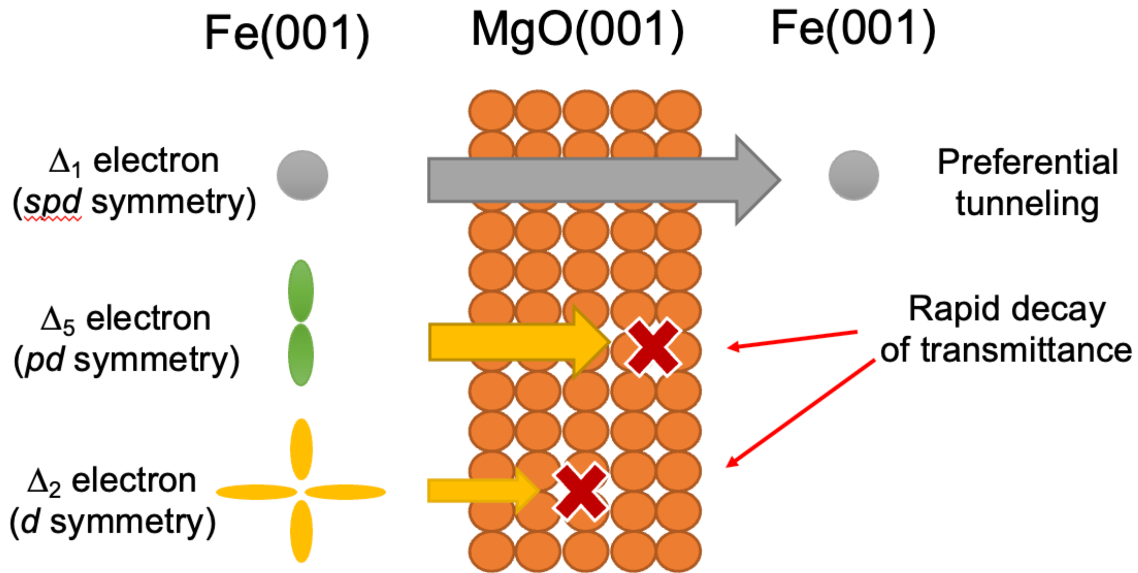

Figure 1.6 Schematic illustrations of tunneling effect in bcc (001) Fe/MgO/Fe MTJ.

As illustrated by Fig. 1.6, at the $k_{\parallel} = 0$ (in this case is [001] direction), there are three evanescent states in the bandgap of MgO (001) known as Δ_1, Δ_5, and Δ_2 with different symmetry behavior. Since the symmetries of the wave functions are conserved, each Bloch state of Fe (001) and MgO (001) are coupled such that Fe Δ_1 will be coupled with MgO Δ_1. By the first principle calculation shown in Fig. 1.7(a), the transmittance of Δ_5 electrons and Δ_2 electrons decay rapidly which means that they can hardly tunnel through the barrier and have negligible influence on the tunneling process. This leads to that only Δ_1 electrons dominantly tunnel through the barrier. So we should only focus on the band structure of this electron. As shown in Fig. 1.7(b) of the band dispersion of bcc Fe in the [001] direction, for the Δ_1 state at the Fermi level, only up spin has a finite value and down spin does not occur at the Fermi level. This is a half-metallic fully spin-polarized behavior and the theoretical spin polarization $P = 1$ for this kind of situation, which means an enormous TMR value is expected and this bcc (001) structure can yield a significantly larger TMR ratio.

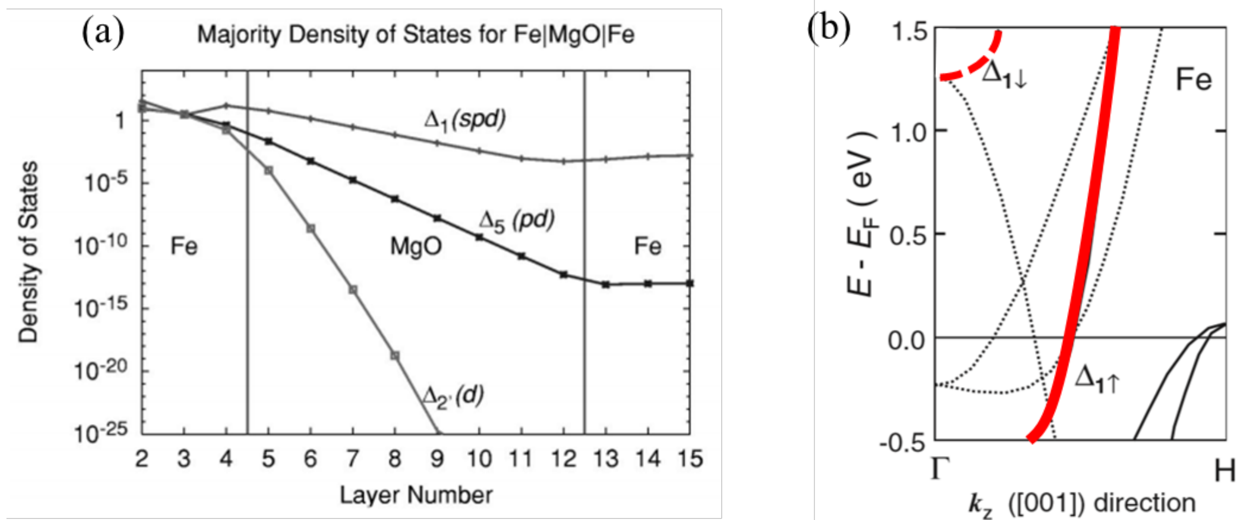

Figure 1.7 (a) Tunneling DOS of spin majority for $k_{\parallel} = 0$ in P state of Fe(001)/MgO(001)/Fe(001)[14], (b) Band dispersion of Fe in [001] direction. The red solid line represents the spin majority in Δ_1 state, and the red dashed line represents the spin minority in Δ_1 state (adapted from[16]).

Further calculation can be simply introduced as the following expression. In Chapter 1.2.1 we derived the transmission probability equation that when $\mathbf{k}_{\parallel} = 0$, it can be given by:

$$T(E) \approx \exp\left(-2\int_0^t \sqrt{\frac{2m_e[U(x)-E]}{\hbar^2}}\,\mathrm{d}x\right) \tag{1.12}$$

Considering the importance of the in-plane wave vector $\mathbf{k}_{\parallel} = (k_x,\ k_y)$ for defining the scattering states, the transmission probability should be written as:

$$T(E) = \exp\left(-2\int_0^t \sqrt{\frac{2m_e[U(x)-E]}{\hbar^2} + \mathbf{k}_{\parallel}^2}\ \mathrm{d}x\right) \tag{1.13}$$

For bcc (001) MTJ, Butler et al.[14] derived the Landauer formula for the conductance as follows:

$$G = \frac{e^2}{h}\sum_{\mathbf{k}_{\parallel},j} T(\mathbf{k}_{\parallel}, j) \tag{1.14}$$

Then he calculated the tunneling probability with the $\mathbf{k}_{\parallel}$ wave vectors distribution as shown in Fig 1.8. This is clear evidence of the giant TMR effect from the coherent tunneling mechanism. It is obvious that in the parallel state of MTJ, the majority spin band has a very high tunneling probability at $\mathbf{k}_{\parallel} = (0, 0)$ (Fig. 1.8(a)) which is attributed to the Δ_1 coherent tunneling in the majority spin band. In Fig. 1.8(b), the probability is distributed through the $\mathbf{k}$ plane, exhibiting some small tunneling probability. As for the antiparallel state, despite the existence of some finite tunneling currents as shown in Fig. 1.8(c), the conductance of the AP state is much smaller than the P state and a giant TMR value can be deduced by this kind of distribution. This is the theoretical study of the giant TMR mechanism known as coherent tunneling from the bcc (001) MTJ structure.

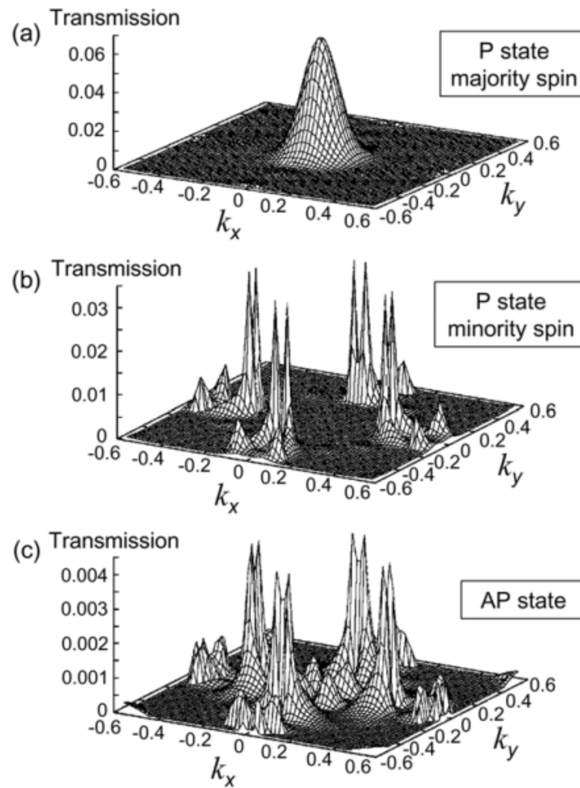

Figure 1.8 Tunneling probability in a Fe(001)/MgO(001)/Fe(001) MTJ as a function of $\mathbf{k}_{\parallel} = (\boldsymbol{k_x},\ \boldsymbol{k_y})$wave vector. (a) Spin majority conductance in the P state, (b) spin minority conductance in the P state, (c) conductance in the AP state, reproduced from[1].

In the experiment work, the enhanced TMR value was consistently observed by utilizing such giant TMR mechanism with bcc Fe, CoFe, and CoFeB as ferromagnetic layers with MgO or Mg-Al-O as a barrier material. The preliminary observation was conducted by Yuasa et al.[17] with fabricated the Fe(001)/MgO(001)/Fe(001) by MBE method and the TMR value was up to 180% at RT. This is a significant enhancement compared with the amorphous Al-O MTJ and proves the coherent tunneling mechanism existed in this kind of structure. Recently Scheike et al.[18] doubled this record for Fe/MgO/Fe MTJ with a precisely optimized deposition process and interface control by combining the magnetron sputtering with the electron beam evaporation method only for the barrier layer. In detail, a high-quality buffer layer with a flat surface and narrow rocking curve provides an enhanced TMR value of 417% and a thin CoFe insertion layer increases this result to 496%. This enhancement was realized with the achievement of atomically sharp interfaces. As for the technique of employment of CoFeB as an amorphous template for MgO (001) growth, which can main the coherent tunneling mechanism with a highly textured MgO(001) barrier layer and after annealing the CoFeB was crystallized to a bcc(001) structure.[19,20] This structure provides the maximum TMR value as a record and was refreshed by Scheike et al. in a CoFe/MgO/CoFe with a TMR value of 631% at RT in 2023.[21] This is the current largest TMR ratio in the experiment. (until June 2024). However, it took over 10 years to break the last record and there is still a large discrepancy between the experimental value and the theoretical value which is over ten thousand percent.

$MgAl_2O_4$ with spinel structure is also chosen in the conventional (001) MTJ due to the improved lattice matching with the FM materials (less than 1%) compared with Fe/MgO (3.8%) as we mentioned before. A large TMR ratio of over 300% at RT was reported in the epitaxial $MgAl_2O_4$ MTJs.[22,23] The coherent tunneling is still effective due to the tunneling process through the D_1

state.[24,25] The spinel materials have the advantage that by tuning the composition between Mg and Al, the lattice constant can be adjusted and from this point of view, it is also suitable for (111) MTJ fabrication. Further development with $Mg_4Al\text{-}O_x$ for perfect lattice matching structure yielded a TMR ratio of 429% at RT (1034% at LT) in Fe/$Mg_4Al\text{-}O_x$/Fe(001) MTJ.[26] This is also the most recent record for Mg-Al-O barrier MTJ.

The TMR value was enhanced by utilizing the coherent tunneling mechanism from bcc (001) MTJ structure and the development from in-plane CoFe/MgO-based MTJ reached over 600%. Nevertheless, for applications such as MRAM, the in-plane magnetization was not usable due to the small anisotropy energy and the decreased thermal stability with decreasing the aspect ratio, which inhibits the in-plane MTJ downscaling to smaller than 50 ~ 60 nm size[4]. With the development of the semiconductor industry with the reduction of memory elements to several nanometers, it is indispensable to realize the giant TMR effect in perpendicular magnetic anisotropy (PMA) MTJ. This part will be discussed in the following chapter.

1.2.3 PMA and p-MTJ

As we just mentioned, the magnetization direction of the FM layers in an MTJ is along the in-plane direction. With the development of magnetic anisotropy, there is an important phenomenon called perpendicular magnetic anisotropy (PMA) which describes the easy axis of the magnetization direction perpendicular to the sample's surface. This effect is desirable for a better performance MRAM. For instance, it can retain high thermal stability in some ultrahigh-density MRAM due to the larger anisotropy energy density, reduce the critical current of magnetization switching[27] , and lower the write error rate in some voltage-controlled MRAM[28]. The thermal

stability factor was defined as $\Delta = E/k_B T$, where E is the energy barrier which is defined by $E = K_u V$, k_B is the Boltzmann constant, and T is the temperature. Here K_u is the anisotropy energy density, and V is the volume of the free layer. As the downscaling of the junction size, V will decrease which decreases the thermal stability and a large value of K_u is indispensable for the realization of better thermal stability. The realization of PMA along with a large TMR effect in MTJ is indispensable, especially for downscaling the current memory element size below 10 nm with stable thermal stability at a working temperature between 350 ~ 400 °C[1,29–31]. This demonstration of perpendicular MTJ is established by interface-induced PMA from (001)-type CoFeB/MgO/CoFeB structure or bulk PMA of fcc(111)-based multilayers such as Co/Pt and Co/Pd.[32–34]

As we just mentioned, normally there are two ways to achieve the PMA effect in MTJs. One is to use some ferromagnets with strong bulk magnetocrystalline anisotropy from the FM layers. In the traditional (001) MTJ, some ordered alloys like $L1_0$ FePt [35,36] or MnGa[37] are fabricated with large PMA along the (001) direction but the TMR value is not large due to the impedance of the coherent tunneling. Another way is to use the interfacial PMA in the (001) MTJ with coherent tunneling. This interface-induced PMA is explained by the hybridization from the Fe orbital and MgO orbital[38]. Ikeda et al.[39] realized the CoFeB/MgO/CoFeB MTJ with a relatively large interface-induced PMA as 1.3mJ/m^2 with more than 120% TMR at room temperature. However, this interfacial effect is very sensitive to the oxidation condition because it is the interface effect[40,41] and the thickness of the FM layer which was observed experimentally[39]. This leads to the difficulty of controlling the interface-induced PMA effect steadily. In conclusion, in the application of p-MTJ, bulk PMA is promising but difficult to use in the traditional (001) MTJ, this discrepancy

leads to the requirement for some novel TMR mechanism apart from the conventional (001) MTJ structure.

1.2.4 Non-(001) MTJ

In history, since the promising giant TMR value was derived by the coherent tunneling mechanism in (001) oriented MTJs, researchers always focused on this direction and optimized this material system on the composition and growth techniques for better crystal structure and reduced defects. Besides this, there are few previous studies about non (001) orientation MTJs and they used the MgO (111) orientation as the barrier layer. Hauch et al. [42] fabricated epitaxially Fe(110)/MgO(111)/Fe(110) MTJ with a three-dimensional island growth from MgO and the surface morphology of the MgO has a grain-like structure. They reported with 28% TMR value at room temperature and by theoretical analysis, this value is consistent with the estimated spin polarization due to the partial spin filtering in the Σ_1 state. Another work was done by Ontake et al. [43] fabricated epitaxially CoPt/MgO/CoPt along the (111) direction and only two (111) variants were observed but still, nice epitaxial growth was revealed by microstructure analysis. Due to the metastable $L1_1$ structure of the CoPt layer, the sample has a PMA effect. But there is no TMR value given and from the magnetization curves, there is no AP state from this stack in this study. The lack of a giant TMR mechanism and technical engineering method inhibit the development of TMR apart from the conventional bcc (001) MTJ and it is necessary to find a novel mechanism and demonstrate the new structure with precisely controlled fabrication techniques.

1.2.5 (111) MTJ

As we discussed before, the requirement for large TMR and PMA effect is indispensable for current MRAM development with MTJ as the memory cell and the conventional (001) MTJ have several issues that remain. Although the record of the TMR value is much larger than the previous one, it seems difficult to improve it further, especially for room-temperature applications. Nevertheless, the layering of various lattice systems, i.e., bcc-FM layer/fcc-type oxide barrier/bcc-FM layer, where an in-plane 45° rotation is required, considerably inhibits the MTJ stack design as shown in Fig. 1.13(a). Besides, for the perpendicular MTJ stack with bcc (001) MTJ structure, the pinned layer which has a fixed magnetization orientation always needs to utilize an fcc (111) Co/Pt or Co/Pd multilayers structure with Ru insertion as a synthetic antiferromagnetic (SAF) layer. Between the (111) stack and (001) stack a texture-breaking layer such as W or Ta are necessary. The difficulty of this breaking symmetry of crystallographic structure but coupled magnetically always makes the fabrication rather complicated because of the mixing between a four-fold (001) structure and a three-fold (111) structure[28,31,32]. The sensitive interfacial PMA with less fabrication stability also restrains the development from the perpendicular MTJ of (001) coherent tunneling. Consequently, novel MTJ structures with advanced mechanisms combining superior TMR and PMA are requisite for the next-generation MRAM magnetoresistive elements.

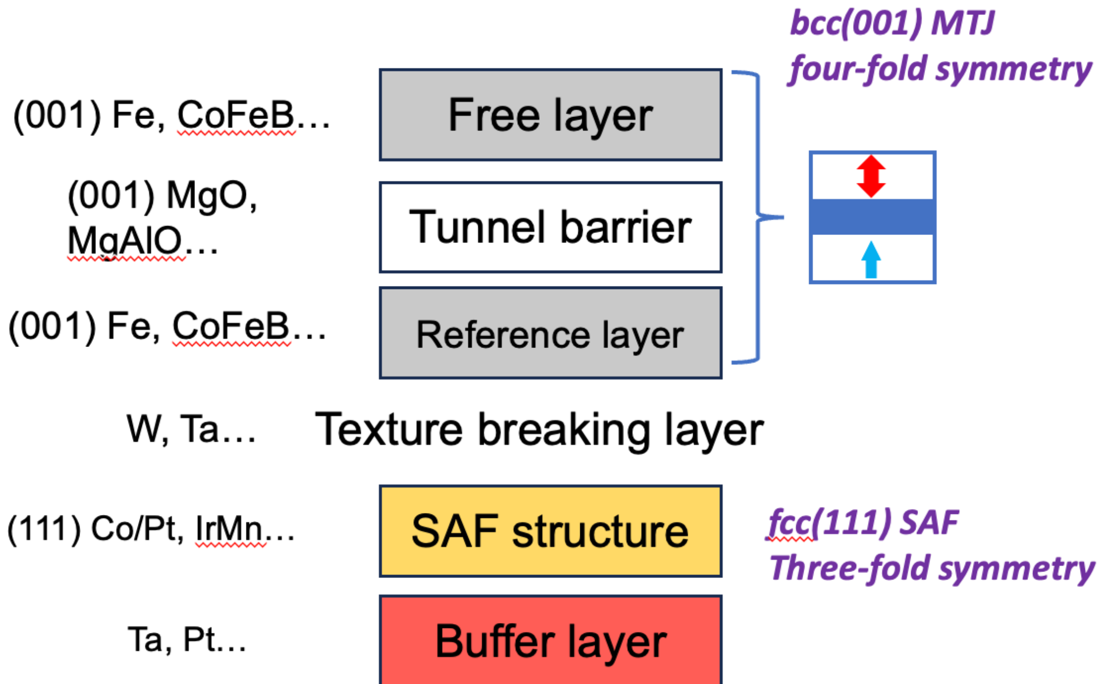

Figure 1.9 Illustration of a conventional (001) perpendicular MTJ stack

Recently, a new concept named fcc (111) MTJ with large TMR combing a bulk PMA effect has given promising advantages and application potential. The mechanism behind this structure with a large TMR ratio is called interface resonant tunneling arising from the interfacial *d-p* antibonding at the Fermi level. The PMA effect arises from the bulk anisotropy induced by some Co-based $L1_1$ materials. Masuda et al.[11] calculated the TMR ratio in the Co/MgO/Co(111) supercells and found the TMR value is over 2000%. Then they also analyzed some $L1_1$ alloys with large bulk PMA energy like CoPt/MgO/CoPt(111) and the theoretical TMR value is also as large as over 2000% with PMA energy predicted theoretically of 10 MJ/m^3. Large TMR and large PMA are both realized in this novel (111)-oriented MTJ structure.[44]

The detailed explanation for this novel fcc (111) MTJ theoretical prediction will be shortly discussed here. Masuda et al.[11,44] performed the first principle calculations based on the density functional theory (DFT) and the Landauer formula[14] and calculated the transport properties such

as the conductance and TMR values. The supercell of Co/MgO/Co(111) is prepared as Figure 1.10 shows. The (111) direction in a close-packed structure with the lowest surface energy for metallic fcc lattice so it is natural to consider this structure. The Co-O interface is chosen because it is the energetically favorite state instead of Co-Mg.

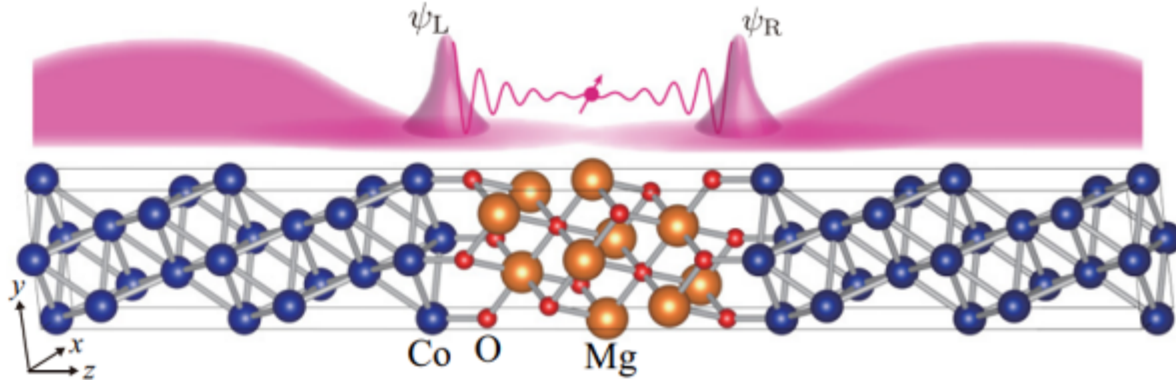

Figure 1.10 Supercells of Co/MgO/Co(111) with the schematics for the TMR effects in the MTJ, adapted from[11].

The local electronic structure and the transmittance were analyzed to clarify the origin of such a large TMR value. The theoretically calculated conductance yield to TMR ratio = 2130% in the Co/MgO/Co(111) structure by TMR ratio $= 100 \times (G_P - G_{AP})/G_{AP}$, where $G_{P(AP)} = G_{P(AP),\uparrow} + G_{AP(P),\downarrow}$. The average conductance is calculated by $G_{P,\uparrow} = \sum_{\mathbf{k}_\parallel} G_{P,\uparrow}(\mathbf{k}_\parallel)/N$, in which $G_{P,\uparrow}(\mathbf{k}_\parallel)$, $G_{P,\downarrow}(\mathbf{k}_\parallel)$, $G_{AP,\uparrow}(\mathbf{k}_\parallel)$, $G_{AP,\downarrow}(\mathbf{k}_\parallel)$ are the in-plane wave vector $\mathbf{k}_\parallel = (k_x,\ k_y)$ resolved conductance with the up (down) arrow indicating the spin majority (minority) in the parallel and antiparallel states, and N is the sampling number of $\mathbf{k}_\parallel$ points.

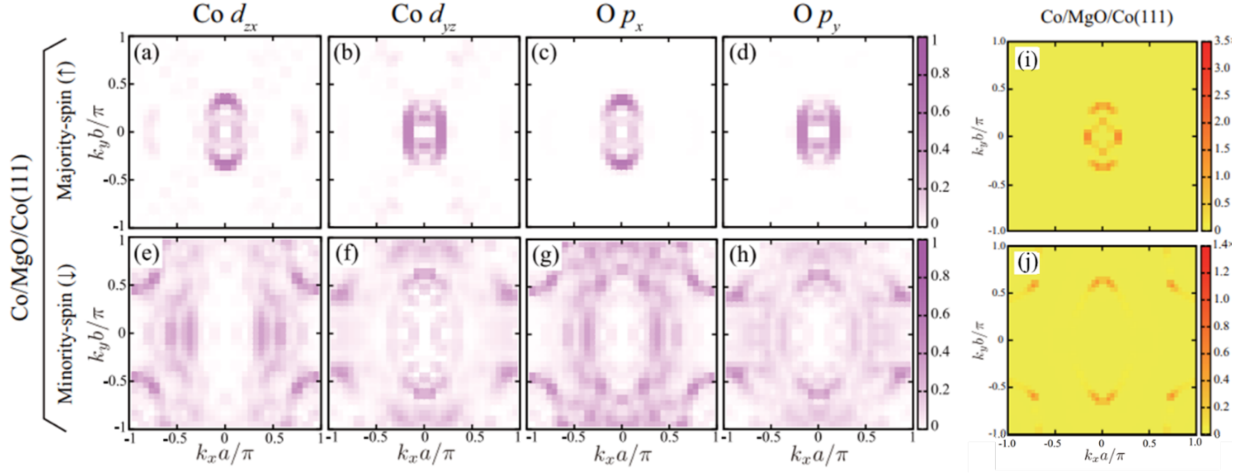

Figure 1.11 The normalized $\mathbf{k}_{\parallel}$ resolved LDOS at Fermi level of interfacial atoms in Co/MgO/Co(111). (a)-(d) are the contributions from Co d_{zx}, d_{yz}, p_x and p_y orbitals in the spin majority state and (e)-(h) are the spin minority state. And the $\mathbf{k}_{\parallel}$ dependencies of conductance in (i) spin Majority $G_{P,\uparrow}(\mathbf{k}_{\parallel})$ and (j) spin minority $G_{P,\downarrow}(\mathbf{k}_{\parallel})$ for the parallel states of MTJ. (Adapted from [11])

The possible explanation for the giant TMR mechanism can be explained by the interface resonant tunneling from the *d-p* antibonding between interface Co and O. From Figure 1.11, there is the almost same behavior of the distribution of the normalized $\mathbf{k}_{\parallel}$ resolved LDOS at Fermi level as shown in Fig. 1.11(a) and (c), (b) and (d) which is antibonding of *d* and *p* orbitals between Co-O. The combination of the LDOS distribution (1.10(a)-(d)) can reproduce the conductance distribution as shown in Figure 1.11(i), which is dominant for the final TMR value from the previous equation with the relationship between the TMR and the conductance. This is clear evidence for showing the relationship between them. Another piece of evidence is the energy dependence of the transmittance in Figure 1.12 with a narrow peak at the Fermi level originating from the interfacial resonant effect.[45–47]

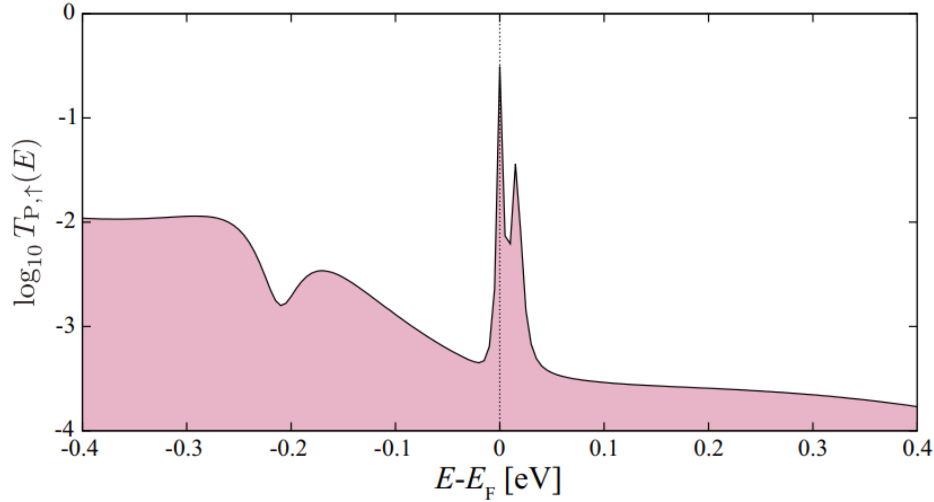

Figure 1.12 The energy dependence of the spin majority transmittance at ($k_x a/\pi$, $k_y b/\pi$) = (0.04, 0.32) in the parallel state of Co/MgO/Co (111) MTJ, adapted from[11].

Masuda et al.[44] also predicted not only the large TMR value but also large PMA energy in some $L1_1$ Co-based materials like CoPt or CoNi with (111) orientation. This novel structure is promising for the development of both TMR effect with PMA energy and the demonstration for this structure was yet to be done experimentally. In this study, the main part of the research result is the first demonstration of the fully epitaxial fcc (111) MTJ following the theoretical study's guidance with technical process optimization and precise characterization.

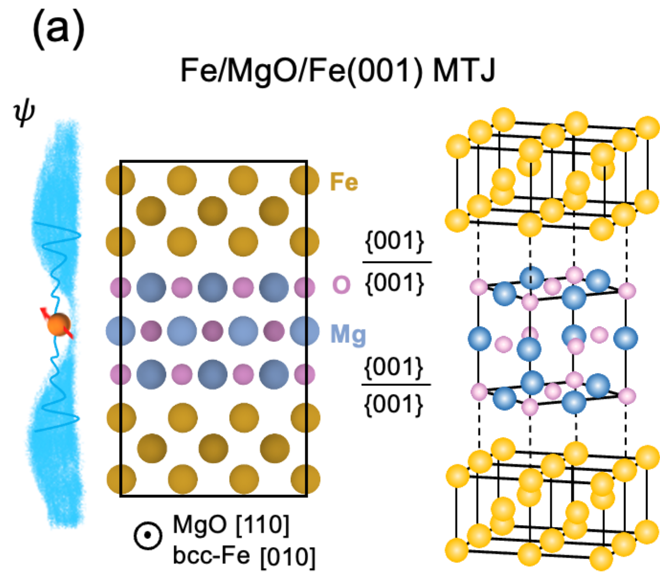

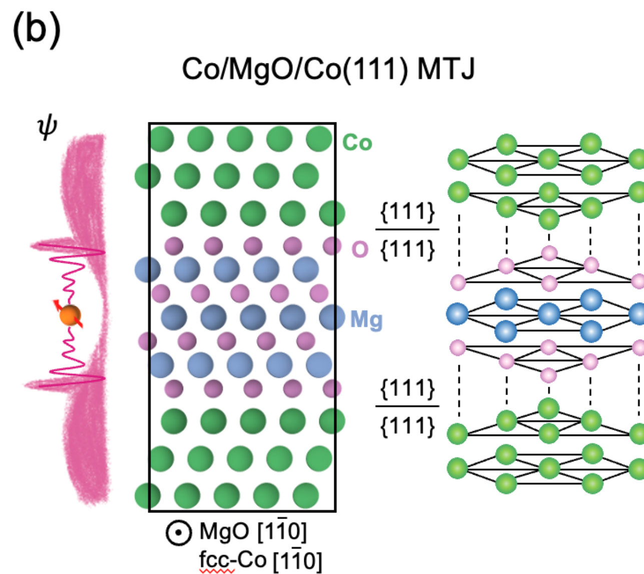

Figure. 1.13 Concept of fcc(111) MTJ. Illustration of crystallographic relationships of (a) conventional bcc Fe/MgO/Fe(001) and (b) fcc Co/MgO/Co(111) MTJ. The theoretical TMR mechanism of the Fe/MgO/Fe(001) is based on *bulk coherent tunneling*, while that of the Co/MgO/Co(111) is based on *interfacial resonance tunneling*, adapted from[48].

Since the conventional bcc (001) MTJ structure has a crystallographic mixture between (001) coherent tunneling material system towards giant TMR application and (111) texture film with perpendicular pinned layer. As Figure 1.13 shows, this kind of structure is rather complicated for further development. Further issues of bcc (001) perpendicular MTJ is that the interface-induced PMA is sensitive to the interface condition and the thickness of the FM layer which also hinders the combination of giant TMR with strong PMA effect. In conclusion, the (111) MTJs with various $L1_1$ materials are proven to have both large TMR and large PMA effects. From the basic Co/MgO/Co(111) to CoPt/MgO/CoPt(111), this is a new direction for the development of magnetic tunnel junctions for the next generation of spintronic applications.

1.3 Spin-charge conversion

1.3.1 Basis of spin-charge conversion

Spin-charge conversion is described by a procedure in which a flow of spin angular momentum, i.e., spin current (SC), is converted into a flow of electric charge i.e., charge current, or vice versa. This process is demonstrated by the spin-orbit interactions (SOIs), which utilize the spin and orbital degrees of freedom in a material. [49–53] Manipulation of the spin-charge conversion is essential for the development of energy-efficient spintronic devices such as magnetoresistive random access memories (MRAMs) [4,54], spin-orbit oscillators [55,56], and spin-orbital magnetoresistance sensors. [57] Demonstrating the spin-charge conversion, especially with enhanced spin Hall efficiency, which quantifies the process of spin-charge conversion, is significantly important for better-switching efficiency towards next-generation MRAM development such as the energy-efficient spintronic devices such as spin-orbital torque (SOT) based magnetoresistive random access memories (SOT-MRAM).

1.3.2 Spin orbital torque

Besides the data storage from the TMR effect utilizing the different magnetization states between two magnetic layers, how to switch the magnetization direction of each layer inside the MTJ is also important which is called the magnetization switching related to the writing procedure inside the MRAM system. In terms of the writing procedure, it is required an efficient switching for the magnetization direction of the FM layer. Progressing from the current-induced field switching to spin transfer torque (STT), the most recent advanced approach was spin-orbital torque (SOT) switching, which offers better energy efficiency, reliability, and flexibility.

A spin current can be produced through spin-orbit effects, such as the spin Hall effect (SHE), within the NM layer when a charge current is applied. The generation and detection of spin current is one of the most important processes in spin-charge conversion. In nonmagnetic material (NM)/ferromagnetic material (FM) heterostructures, a spin current can be generated by the so-called spin-orbit effects, e.g., the spin Hall effect (SHE). When the spin current is injected into the FM layer, it can exert a torque on the magnetization of the FM layer, so-called spin-orbital torque (SOT), resulting in efficient magnetization switching with low energy consumption. [58–61] This part can also be explained as the writing process for the principle of MRMA also known as magnetization switching which means the changing of the magnetization direction of the FM layer of the MTJ element by several methods including the SOT switching.

The conversion efficiency of SOT is important and typically, 5*d* heavy metals such as Ta [54,62–64], Pt [67,6865–67], W [68,69], or some topological insulators such as Bi_2Se_3 are well-known with large charge-to-spin conversion efficiency. However, they do have some drawbacks such as unstable

phases, high cost, or low conductivity. Therefore, the exploration of novel materials systems such as nanolayered structures or engineered interfaces within highly conductive materials is desirable.

1.4 Organization of this thesis

With the development for next generation memory systems especially the most advanced SOT-MRAM application, the conventional bcc (001) MTJ structure always suffered from its magnetic coupled but crystallographic mixture between (001) MTJ stack and (111) synthetic antiferromagnetic structure for pinning and stabilizing. The theoretical study proposed a new concept called fcc (111) MTJ with giant TMR and strong bulk PMA effect but the experimental demonstration was yet to be done. As for the writing procedure, the high resistivity of heavy metal also constrains the industrial application which lets the high conductivity material system with nano-level engineering for high spin Hall efficiency draw researchers' attention.

The purpose of this study is to develop the novel layered structure of (111) orientation thin films for MTJ and SOT application. In this work, we developed epitaxial thin films of fcc (111) material system based on a high-quality Ru underlayer on sapphire substrate with epitaxial fcc (111) materials including CoFe/Mg-Al-O/CoFe, CoPt/MgO and Ru/Cu material system. The main part is the first demonstration of fcc (111) MTJ with carefully engineered layer structure and optimized growth conditions.

In Chapter 2, experimental procedures used in this study are introduced.

In Chapter 3, an fcc(111)-type MTJ using a fully epitaxial $Co_{90}Fe_{10}/Mg_4Al\text{-}O_x$/CoFe structure with relatively flat interfaces was observed with periodic misfit dislocations at CoFe/MAO interface to minimize their large lattice mismatch (~19%). A TMR ratio of 37% at RT (47% at 10 K) was

achieved with symmetric TMR-H curves indicating the well-balanced CoFe/MAO interface. This is the first demonstration of a fully fcc (111) MTJ with TMR value reported and the microstructure and transport properties were discussed.

In Chapter 4, a multilayer method in a co-sputter chamber was performed to fabricate the Co/Pt layered structure, and non-integer monolayer controlled superlattice behavior with different Co/Pt components was discussed from a peak splitting XRD out-of-plane spectrum. This indicates the well-defined layer-by-layer growth with atomically sharp interface which is desirable for MTJ stack fabrication. Then a CoPt/MgO/CoFeB p-MTJ was fabricated and characterized with a TMR value of 24% at RT. The lattice mismatch here was reduced compared with the in-plane MTJ shown in Chapter 3 together with the large PMA of 1 MJ/m^3 from Co/Pt multilayer. Then the first fully fcc (111) perpendicular MTJ with CoPt/MgO/CoPt structure was reported with 15% MR observed.

In Chapter 5, SOT devices with highly conductive epitaxial Ru/Cu nanolayered samples were studied and the effective spin Hall efficiency was evaluated quantitatively. The sharp interface Ru/Cu film has a sizeable ξ_{DL} of −2.2% due to the interface spin-orbit filtering effect. The insertion of Cu/Ru nanolayers can increase the ξ_{DL} value to −3.7% by the intrinsic contribution from the local electronic structure tuning of the lattice distortion near the interface. A large effective spin Hall conductivity is achieved to be $(3\sim5)\times10^5\ \hbar/2e\ \Omega^{-1}m^{-1}$, which is in a similar region as that of platinum.

Chapter 2 Experimental Methods

In this chapter, the experimental methods for sample preparation, characterization, and evaluation are described. All the thin film samples are fabricated by magnetron sputtering with a combination of eb-evaporation only for the Mg-Al-O barrier in Chapter 3. A series of characterization methods for the surface flatness, crystallinity, magnetic properties, and microstructure are conducted and analyzed. Then the sample stack was patterned into an MTJ pillar or Hallbar structure by microfabrication which consists of lithography, ion-milling, and sputtering. The patterned devices are further characterized by their transport properties as mentioned below.

2.1 Sample preparation

2.1.1 Magnetron sputtering

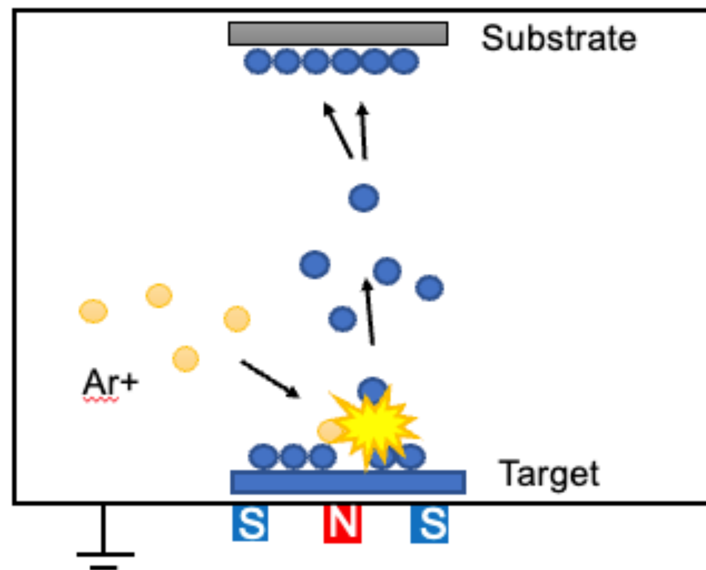

Figure 2.1 Schematic illustration of magnetron sputtering.

Magnetron sputtering is a technique of the physical vapor deposition methods (PVD) that is frequently employed in the production of thin films. The convenience of operation and relatively low cost are two important advantages for both laboratory research and industry applications. During the sputtering procedure, the material that is desired for sputtering (called target) is fixed on a cathode with a voltage power following a magnet beneath the target. Inside the ultrahigh vacuum chamber filled with Ar gas, when the high power voltage is introduced, the plasma will be generated with ionized Ar+. Due to the electric field between the cathode and anode, Ar+ particles are accelerated towards the target and bump out the atoms from the target surface and then the target material will deposit on the substrate in front of the target. The magnetic field generated by the magnet can attract the electrons all around to avoid damage to the substrate. There are two further types of sputtering depending on the target material. For conductive targets, direct current (DC) sputtering is a common method. As for the insulating material, charging at the target will reduce the deposition rate so an alternating electrical potential at radiofrequency (RF) is used. In this research, two sputtering systems were employed from Ulvac and EIKO, and the annealing, and RHEED pattern observation were conducted *in-situ* by the connected chamber in between without breaking the vacuum.

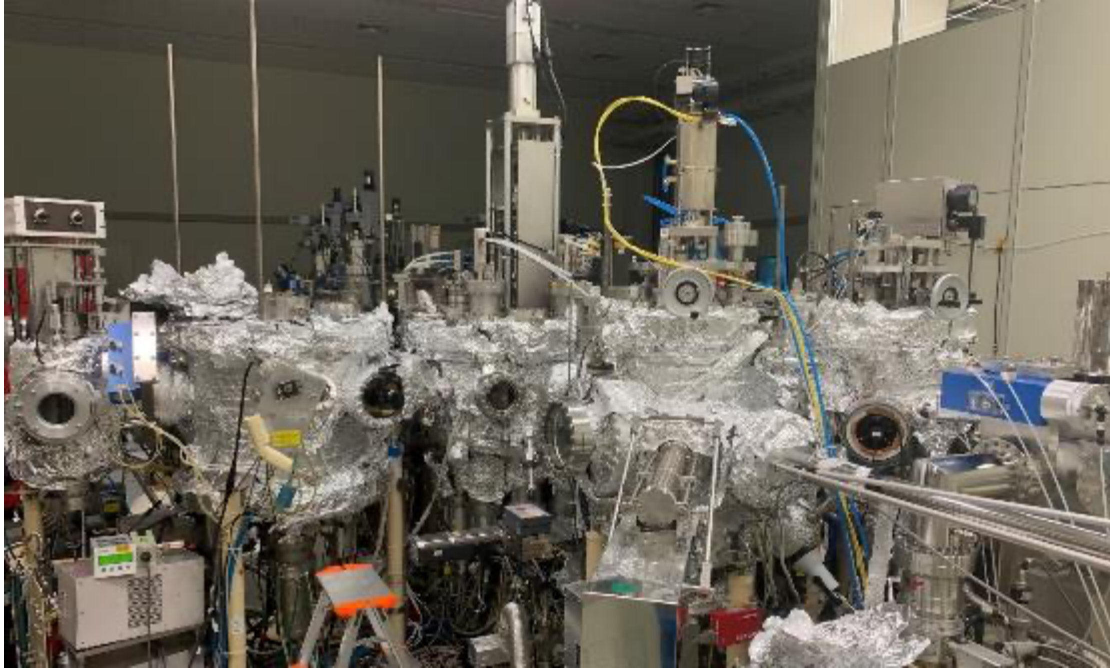

Figure 2.2 Photo of the ULVAC sputter system used in Chapter 3.

2.1.2 Electron-beam evaporation

Electron beam evaporation (EB) is used in this research for the fabrication of the barrier layer from a sintered $Mg_4Al\text{-}O_x$ pellet in Chapter 3. This is one of the molecular beam evaporation (MBE) methods that are often used for high-quality thin film fabrication. An electron beam is generated from a tungsten filament and then bombards the pellet and makes it evaporate then deposited on the substrate. In a high vacuum chamber (1×10^{-5} Pa for this study), the deposition rate can be accurately controlled by adjusting the power and a high-quality barrier layer with accurate thickness confirmed by a thickness monitor can be generated.

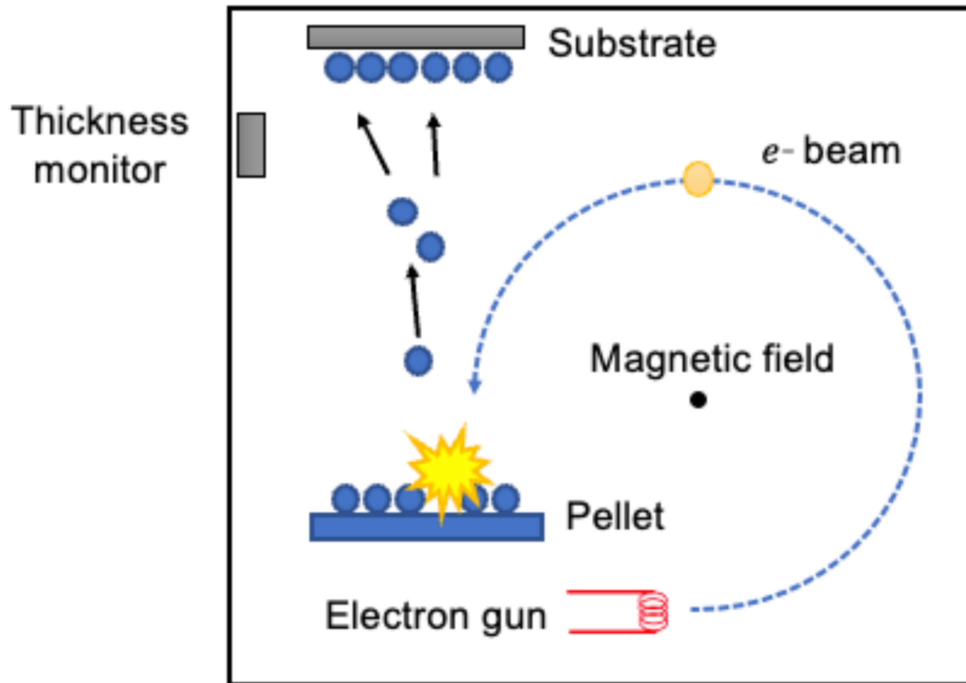

Figure 2.3 Schematic illustration of electron beam evaporation.

2.1.3 Microfabrication

Microfabrication is a complicated but significant process for electronic device fabrication. It usually takes some repeating steps including lithography, milling, and sputtering. Although the current in-plane tunneling (CIPT) measurement can also measure the CIPT-TMR from an unpatterned wafer, the microfabricated sample is still indispensable for providing a much lower resistance area (RA) and stable results. As Figure 2.4 shows, the top, and bottom electrodes are connected by the depositing of Au by sputtering and this kind of structure can only be made by using a different mask with a photoresist covering specific areas and milling out the unnecessary

parts or sputtering the material we need. Then the four-probe measurement can be done on this fabricated sample.

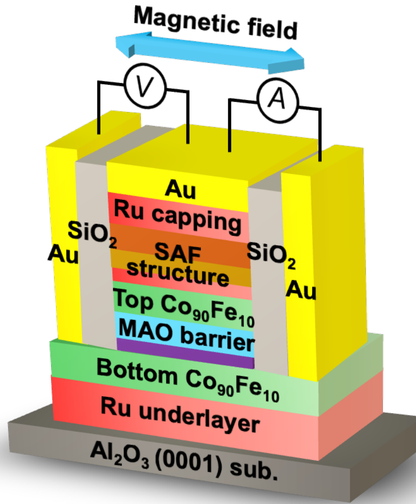

Figure 2.4 Schematic illustration of an MTJ stack after microfabrication, adapted from[48].

The basic solutions we used are listed here: Rinse: Butanone, promoter: Hexamethyldisilane (HMDS), photoresist: ma-N1407, Developer: ma-D533, Remover: N-Methyl-2-pyrrolidone (NMP).

A conventional lithography process can be introduced as follows: Buta cleaning – HMDS 3000 rpm, bake 100°C 2min – N1407 3000 rpm, bake 100°C 1min30s – lithography 100 seconds – develop by ma-D533/s for 90 seconds – D/W 30 seconds. Baking is for better integration of resist and sample's surface. The ion milling facility is shown in Figure 2.5 and the chamber vacuum is 5×10^{-4} Pa. In the different processes, we used different setting voltages and milling angles for accurately optimized milling control. An endpoint detection (EPD) machine is used in some processes to monitor the milling progress which is very important to define the milling step of each layer composition.

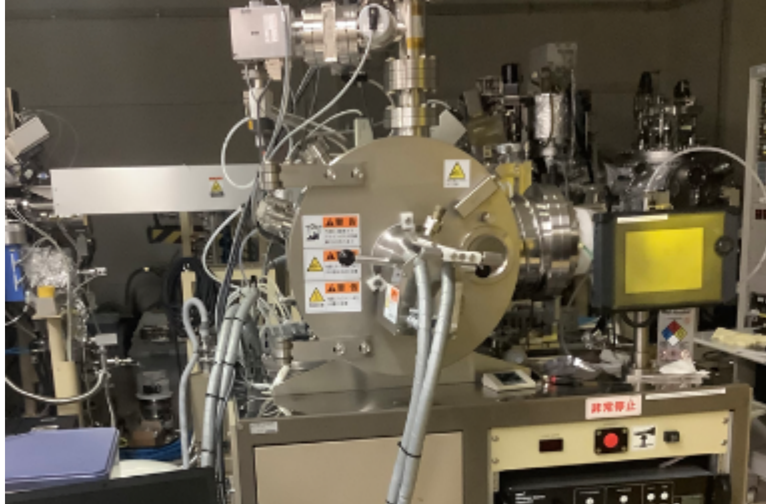

Figure 2.5 Photo of the milling system used in this work.

For sputtering, we used an Ulvac RF sputter system with the vacuum at 5×10^{-4} Pa and a conventional deposition rate for SiO2 is 0.642 Å/s for 175W and 15.0 SCCM, Ta is 0.958 Å/s for 70W and 15.0 SCCM, Au 0.699 Å/s for 100W and 15.0 SCCM. Please note that as time went by the deposition rates and chamber conditions are always fluctuating. As for the lift-off step, we used NMP for 5 minutes and then used Buta and D/W for washing.

The conventional process for fabricating an MTJ is shown as this:

1. Bottom electrodes: milling the cap – lithography – milling – lift-off
2. Pillars of MTJ: lithography – milling – sputter (SiO_2) – lift-off
3. Contact holes: lithography – milling – lift-off
4. SiO_2 pad: lithography – milling – lift-off
5. Top electrodes: lithography – milling – sputter (Ta/Au) – lift-off

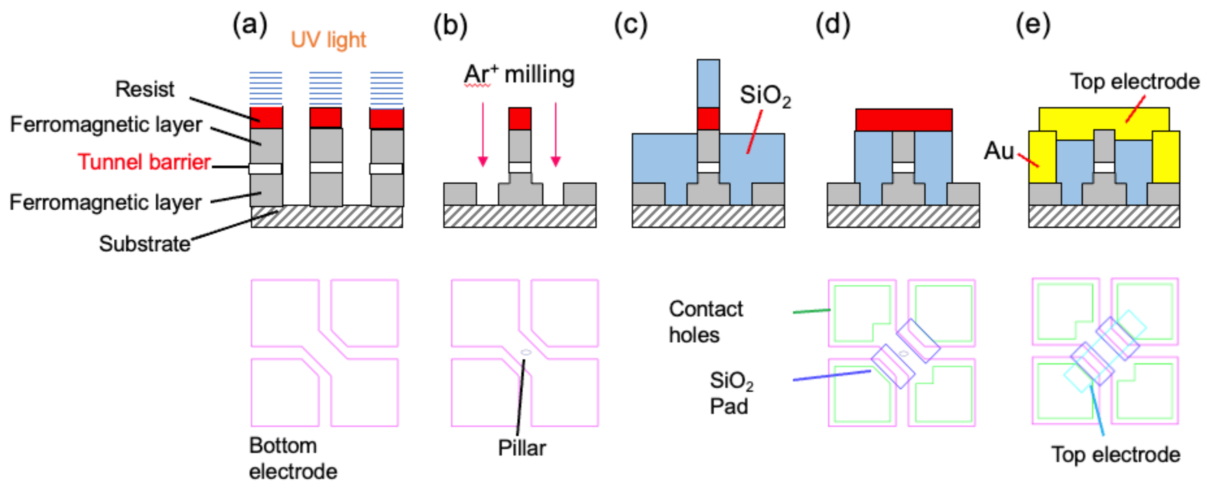

Figure 2.6 Schematic illustration of a microfabrication process (a) bottom electrode lithography and milling (b) pillar milling, (c) insulator SiO_2 deposition, (d) contact holes milling and SiO_2 pad deposition, (e) electrode deposition.

As Figure 2.6 shows, microfabrication is a series of lithography and milling processes for removing the unnecessary parts of the thin film and sputtering to deposit materials on the film. The first step is to make the bottom electrode pattern (Figure 2.6(a)), the mask configuration is shown at the bottom of the graph for each step. The next step is making the junction pillar and depositing SiO_2 around the pillar for protection (Figure 2.6(b), (c)). Because the pillar size is several micrometers, this step is very important and needs great caution for treatment. The third step is making the contact holes between the bottom electrode and top electrode and depositing a SiO_2 pad between the pillar and top electrode for insulation (Figure 2.6(d)). Finally, the conductive materials such as Ta and Au are deposited into the four squares, and the connection bridge on top is the electrode for electric measurements such as four-probe measurements.

2.2 Structural characterization

2.2.1 Atomic force microscopy (AFM)

When a magnetic thin film is used in devices, a flat surface with pinhole-free morphology is indispensable to avoid defects and shortage. Apart from this property, the surface morphology can also provide crystallographic information such as a terrace structure with different atomic steps. Atomic force microscopy (AFM) is a conventional method to characterize the surface flatness and morphology within the nanoscale. A probe fixed on a cantilever was used to detect the force between the probe and the samples' surface. Detected force data will be transferred into distance data by Hooke's law: $F = -k$ and a three-dimensional distribution of the scanning area will be generated based on the variation of surface roughness. Within this study, the AFM measurement was conducted in 5×5 μm^2 and 1×1 μm^2 scanning area. Parameters such as roughness average (R_a), peaks and valleys (P-V), and root mean square (RMS) are collected for analysis.

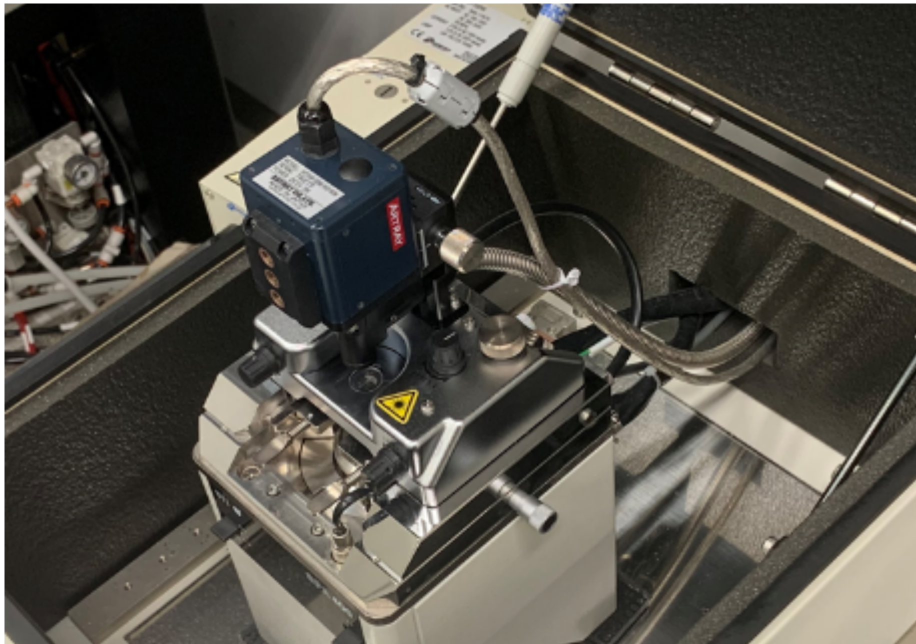

Figure 2.7 Photo of the AFM equipment used in this study.

2.2.2 X-ray diffractometry (XRD)

X-ray diffractometry is a conventional method for crystallinity characterization and orientation characterization in thin film and bulk samples. Based on Bragg's law, when the wavelength of the X-ray is consistent with the lattice distance between the atom planes in the crystal at a specific 2θ angle position, the amplified signal by constructive interference, which is called diffraction will occur with a high-intensity peak observed in the XRD spectrum. With different setting angles for different axes of the XRD sample stage, the out-of-plane and in-plane atomic structures can be observed.

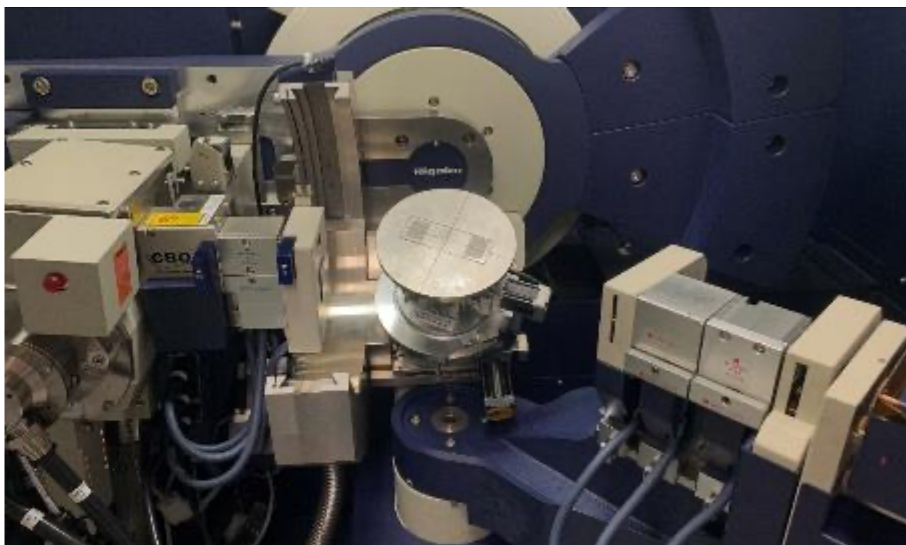

Figure 2.8 XRD in-plane measurement with a titled χ angle.

The rocking curve is measured by fixing the 2θ angle with only an incident angle ω scan to evaluate the crystallinity. In this study, we evaluated the full-width half maximum (FWHM) by Voigt fitting.

2.2.3 Reflection high-energy electron diffraction (RHEED)

There is one of the most important measurements for *in-situ* checks of crystallinity and surface roughness called reflection high-energy electron diffraction (RHEED) and if the time is controlled, there will be a negligible detrimental influence on the sample surface. This method uses a collimated high voltage electron beam irradiating the sample's surface and the diffraction pattern was shown on a screen on a view window by another side. From the RHEED pattern, it is easy to justify the thin film sample's crystal structure, especially for distinguishment of single crystal or polycrystalline. The diffraction pattern indicates the crystal orientation. Also, the intensity or sharpness of the streaks and spots with Kikuchi lines show the information of crystallinity. In the thin film deposition process, *in-situ* RHEED observation conducted during the deposition or annealing process at each layer's surface can monitor the sample's quality with a simple recording of the patterns.

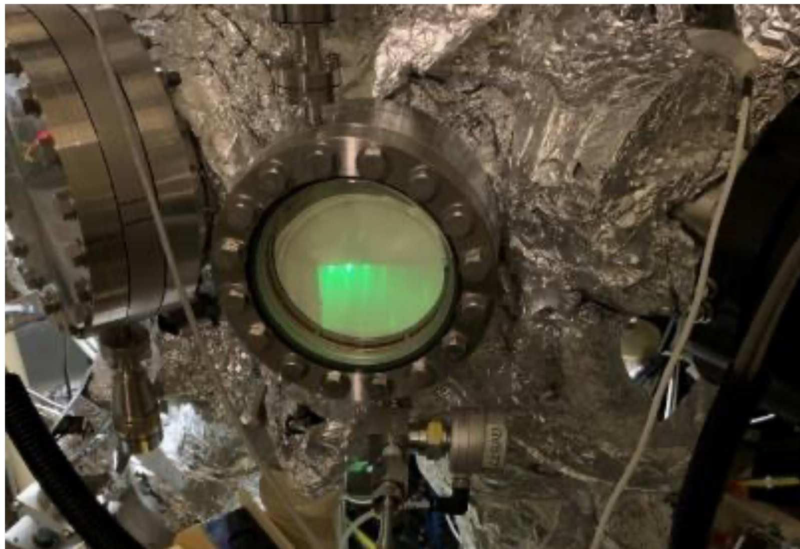

Figure 2.9 photo of an RHEED pattern illuminated on a screen.

2.3 Magnetic property measurement

2.3.1 Vibrating sample magnetometer (VSM)

For the characterization of magnetic materials, an important parameter is the magnetic property derived from the electrons' spin dynamics. The vibrating sample magnetometer (VSM) is a widely used method to analyze the magnetization of the sample and characterize the magnetic hysteresis curve. Key parameters such as the coercivity (H_c) and saturated magnetization (M_s) are crucial for evaluating the ferromagnetic layers in MTJ devices. As illustrated in Figure 2.10, the VSM measurement measures the electromotive force (emf) induced by the oscillating magnetic field of a magnetized sample vibrating along the z-axis according to Faraday's law of induction. The sinusoidal signal generated from the vibration can transfer the magnetic moment from the magnetized sample via an electric signal detected by the pickup coils. A lock-in amplifier ensures that only the signal at the vibration frequency is detected, which enables the precise measurement of the magnetic properties.

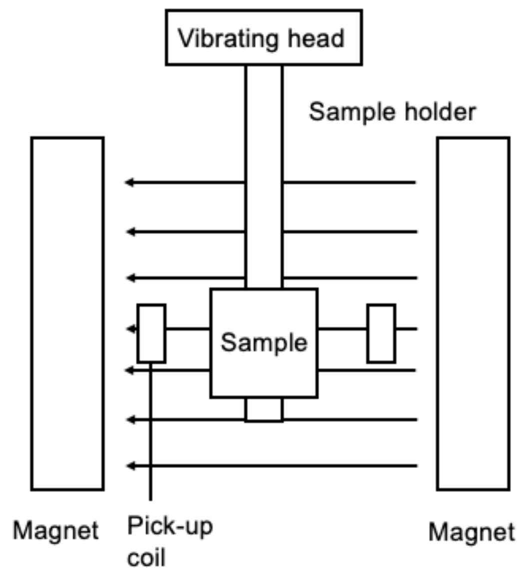

Figure 2.10 Schematic illustration of VSM.

2.3.2 Magneto-Optical Kerr Effect (MOKE)

By utilizing the magneto-optical effects, especially the Kerr effect, the magneto-optical properties of magnetic materials can be studied by MOKE measurement. This effect describes how the polarization and intensity of reflected light are affected when light is reflected from a magnetic thin film's surface. The MOKE system measures the Kerr angle θ_k which indicates the rotated linearly polarized light reflected from the sample's surface. In this work, we employed the polar MOKE (out-of-plane configuration), where the magnetization vector is perpendicular to the sample surface because our sample has perpendicular magnetic anisotropy.

2.4 Transport property measurement

2.4.1 Current in-plane tunneling measurement (CIPT)

Since the complexity and irreversibility of the microfabrication process, the current in-plane tunneling measurement (CIPT) is often used to evaluate the TMR value from an unpatterned wafer with comparable accuracy with patterned MTJ[70]. This method uses a set of probes with very small probe spacing (on the micron scale) contacting with the surface of the MTJ wafer. In Figure 2.11, the induced voltage is measured when a current flows through the sample, allowing for calculating the sheet resistance. In an MTJ structure, the current can flow in both the top electrode and tunnel through the bottom electrode. By changing the probe spacing by choosing a different probe set, the amount of tunneling current will be changed proportionally and affect the value of measured resistance. Then we can obtain the sheet resistance curve with the dependence of probe spacing. By fitting the results, we can get the TMR and *RA* values. In this study, by changing different magnet systems we can measure both in-plane and perpendicular MTJ samples.

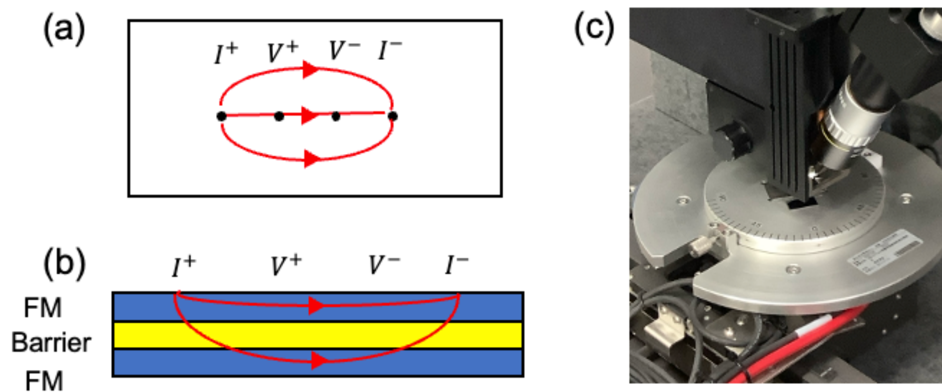

Figure 2.11 Schematic illustration of CIPT measurement (a) top view of current flowing, (b) side view, (c) photo of the CIPT measuring an in-plane MTJ sample from this study.

2.4.2 Four probe measurement

Four-probe measurement is a conventional method to determine the TMR from a microfabricated MTJ sample, as it can help minimize contact resistance. Figure 2.12 here shows the photo of the four-probe measurement setup by the monitor camera on top of the sample. A current source (power supply) is connected between the top and bottom FM layers and measures the voltage difference (current). With a sweeping external magnetic field, the resistance changes when the MTJ magnetization configuration switches between P and AP states. From this TMR-*H* curve, the TMR value can be calculated. The *I*-*V* curve is also measured at a fixed magnetic field for both the P and AP state and measuring the *I*-*V* dependence.

Figure 2.12 Photo of the four probe measurements in this study.

2.4.3 Unidirectional spin magnetoresistance (USMR)

The unidirectional spin magnetoresistance (USMR) is an effect that arises from the spin accumulation at the non-magnetic/ferromagnetic (NM/FM) interface and it depends on the alignment with parallel or antiparallel between the spin polarization direction of spin current and the magnetization direction of the FM layer. [71,72] The USMR signal can be utilized to identify the generation of spin current inside the NM layer, and this is often evaluated by measuring the second harmonic components of the longitudinal resistance ($R_{xx}^{2\omega}$).

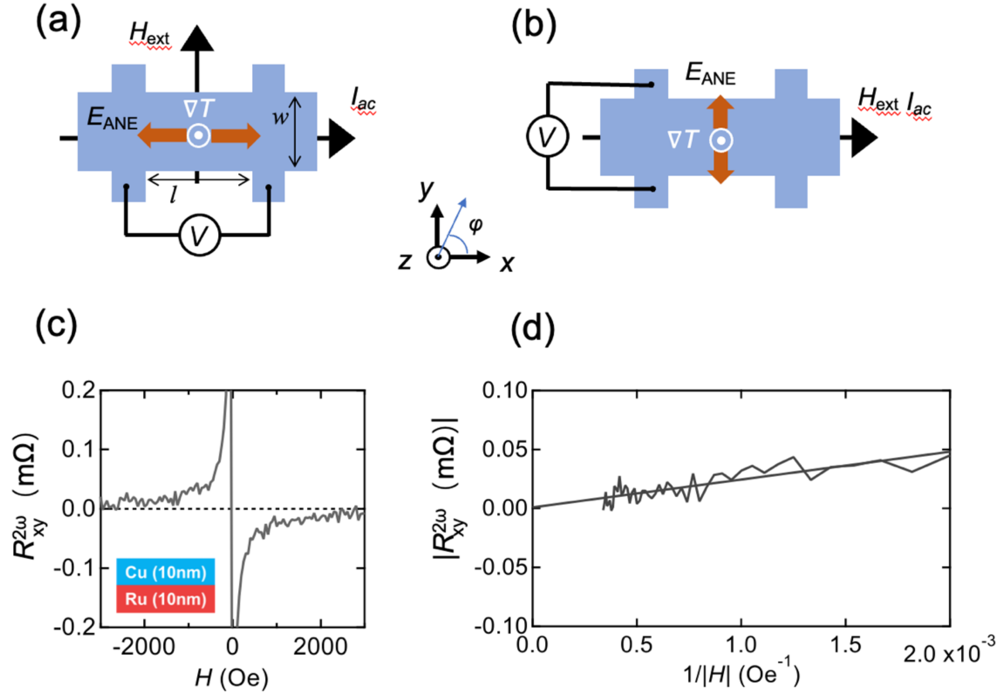

Figure 2.13 (a) The experimental setup for evaluating the thermal effect in the USMR measurement along the longitudinal direction and (b) transverse direction. The quantity observed is the thermal gradient from the Joule heating. (c) Transverse resistance $R_{xy}^{2\omega}$ for Ru (10nm)/Cu (10nm) sample analyzed during a field sweeping along *y* direction with a current density value *j* = 1.4 × 10^{7} A cm^{-2}. (d) The $R_{xy}^{2\omega}$ as a function of the reciprocal using the data from (c). The *y*-axis intercept corresponds to the contribution from the ANE effect, adapted from[73].

For evaluating the USMR signal accurately, there is a crucial step to analyze the thermoelectric component. As a supplementary to Chapter 5, this analysis was introduced here. In the USMR measurements, the longitudinal second harmonic resistance which is $R_{xx}^{2\omega}$ has two components with similar angular dependence, which can be derived by the following equation,

$$R_{xx}^{2\omega} = R_{xx(\mathrm{USMR})}^{2\omega} + R_{xx(\mathrm{ANE})}^{2\omega} \tag{1}$$

The signal $R_{xx(\mathrm{ANE})}^{2\omega}$ is due to the anomalous Nernst effect (ANE) which will be required to separate from the $R_{xx}^{2\omega}$ signal for the final USMR results. From the methods from references, [71,74]

the ANE effect can be evaluated by measuring the transverse Hall voltage ($R_{xy}^{2\omega}$) as illustrated in Fig. 2.13(b). When the magnetic field is sweeping along the longitudinal direction (which means that φ = 0), the second harmonic components of the transverse resistance, which is the $R_{xy}^{2\omega}$, contains two constituents from ANE and spin-orbital torques (SOTs) separately:

$$R_{xy}^{2\omega} = R_{xy(\mathrm{ANE})}^{2\omega} + R_{xy(\mathrm{SOT})}^{2\omega} \tag{2}$$

Here the $R_{xy(\mathrm{SOT})}^{2\omega}$ is attributed to the magnetization oscillations and its amplitude decreases when the magnetic field is increased. This is due to the proportional relationship between the SOT component and the magnetic susceptibility. Whereas, the ANE is independent of the magnetic field so will maintain as a constant. The intercept of the *y*-axis with the $R_{xy}^{2\omega}$ value versus 1/*H* results yields the $R_{xy(\mathrm{ANE})}^{2\omega}$ value, as given by the following equation:

$$R_{xy}^{2\omega} \approx R_{xy(\mathrm{ANE})}^{2\omega} \; (|H| \to \infty) \tag{3}$$

The fitting results for these data of Fig. 2.13(c) from Ru (10nm)/Cu (10nm)/NiFe (5nm) sample with a current density $j = 1.4 \times 10^7$ A cm^{-2} are plotted in Fig. 2.13(d). Here the intercept of the *y*-axis we can find that the $R_{xy(\mathrm{ANE})}^{2\omega}$ contribution is rather small.

Further, if we want to obtain the ANE signal from the longitudinal direction, we used the aspect ratio of the Hall bar device to convert the $R_{xy(\mathrm{ANE})}^{2\omega}$ to $R_{xx(\mathrm{ANE})}^{2\omega}$ since that the ANE effect is proportional to the voltage between the devices followed by this relationship:

$$|R_{xx(\mathrm{ANE})}^{2\omega}| = |R_{xy(\mathrm{ANE})}^{2\omega} \times \frac{l}{w}| \tag{4}$$

In this study, we have l = 25 μm and w = 10 μm, and then the $R^{2\omega}_{xx(\mathrm{USMR})}$ value was given finally by substituting the $R^{2\omega}_{xx(\mathrm{ANE})}$ followed by this equation:

$$R^{2\omega}_{xx(\mathrm{USMR})} = R^{2\omega}_{xx} - R^{2\omega}_{xx(\mathrm{ANE})} \quad (5)$$

After this conversion, the range of $R^{2\omega}_{xx(\mathrm{ANE})}$ signal in this study is around 0.003–0.005mΩ. For all results shown in this thesis, we performed the subtraction of the ANE contribution as introduced above.

2.4.4 Spin torque ferromagnetic resonance (ST-FMR)

The spin current can exert a spin-orbital torque (SOT) on the magnetization of the FM layer, which causes the ferromagnetic resonance (FMR). Then a DC voltage can be induced by the ST-FMR due to the anisotropic magnetoresistance (AMR) effect from the FM layer. The produced DC voltage contains two mixed components, including a symmetric Lorentzian line shape (V_S) and an antisymmetric Lorentzian line shape (V_A) which can be derived by the following, [55]

$$V = V_S \frac{\Delta^2}{(H-H_{\mathrm{res}})^2+\Delta^2} + V_A \frac{\Delta(H-H_{\mathrm{res}})}{(H-H_{\mathrm{res}})^2+\Delta^2} + C, \quad (6)$$

where V_S is related to the damping-like (DL) SOT from the oscillation of the spin current and V_A is related to the Oersted field and the field-like (FL) spin torque. The Δ is the resonance linewidth, H_{res} is the resonance field, and C is a constant that represents the offset of the voltage signal. The detailed analysis procedure is given in Chapter 5.

Chapter 3 Fully epitaxial fcc(111) magnetic tunnel junctions with a $Co_{90}Fe_{10}$/MgAlO/$Co_{90}Fe_{10}$ structure

3.1 Introduction

Recently, first-principles calculations predicted that a new class of an fcc(111)-type MTJ with Co/MgO/Co(111) structure exhibits a large TMR ratio exceeding 2000%, [11] which is attributed to the interfacial resonance tunneling mechanism, in sharp contrast to the conventional coherent tunneling mechanism through bulk band structures of bcc (001) MTJ structure. A (111) plane generally has the most stable and lowest surface energy in a metallic fcc lattice, [75] allowing the construction of stable MTJ structures without changing the crystal system. In addition, the theoretical calculations of MTJs with Co-based $L1_1$(111) alloys, which have an fcc fundamental crystal structure, such as CoPt/MgO/CoPt(111) and CoPd/MgO/CoPd(111), exhibit both large TMR ratios and large PMA energies. [44] A high PMA energy is indispensable for ultra-high density applications for downscaling the junction size below 10nm or even smaller. However, it is generally difficult to obtain a flat MgO(111) layer because of its polar surface property with very high surface energy, e.g. a charge-imbalanced surface. [76] Above all, it is necessary to explore the preparation and demonstration methods for the fully fcc(111) based MTJ stacks.

The research of (111) MTJ has several difficulties in the demonstration of a fully epitaxial fcc (111) stack. Most concerns about the MgO barrier. It is necessary to mention that the theoretical model assumed a perfect lattice matching but the bulk lattice mismatch between Co and MgO is almost 20%. The (111) MgO barrier generally has an imbalanced polar surface with infinite surface

energy which leads to the impossible to obtain a flat surface but always three-dimensional island growth. The top FM layer growth on this MgO (111) barrier will also be another challenge.

In this section, we report the achievement of a fully epitaxial fcc(111) MTJ using $Co_{90}Fe_{10}$ (CoFe)/$Mg_4Al\text{-}O_x$ (MAO)/CoFe structure by combining magnetron sputtering for the ferromagnetic layer with CoFe and electron-beam evaporation for the barrier layer with MAO. Crystal structure analysis reveals the epitaxial (111) growth with high crystallinity from the trilayer structure. Relatively flat FM/barrier interfaces were observed by cross-sectional scanning transmission electron microscopy (STEM) images with periodic misfit dislocations formed between the CoFe electrode and the MAO barrier layer to minimize the influence of their large lattice mismatch (~20%). For the TMR evaluation, we observed a TMR ratio of up to 37% at room temperature (RT) and 47% at 10 K in this CoFe/MAO/CoFe(111) MTJ. In addition, symmetric differential conductance (dI/dV) curves with bias polarities were confirmed, indicating the achievement of well-balanced interfaces between the bottom and upper CoFe/MAO sides. This is the first demonstration of a fully fcc (111) MTJ structure which is significant for the future development of the conventional bcc (001) way[48].

3.2 Experiment procedures

In this study, the MTJ stack was deposited on a single-crystal sapphire Al_2O_3(0001) substrate combining a magnetron sputtering apparatus (ULVAC, Inc. base pressure ~4×10^{-7} Pa) for all metallic layers and an EB evaporator apparatus for the $Mg_4Al\text{-}O_x$ barrier. [26] Substrate treatment and the optimization for the Ru underlayer were carefully performed before the deposition of the MTJ stack fabrication. The sapphire substrates were *ex-situ* annealed at 1000°C for 1 hour in a

muffle furnace (AS ONE HPN-ON shown in Fig 3.1(a)) under an air atmosphere to improve their surface morphology and flatness. As shown in Fig 3.1(b), some holes can be observed on the surface of the substrate without treatment. After the thermal cleaning (Fig. 3.1(c)), the terrace structure which may represent the formation of the atomic step was shown. Several temperature conditions were conducted for optimization of the thermal cleaning condition and the results of 5×5 μm^2 AFM are shown in Table 3.1. The best flatness results were obtained with 1000°C compared with 800°C or 1200°C. This substrate treatment was conducted for all the work within this thesis including the other two chapters.

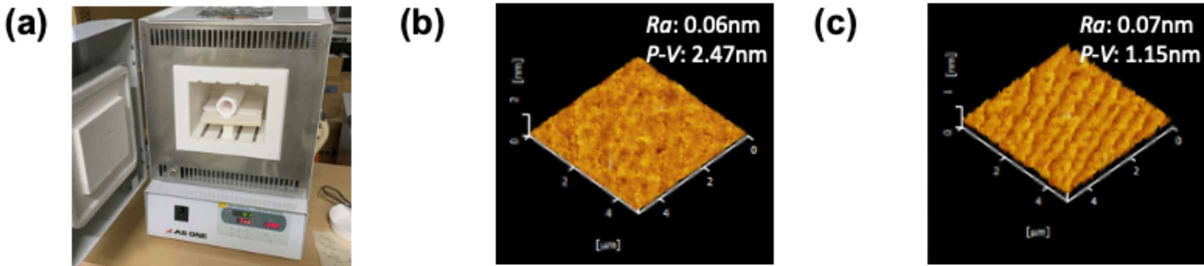

Figure. 3.1 (a) Photo of the electrical furnace. (b-c) 5×5 μm^2 AFM results of the Al_2O_3 substrate (b) no thermal cleaning (c) with 1000°C 1h thermal cleaning. The lowest values were made in bold font.

5×5 μm^2 AFM	None	800 °C	1000 °C	1200 °C
R_a (nm)	0.19	0.07	**0.06**	0.13
P-V (nm)	46.05	4.53	**0.78**	21.66

Table 3.1. Summary of the 5×5 μm^2 AFM results of Al_2O_3 substrate with different thermal cleaning conditions, all thermal cleaning are conducted for 1 hour.

After achieving the optimization for the substrate, the deposition of the Ru underlayer was also optimized for the realization of the nice flatness and high crystallinity. The temperature profile of the deposition procedure of the high-quality Ru underlayer is shown in Fig. 3.2(a). After degassing

at 350℃ for 1 hour to obtain a stable deposition condition, Ru was deposited at substrate heating with the same temperature of 350℃ following a high annealing with 750℃ for 1 hour [73]. The flatness of the surface morphology of a 40nm Ru single layer was shown by the AFM 5×5 μm^2 measurement in Fig. 3.2(b) with an average roughness (R_a) value of 0.15 nm and a peak-to-valley (*P*-*V*) value of 1.54 nm. The RHEED pattern of the Ru underlayer is shown in Fig. 3.2(c), the sharp streaks and obvious Kikuchi line indicate the high crystallinity of this Ru layer.

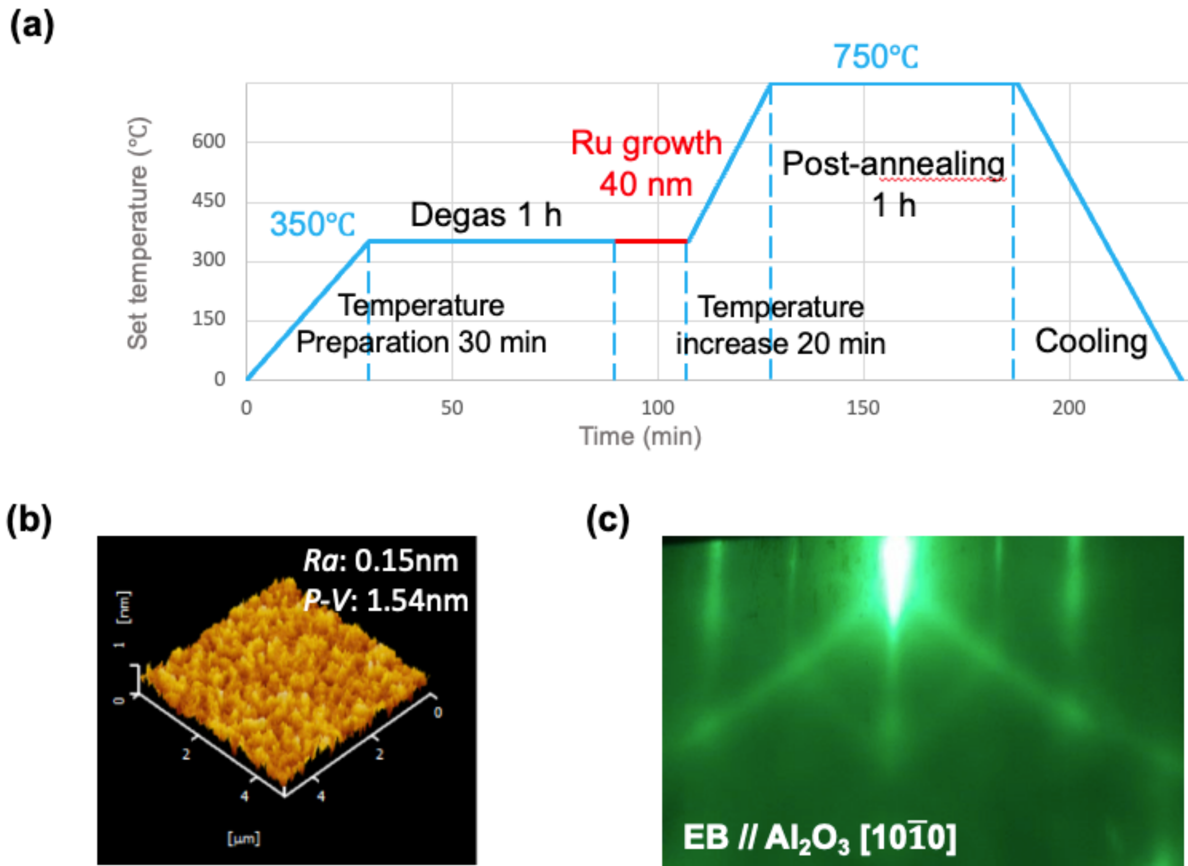

Figure. 3.2 (a) Optimized temperature profile for Ru underlayer deposition. (b) 5×5 μm^2 AFM results of the substrate/Ru 40nm single layer (c) RHEED pattern of the Ru underlayer observed after post-annealing. The incident electron beam is parallel to the $Al_2O_3[10\bar{1}0]$ azimuth.

The deposition condition especially the temperature for post-annealing of the ferromagnetic layer was also carefully optimized. As shown in Table 3.2 and 3.3. The summary of the 5×5 μm^2 AFM results and the full-width half maximum (FWHM) of the rocking curve from XRD out-of-plane measurement were listed and the 400°C annealing temperature yields the lowest surface roughness and FWHM which indicates a flat surface and high crystallinity. This condition was chosen for the MTJ stack fabrication.

5×5 μm^2 AFM	**300 °C**	**400 °C**	**450 °C**	**500 °C**
R_a (nm)	0.15	**0.12**	0.14	1.35
P-V (nm)	2.62	**1.31**	1.46	16.81

Table 3.2. Summary of the 5×5 μm^2 AFM results of Al_2O_3//Ru40nm/$Co_{90}Fe_{10}$20nm/Ru2nm with various annealing temperatures. The lowest values were made in bold font.

FWHM (°)	**300 °C**	**400 °C**	**450 °C**	**500 °C**
$Co_{90}Fe_{10}$	0.054	**0.050**	0.086	0.065

Table 3.3. Summary of the FWHM value from XRD rocking curve measurement of Al_2O_3//Ru40nm/$Co_{90}Fe_{10}$20nm/Ru2nm with various annealing temperatures. The lowest values were made in bold font.

Top-exchange-bias type MTJ multilayers were prepared as the following stack design: Al_2O_3(0001)//Ru (40)/$Co_{90}Fe_{10}$ (CoFe) (20)/Mg (0.5)/Mg_4Al-O_x (2.5)/CoFe (5)/Ru (0.75)/$Co_{50}Fe_{50}$ (2.2)/$Ir_{20}Mn_{80}$ (IrMn) (10)/Ru (10) (nominal thickness in nm) (Fig. 3.1a). Instead of a pure Co as the ferromagnetic layer (FM) assumed in the theory, [11] which always shows both

hcp and fcc mixed structures, the $Co_{90}Fe_{10}$ layers were used as the FM layers to obtain a single fcc phase. The Mg-rich MAO (Mg_4Al-O_x) was used as a barrier following the previous report that larger TMR ratios (up to 429% at RT)[26] than those of MgO (417%)[18] observed in the Fe(001)-MTJ studies. All metallic layers were deposited by DC magnetron sputtering where the substrate heating temperature for Ru is at 350°C[73] and other layers were deposited at RT. Each layer was *in-situ* post-annealed with optimized temperature conditions to obtain a flat surface and high crystallinity. The Mg layer was inserted at the lower CoFe/MAO interface to avoid over-oxidation during the MAO deposition as reported by the previous study. [21] The MAO barrier was deposited by EB-evaporation from a sintered MAO pellet with a nominal Mg/Al atomic ratio = 4 and a deposition rate of $\sim 8 \times 10^{-3}$ nm s^{-1}.[26] The CoFe/Ru/$Co_{50}Fe_{50}$/IrMn structure acts as a pinned layer with an SAF structure for obtaining a stable AP state. After the deposition, the MTJ stack was *ex-situ* magnetic annealed at 300°C for 30 minutes under a 7 kOe magnetic field along the $Al_2O_3[10\bar{1}0]$ direction.

As for the characterization method, the crystal structures were characterized by *in-situ* reflection high energy electron diffraction (RHEED) methods and *ex-situ* X-ray diffraction (XRD) with Cu K_α radiation (wavelength: 0.15418 nm) utilizing a graphite monochromator. The microstructure analysis was performed by the high-resolution high-angle annular dark-field STEM (HAADF-STEM), nano-beam electron diffraction (NBED), and the energy dispersive x-ray spectroscopy (EDS) (FEI Titan G2 80–200 ChemiSTEM) measurements. The MTJ stacks were patterned by photolithography and Ar-ion milling for a 39 μm^2 area elliptical junctions pillar with the long axis parallel to the $Al_2O_3[10\bar{1}0]$ axis. TMR ratios were measured by a conventional DC 4-probe method at RT with the source meter (Keithley, 2400) and nanovoltmeter (Keithley, 2182A). Temperature dependence from RT to 10 K of the TMR ratio and samples' resistances were characterized with a

physical property measurement system (PPMS) apparatus (Quantum Design, Dynacool). In this work, a negative bias voltage corresponds to electrons tunneling from the bottom to the top layer. The value for the TMR ratio is defined as $(R_{AP} – R_P)/R_P \times 100\%$.

3.3 Results and Discussions

3.3.1 Structural properties of $Co_{90}Fe_{10}$/MgAlO/$Co_{90}Fe_{10}$ stack

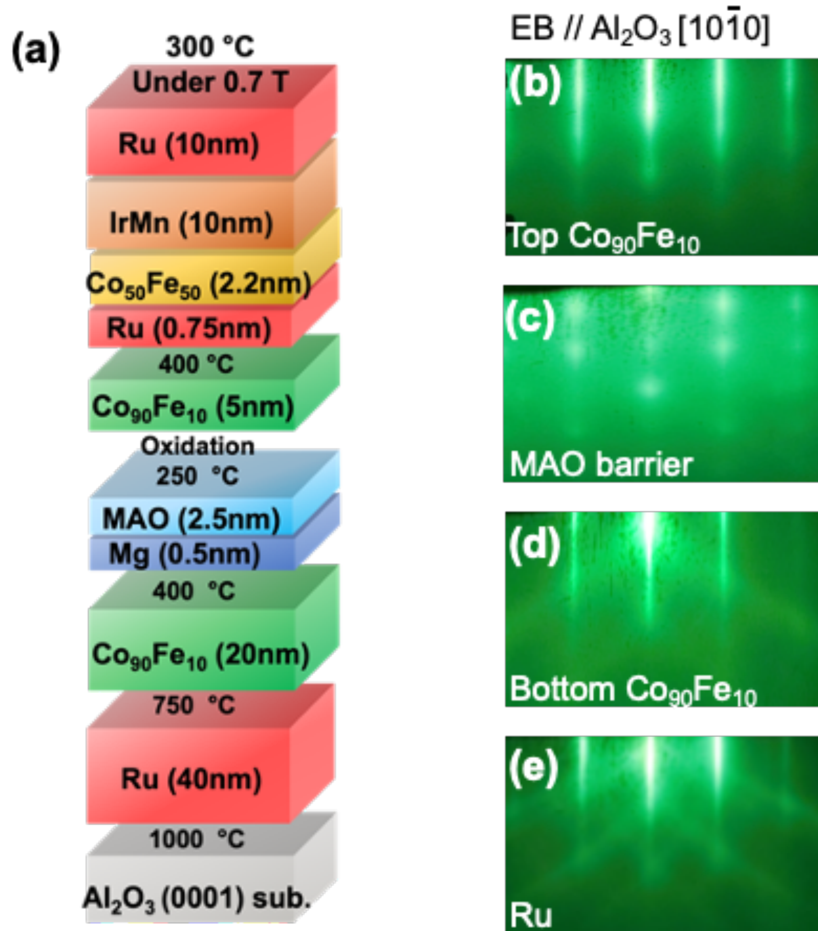

Figure. 3.3 (a) Schematic MTJ stacking structure with post-annealing temperatures and oxidation process profiles. (b-e) RHEED patterns of (b) top CoFe, (c) MAO barrier, (d) bottom CoFe, and (e) Ru buffer. The direction of the incident electron beam is parallel to the $Al_2O_3[10\bar{1}0]$ azimuth. All observations were performed after post-annealing.

Figure 3.3(a) illustrates the schematic MTJ stack structure with post-annealing temperature profiles and oxidation process conditions. Figure 3.3(b-e) shows the reflection high energy electron diffraction (RHEED) patterns with incident electron-beam along the Al_2O_3 $[10\bar{1}0]$ azimuth for (e) the Ru buffer layer, (d) bottom CoFe, (c) MAO barrier, and (b) top CoFe layer. All RHEED patterns were taken after each layer's *in-situ* post-annealing. The Ru buffer's pattern here showed the sharp streak lines with Kikuchi arcs and these features indicate the epitaxial growth with a very flat surface and excellent crystallinity from the hcp(0001) growth. This confirms the technique for the Ru underlayer growth on a high-quality engineered sapphire substrate. The bottom CoFe layer also shows similar patterns which indicates that the epitaxial growth of fcc(111) CoFe is realized on the Ru(0001). Following these results, the MAO barrier also has evidence for (111) epitaxial growth; however, the spotty-like pattern indicates that the MAO surface is rougher than the bottom CoFe surface as a known behavior in MgO (111) structures. [77–79] This may be attributed to the large lattice mismatch with the CoFe layer and the surface reconstruction for reducing the surface energy of the charge-uncompensated (111) surface. Nevertheless, the top CoFe layer recovers back to the (111) epitaxial growth together with the high crystallinity again on the MAO barrier layer, demonstrating the realization of a fully epitaxial fcc(111) MTJ structure.

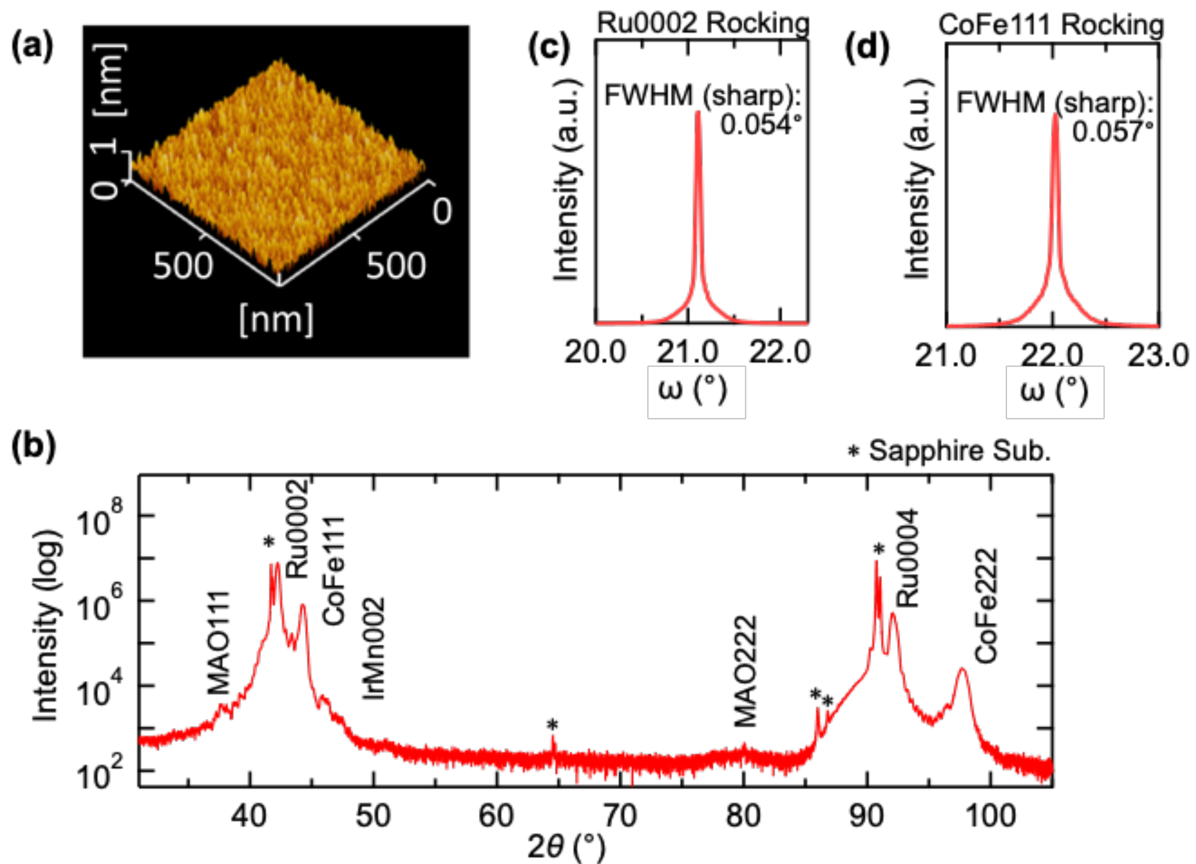

Figure. 3.4 (a): AFM image of the MTJ stack. (b) Out-of-plane XRD spectrum of the MTJ stack. (c, d) Rocking curves of (c) Ru(0002) peak and (d) CoFe(111) peak from a stack with Al_2O_3(0001)//Ru (40 nm)/CoFe (20 nm)/Ru (2 nm) structure.

Figure 3.4(a) shows an atomic force microscopy (AFM) image with a 1×1 μm^2 area from the MTJ sample surface. We obtained an average roughness (R_a) value of 0.18 nm and a peak-to-valley (P-V) value of 1.96 nm as shown on the AFM image, indicating the achievement of a flat surface suitable for the MTJ devices. Figure 3.4(b) shows the out-of-plane 2θ-ω XRD results of the MTJ stack. The (0001) growth from hcp Ru and the (111) growth from fcc CoFe were confirmed by the Ru(0002), Ru(0004), CoFe(111), and CoFe(222) peaks. The (111) and (222) peaks for MAO (with indices for a cation-disordered spinel structure[22]) were also observed. Due to the advantage of a flat Ru buffer, the fringe patterns corresponding to 40 nm are observed around the Ru peaks. In

Fig. 3.4(c) and 3.4(d), the rocking curves (ω-scan) of the Ru(0002) peak and the CoFe(111) peak of a reference sample with a bottom electrode structure of Al_2O_3(0001) sub.//Ru (40 nm)/CoFe (20 nm)/Ru (2 nm) were shown. These curves consist of two components: a sharp specular component and a broad diffuse component. Such broad components in a rocking curve are often observed in highly oriented epitaxial thin films due to the strain field caused by introducing the misfit dislocations near interface regions. [80] The values of full-width half maximum (FWHM) for the sharp and broad components for Ru (CoFe) are 0.054° and 0.34° (0.057° and 0.38°), respectively. The small FWHMs of the sharp components indicate that nearly perfect orientation has been achieved for Ru(0001) and CoFe(111).

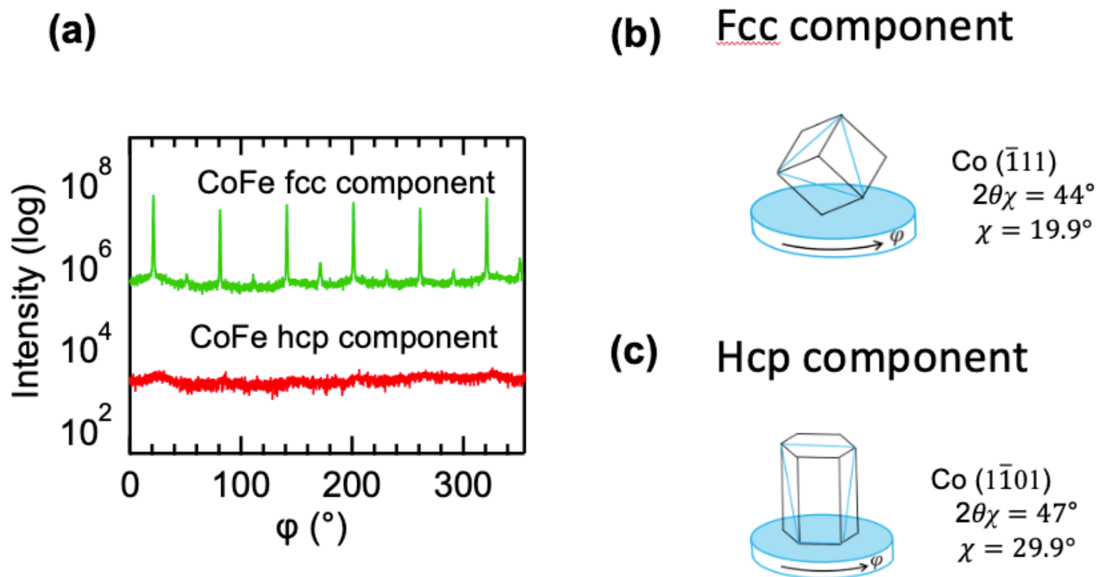

Figure. 3.5 (a) In-plane pole figures for CoFe(11$\bar{1}$)fcc and (1$\bar{1}$01)hcp poles of the MTJ stack. (b, c) Illustration of measurement configuration for pole figure (b) CoFe(11$\bar{1}$)fcc and (c) (1$\bar{1}$01)hcp.

Figure 3.5(a) shows the in-plane XRD pole scan (φ-scan) spectra to obtain the information on fractions of hcp or fcc components from the CoFe layers in the MTJ stack. The upper (lower) spectrum corresponds to the pole scan of $(11\bar{1})_{fcc}$, with measurement setup of $2\theta_\chi \sim 43.9°$ and $\chi \sim$

19.9° [$(1\bar{1}01)_{hcp}$, $2\theta_\chi \sim 46.2°$ and $\chi \sim 29.9°$]. [81] The measurement settings are illustrated in Figure 3.5(b) and 3.5(c) for $(11\bar{1})_{fcc}$ and $(1\bar{1}01)_{hcp}$ plane, separately. Compared with pure Co which always has a mixed phase between the hcp component and the fcc component. The 10% Fe doping used here as a CoFe electrode has an almost pure fcc phase as the XRD results show. The upper spectrum has distinct 6-fold peaks from the fcc phase. The additional smaller 6-fold peaks at an offset of 30° are attributed to the presence of a variant in the CoFe layers. In contrast, the lower spectrum shows no distinct peaks from the hcp component. In conclusion, the CoFe layers for this MTJ stack consist of an almost perfect fcc structure utilizing the $Co_{90}Fe_{10}$ composition instead of a pure Co, which is consistent with the theoretical model with the fcc (111) structure.

3.3.2 Microstructure analysis of $Co_{90}Fe_{10}$/MgAlO/$Co_{90}Fe_{10}$ stack

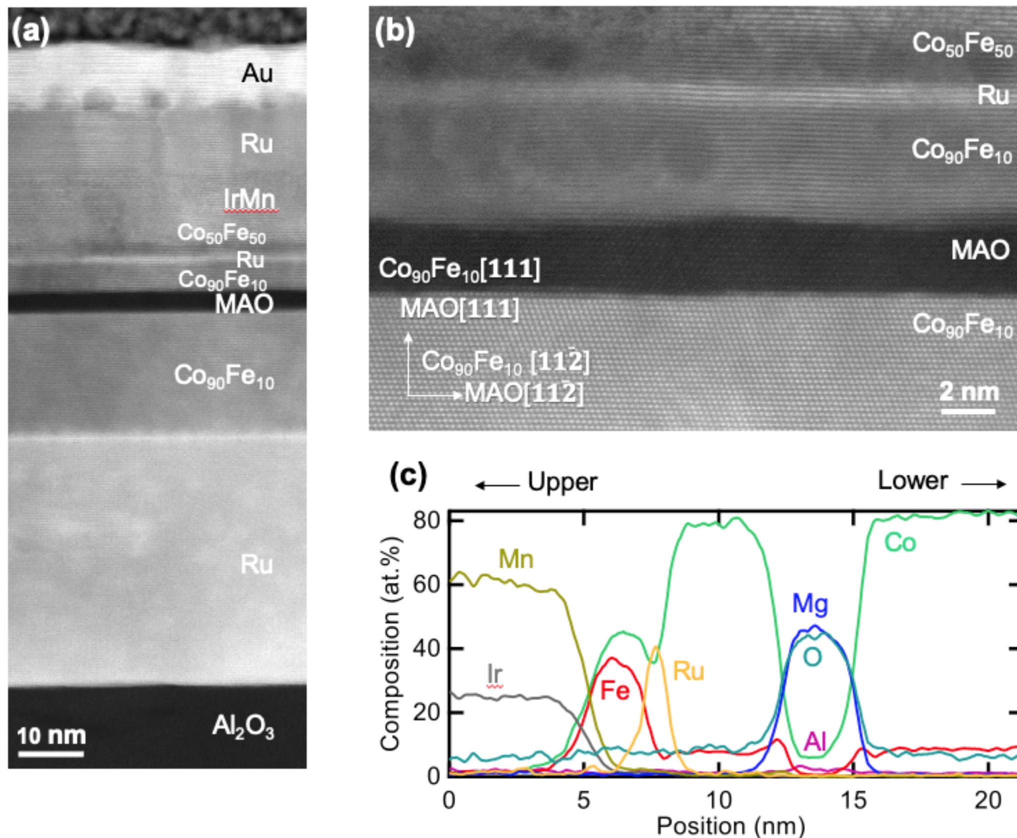

Figure. 3.6 (a) Cross-sectional HAADF-STEM image of the MTJ stack observed along $Al_2O_3[10\bar{1}0]$. (b) Magnified HAADF-STEM image of (a) near the CoFe/MAO/CoFe. (c) Elemental depth profiles by EDS.

Figure 3.6 shows the cross-section HAADF-STEM images of the MTJ stack. From the HAADF-STEM image of the entire stack in Fig. 3.6(a), flat and sharp interfaces were consistently maintained from the Ru buffer layer to the top CoFe layer. Figure 3.6(b) shows the magnified image at the CoFe/MAO/CoFe trilayer. At this region, we can find that the lower CoFe/MAO interface is atomically flat compared with the upper MAO/CoFe interface with slightly rougher than the lower interface. However, the formation of a stable fcc-based (111) barrier layer shown in the image is a crucial step to designing fully (111)-type MTJs. The thickness of the MAO barrier layer was determined to be ~2.75 nm from this HAADF-STEM image in Fig. 3.6(b). Figure 3.6(c) shows the EDS elemental line profiles across the cross-section of this film. Note that the O signal outside the barrier is an artifact coming from the TEM specimen surface. From these results, the MAO barrier consists mainly of MgO with a negligible amount of Al, which can be explained by the low Al concentration from the electron-beam (EB) source (Mg_4Al-O_x) and the fluctuation in Mg-Al composition during the deposition process. A small amount of Fe segregation was also shown at the upper and lower CoFe/MAO interfaces, which could be attributed to the higher oxygen affinity of Fe compared with Co.

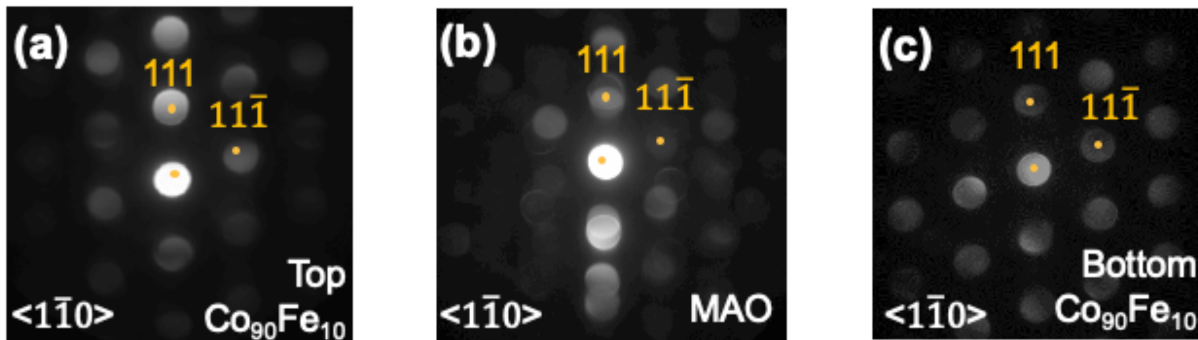

Figure. 3.7 NBED patterns for (a) top CoFe, (b) MAO barrier, and (c) bottom CoFe.

In Fig. 3.7, the NBED patterns observed from the region of the HAADF-STEM observation confirm the epitaxial growth of (111) orientation of the bottom CoFe, MAO barrier, and top CoFe layers. And the epitaxial relationship of $Al_2O_3(0001)[11\bar{2}0]$ || Ru(0001)$[10\bar{1}0]$ || $Co_{90}Fe_{10}(111)[11\bar{2}]$ || MAO(111)$[11\bar{2}]$ was determined by these NBED patterns, which is consistent with previous RHEED and XRD results. Thus, our CoFe/MAO/CoFe(111) structure closely reproduces the theoretical supercell stack of Co/MgO/Co(111), except for the large lattice mismatch, as detailed in the following explanation.

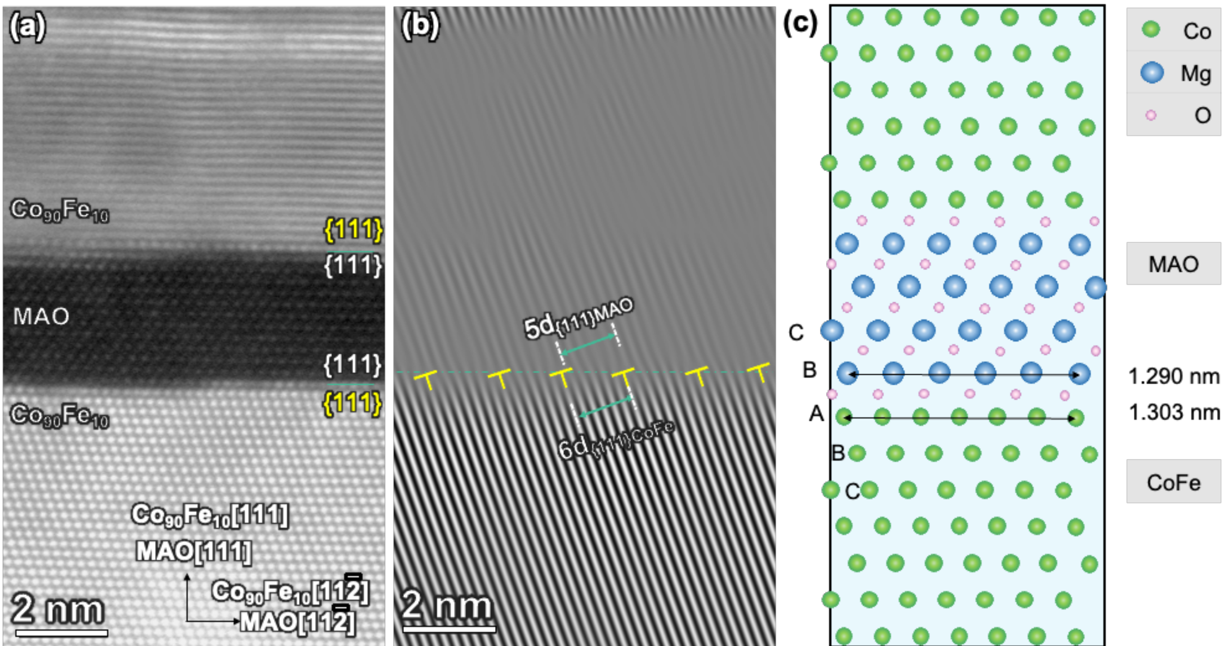

Figure. 3.8 (a) Cross-sectional HAADF-STEM images of the MTJ stack observed along the $Al_2O_3[10\bar{1}0]$, orange lines indicate the {111} planes of CoFe and MAO. (b) FFT filter images using the data from (a). ⊥ Marks in (b) indicate the lattice dislocations at the interface. (c) Illustration of the interface atomic model.

The high-magnification HAADF-STEM image near the barrier region is shown in Fig. 3.8. The lattice parameter of MAO is determined to be a_{MAO} = 0.420 nm according to the local atomic

structure, which is almost identical to the bulk value of MgO (0.421 nm). The lattice mismatch between CoFe and MAO is calculated to be ~20%. Due to this rather large lattice mismatch, a periodic distribution of misfit dislocations is revealed at the lower MAO/CoFe interface which is shown in the inverse fast Fourier transformation (FFT) image in Fig. 3.8(b). The six {111} planes of CoFe coincide with five {111} lattice planes of MAO as illustrated in Fig. 3.8(c). The distance of the 5-plane MAO domain and that of the 6-plane CoFe is 1.290 nm and 1.303 nm, respectively; therefore, their mismatch becomes only –1% by introducing the 5:6 domain matching, which is much smaller than the value of 20%. From the STEM image, the top CoFe was not perfectly oriented and may rotate slightly along the [111] axis within the film plane, as evidenced by the interplanar distance from the top CoFe layer. It is also suggested that the O atoms are located directly above the (Co, Fe) atoms at the interfaces, which is consistent with the theoretical model predicting an energetically stable Co-O interface rather than a Co-Mg interface. [11,82] Therefore, it is speculated that the (111) growth was preserved throughout the growth from the bottom to the top FM layer. The observed 5:6 domain matching with introducing periodic dislocations may explain the formation of the relatively flat barrier interfaces.

3.3.3 Transport properties of $Co_{90}Fe_{10}$/MgAlO/$Co_{90}Fe_{10}$ stack

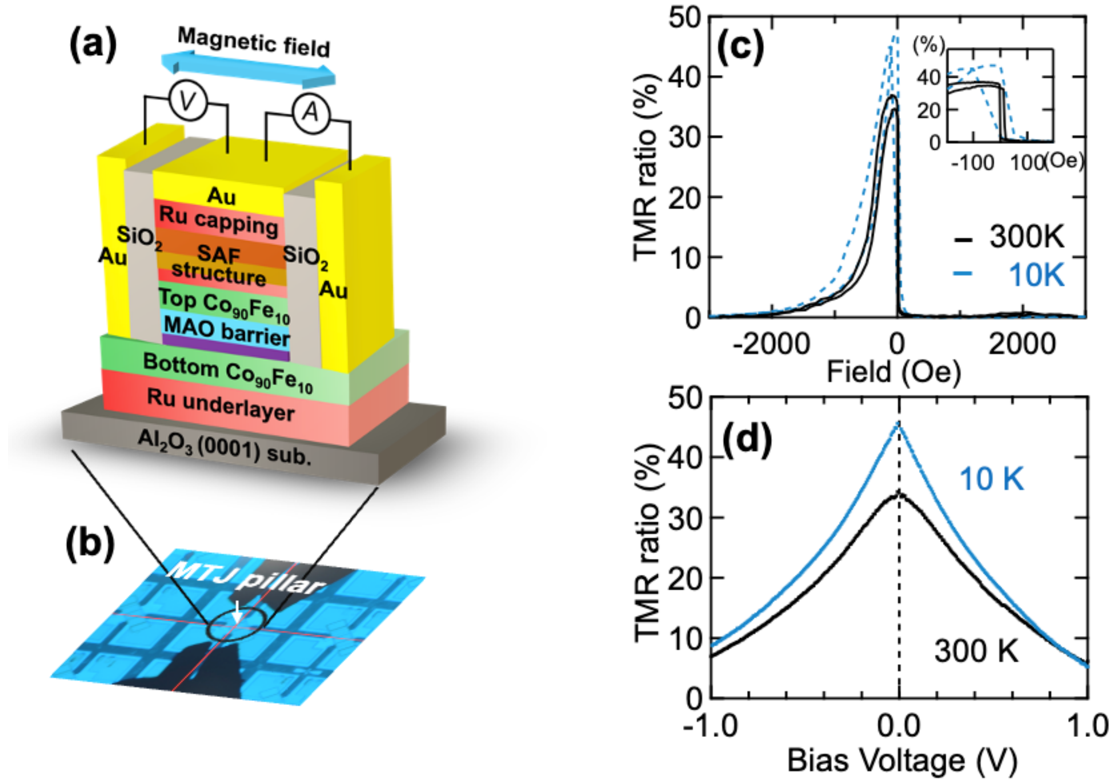

Figure. 3.9 (a) Schematic illustration of a patterned MTJ with the MTJ stack structure and the four-probe measurement setup. (b) Photo of the four-probe measurement configuration. (c) TMR-H curves at 300 K (solid, black) and 10 K (dashed, blue) of the MTJ. (d) Bias voltage dependence of TMR ratio at 300 K and 10 K. Inset of (c): TMR-*H* curves at a low field region.

Figures 3.9(a) and 3.9(b) show the magnetotransport four-probe measurement setup of a patterned MTJ. Figure 3.9(c) shows the TMR ratios as a function of in-plane magnetic field *H* measured along $Al_2O_3[10\bar{1}0]$ at 300 K (RT) and 10 K (bias voltage < 10 mV). Exchange spin-valve type loops were achieved using a synthetic antiferromagnetic (SAF) structure (i.e., $Co_{90}Fe_{10}$/Ru/$Co_{50}Fe_{50}$/IrMn) within the MTJ stack. TMR ratios of 37% at RT and 47% at 10 K were observed from this MTJ stack. The value of resistance area product (*RA*) for the P state at RT was ~ 2.7×10^6 Ω·μm^2, which is larger than the value of the recent Fe/MgO (2.75 nm)/Fe(001) MTJ

(~6×10^5 $\Omega\cdot\mu m^2$)[18]. This may indicate the difference in the transport mechanism compared with the conventional Δ_1 coherent tunneling. However, the observed TMR ratios are still much smaller than the theoretical value predicted in the Co/MgO/Co(111) which is around 2000%. The formation of the interfacial resonance states, which contribute to a large theoretical TMR ratio, can be significantly suppressed by the imperfections at FM/barrier(111) interfaces on both sides. These imperfections include misfit dislocations, atomic diffusion, and roughness, etc. Our STEM observations revealed many interfacial misfit dislocations and atomic steps at the CoFe/MAO interfaces due to the rather large lattice mismatch. These imperfections may significantly reduce the TMR ratio due to the absence of the interfacial effect in this MTJ. Further discussion about this MTJ stack especially the detailed microstructure analysis is reported collaborated with C. He et al.[82] The formation of an unexpected orientation of MgO (111) with a 30° in-plane rotation compared with the normal orientation from the theoretical model. This unexpected orientation has a rather smaller lattice mismatch which is around 3.4% and a volume fraction value of 26%. They also performed the density functional theory (DFT) calculation and proved a greatly suppressed TMR with this unexpected orientation which may further explain the low TMR observed in this study.

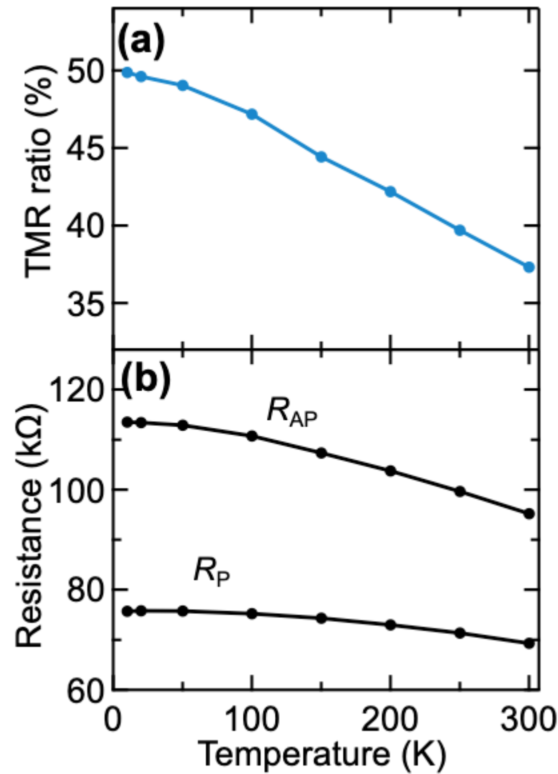

Figure. 3.10 (a) and (b) Temperature dependence of (a) TMR ratio and (b) R_P and R_{AP}.

Figure 3.10(a) (Fig. 3.10(b)) shows the temperature dependence of the TMR ratio (R_{AP} and R_P, where R_{AP} is the resistance of the antiparallel (AP) magnetization configuration and R_P is the resistance of the parallel (P) magnetization configuration). A monotonic increase in the TMR ratio was observed when decreasing temperature. Likewise, both R_{AP} and R_P show a monotonic increase as the temperature decreases. The temperature dependence of the TMR ratio is mainly determined by R_{AP} because R_{AP} shows a stronger change than R_P which is also reported in some conventional bcc(001) MTJs.[18,83] Note that the R_P increases slightly with decreasing temperature, which is in opposition to the highly (001)-oriented Fe/MgO/Fe and Fe/MAO/Fe MTJs with a slight decrease in R_P.[18,26]

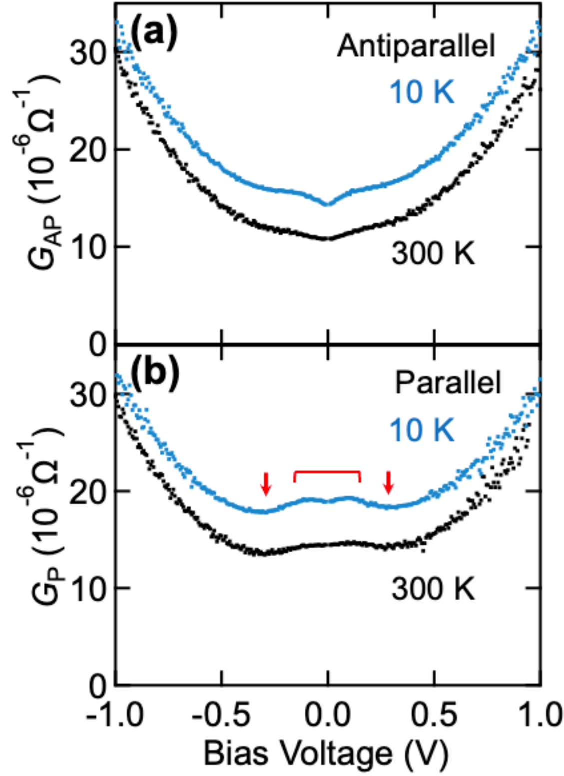

Figure. 3.11 (a) and (b) Conductance G spectra at 300 K and 10 K for (a) AP and (b) P states. For (a) and (b), the 10 K curves are shifted upward (by 4×10^{-6} Ω^{-1}) for comparison. The arrows and open square brackets in (b) are the local structures.

Figures 3.9(d) on the previous page and 3.11(a-b) show the bias voltage V dependences of 3.9(d) TMR ratio (TMR-V curve), 3.11(a) and 3.11(b) differential conductance G of the AP state (G_{AP}) and P state (G_P) at RT and 10 K. By calculating the derivatives of each current-voltage curve, the G_{AP} and G_P were obtained (i.e., dI/dV). Symmetric curves concerning the bias polarity were observed for all the graphs, indicating the achievement of almost identical quality of the lower and upper CoFe/MAO interfaces, i.e., similar interfacial electronic states. Similar to the conventional MTJs, the TMR-V curves exhibit a monotonic decrease with increasing $|V|$. The V at which a TMR ratio becomes half of the zero bias value, known as V_{half} values, were estimated to be 0.49 and –0.51 V (0.41 and –0.46 V) at RT (10 K) at the positive and negative bias polarities, respectively. There are no distinct structures in the TMR-V curves even at 10 K. In contrast, the conductance

curves exhibit some fine local structures. We observed some parabolic-like curves with a dip structure near zero bias in the G_{AP} curves, and the dip is more pronounced at 10 K. The dip at zero bias in the AP state may be attributed to the magnon-assisted inelastic tunneling, which is also observed in various MTJs.[84–86] In the RT G_P curve, a broad (bias-independent) plateau is observed in the range of V between –0.15 and 0.15 V as indicated by an open square bracket in Fig. 3.11(b). At 10 K, a small dip appears near zero bias and two pronounced local minimum structures were observed at $V \sim 0.28$ and ~ -0.26 V, as indicated by the arrows. It has been reported with similar local minimum structures in the G_P curve in bcc(001) CoFeB-based MTJs at around $|V| = 0.23 \sim 0.35$ V.[87,88] Currently, it is still unknown whether the origin of these local minimum structures in the G_P curves is similar in both the bcc(001) MTJ and the fcc(111) MTJ. To further investigate this behavior, more detailed information on the interface states will be obtained with the realization of fcc(111) MTJs with reduced interface imperfection. In general, the local structures in the G_P curve are a reflection of the tunneling processes through electronic states near the electrode/barrier interfaces.[89] Therefore, the transport process in the fcc(111) MTJ structures, which has the interfacial resonance tunneling mechanism, is supposed to be different from that in the bcc(001) MTJ structures. With the discovery of an unexpected orientation of the MAO barrier and the unreliable misfit dislocations at the interfaces, it is also expected that the reduction of the interfacial dislocation density and the unexpected stacking structure will be a key to improving the TMR ratio in the fcc(111) MTJs by enhancing the interfacial resonance tunneling. Utilizing lattice-matched systems by adjusting the MAO composition[90,91] and incorporating FM materials with larger lattice constants, such as CoPt and CoPd, will be a promising way to fabricate high-quality fcc(111) MTJs.[44]

3.4 Summary

A fully (111) epitaxial MTJ with CoFe/MAO/CoFe structure using a combination of magnetron sputtering and EB evaporation was successfully achieved. This is the first demonstration of the fcc (111) MTJ with TMR value observed. Although there is a large lattice mismatch between the CoFe and MAO, a high crystallinity stack with epitaxial MAO(111) barrier was obtained. The relatively flat MAO barrier interfaces were achieved by introducing the periodic misfit dislocations despite the rather large lattice mismatch. The TMR ratios of 37% at RT and 47% at 10 K were determined from this MTJ. The differential conductance curves of the MTJ have a symmetric behavior concerning bias polarity, indicating the well-balanced interfaces at both the lower and upper CoFe/MAO sides. In the differential conductance of the P state, observed local structures may reflect a specific interface structure from the fcc(111) interfaces; however, the small TMR ratios suggest that our MTJ stack does not contain a significant TMR enhancement induced by the interfacial resonance tunneling mechanism predicted theoretically. Nevertheless, this TMR demonstration with the realization of a fully epitaxial CoFe/MAO/CoFe(111) structure will accelerate the development of fcc(111)-based MTJs along with the conventional bcc (001) MTJ stack, which is significant for the next-gen high-density MRAM and highly sensitivity magnetic sensor applications.

Chapter 4 Perpendicular Magnetic Tunnel Junctions with a Non-integer Monolayer Controlled CoPt(111) layer and a MgO(111) Barrier

4.1 Introduction

As we mentioned in the first chapter of the development of MTJ from in-plane magnetization to perpendicular magnetization, for reducing size down to the 10nm dimension of MRAM application, PMA was indispensable for MTJ fabrication and application. Conventionally, the interface PMA from a thin CoFeB layer was used because of the large TMR effect following the coherent tunneling mechanism of the (001) structure. [2,4] However, this material system needs a critical control of the FM layer thickness which also affects the thermal stability. [29] Recently, a novel MTJ structure with Co-based PMA alloys, such as $L1_1$-CoPt and a MgO(111) barrier was theoretically predicted with TMR ratios over 2000% due to an interfacial resonant tunneling effect. [44] CoPt exhibits large magnetocrystalline anisotropy (K_u) along with a relatively low-temperature treatment around 300 °C especially for forming the $L1_1$ metastable phase. [31,92] Compared with the co-sputter method, monoatomic multilayer growth provides artificial superlattice formation and improved controllability and stability. [31] The utilization of multilayered CoPt featuring an fcc(111) MgO structure shows great potential for achieving a large TMR and PMA energy density.

In the previous chapter, a fully epitaxial fcc (111) MTJ with in-plane magnetization was successfully demonstrated and the barrier layer was fabricated by electron beam evaporation. And a rather large lattice mismatch was confirmed as 20% between the CoFe and MAO barrier although a 5:6 domain matching was observed. A large amount of periodic misfit dislocation appeared at the barrier interface which significantly decreased the TMR results compared with the giant TMR

by theoretical calculation. To further reveal the potential of (111) MTJ, a perpendicular magnetization FM layer is desirable such as Co/Pt or Co/Pd to achieve large bulk PMA effect. Compared with Co or $Co_{90}Fe_{10}$, CoPt also has a larger lattice constant which will reduce the mismatch with the barrier MgO layer from 20% to 13.5%. In this chapter, the Co/Pt multilayer structure was fabricated with various Pt content with optimized growth conditions while maintaining high flatness and crystallinity. Pressure dependence was characterized and a large PMA energy was achieved with increasing the growth pressure. MgO deposited by sputtering was also confirmed with (111) orientation and based on this structure, CoPt(111)/MgO(111) with CoFeB top layer and CoPt top layer were both realized as a perpendicular MTJ stack with TMR value observed. Detailed analysis of the flatness, crystallinity, microstructure, and transport properties will be shown in the following content.

4.2 Experiment procedures

In this work, we developed the epitaxial CoPt(111)/MgO(111) based p-MTJ with a non-integer monolayer controlled CoPt electrode with both CoFeB and CoPt as the top electrode. All stacks were deposited by magnetron sputtering on a single crystal sapphire(0001) substrate with a high-quality Ru underlayer of 40 nm. The treatment for the substrate is similar to the previous chapter results as a thermal cleaning in the muffle furnace at 1000 °C for 1 hour. And the Ru underlayer is also following a 1-hour degas with 345°C substrate heating and 850°C annealing for 1 hour. This is inside a different sputtering chamber system (EIKO) so the degas temperature is rather high at 850°C for removing the contamination from the holder and chamber inside. A series of CoPt samples with substrate/Ru 40nm/(Co 0.2 nm /Pt x nm)$_y$ multilayer/Ru 2nm cap stack were deposited with the total thickness of the CoPt layer fixed around 10nm for consistency. Here x

varies from 0.2~1 which is 1~5 ML of Pt, and *y* is the repeat number of Co/Pt layer as illustrated in Figure 4.4(a). The CoPt multilayers were deposited at 0.3 Pa Ar gas environment during the cooling process (monitored temperature is around 345°C) after the Ru annealing to maintain a stable temperature condition since the substrate heating may induce the fluctuation varied with the setting temperature.

The MTJ stack for the CoFeB top layer is substrate/Ru 40nm/(Co 0.2 nm /Pt 0.3 nm)$_{20}$ multilayer/Co 0.2nm/MgO 1.15nm/CoFeB 1.1nm/W 0.2nm/CoFeB 0.6 nm/MgO 1nm/Ta 5nm/Ru 12 nm. The bottom CoPt in the MTJ stack deposited at 2 Pa and after cooling down to RT, the following layers are all as-depo. After the deposition, the MTJ stack was *ex-situ* annealed at 350°C for 30 minutes to achieve the PMA of the top CoFeB layer. The double interfaces of the top CoFeB layer are utilized for stronger PMA. For the CoPt top layer p-MTJ, the stacking structure is substrate/Ru 40nm/(Co 0.2 nm /Pt 0.3 nm)$_8$ multilayer/Ru 0.9nm/(Co 0.2 nm /Pt 0.3 nm)$_8$ multilayer/Co 0.6nm/MgO 1.5nm/Co 0.6nm/Pt 1nm/(Co 0.2 nm /Pt 1 nm)$_3$ multilayer/Ru 12 nm. Here the bottom CoPt used a SAF structure as a pinned layer and deposited at 2 Pa. The top CoPt was deposited at 0.6 Pa for better flatness with a symmetric interface of 0.6nm Co for both the bottom and top.

The characterization is similar to the previous chapter such as the AFM, RHEED pattern, XRD, VSM, and STEM for the structural properties of surface morphology, crystallinity, and microstructure. Microfabrication and perpendicular four-probe measurements were conducted to analyze the transport properties. For CoFeB top layer p-MTJ, the pillar size is similar to the previous in-plane MTJ with a 39 μm^2 area elliptical structure. As for the CoPt top layer p-MTJ, a circle shape with 8×8 μm^2 and 4×4 μm^2 area pillars were fabricated.

4.3 Results and Discussions

4.3.1 Structural properties with $L1_1$ superlattice of Co/Pt multilayers

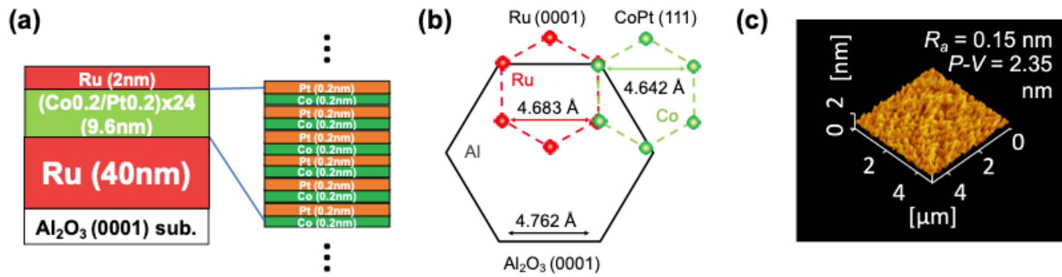

Figure 4.1 (a) Illustration of Co/Pt multilayer stack. (b) Epitaxial orientation relationships of Al_2O_3 (0001)/Ru (0001)/CoPt (111) (c) AFM image of Ru (40nm)/(Co 0.2nm/Pt 0.2nm)$_{24}$/Ru 2nm.

A sample stack with (Co 0.2nm/Pt 0.2nm) repetitively deposited 24 times on sapphire c-plane substrate/Ru 40 nm with a 2 nm Ru capping layer was demonstrated (Fig. 4.1(a)). The staking structure is substrate/Ru 40nm/(Co 0.2 nm /Pt 0.2 nm)$_{24}$ multilayer/Ru 2nm. As illustrated in Fig. 4.1(b). The well-defined epitaxial relationship for each layer from the substrate to CoPt provides a promising growth mode with almost perfect lattice matching. The optimization for the bottom layer is rather important for templating the upper layer growth, especially for the final MTJ stack. Figure 4.1(c) shows the 5×5 μm^2 area AFM image with very flat surface morphology of the CoPt multilayer with 0.2 nm Pt. The average roughness R_a = 0.15 nm and the peak-to-valley value P-V = 2.35 nm as listed on the graph.

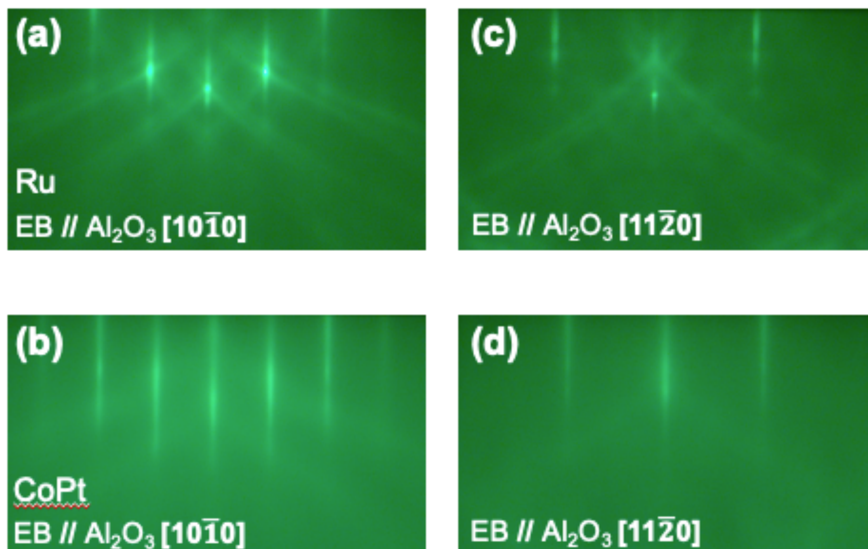

Figure 4.2 RHEED patterns of this sample. (a) Ru, (b) CoPt. The incident electron beam is parallel to the Al_2O_3[10$\bar{1}$0] azimuth. (c) Ru, (d) CoPt. The incident electron beam is parallel to the Al_2O_3[11$\bar{2}$0] azimuth.

The RHEED pattern of this stack was shown in Figure 4.2 with an incident electron beam along the Al_2O_3 [10$\bar{1}$0] azimuth for (a) bottom Ru, (b) CoPt, and incident electron beam along the Al_2O_3 [11$\bar{2}$0] azimuth for (c) Ru and (d) CoPt. The Ru underlayer has obviously distinct Kikuchi lines, indicating the high-quality Ru underlayer especially the high crystallinity was maintained due to the well-optimized deposition profile even with different sputtering systems. The 30-degree rotation with the incident beam along the substrate with the different patterns for Ru and CoPt proved the six-fold symmetry of the crystal orientation with the epitaxial growth of Ru (0002) and CoPt (111) which can also be confirmed by the XRD results in Fig. 4.4(b).

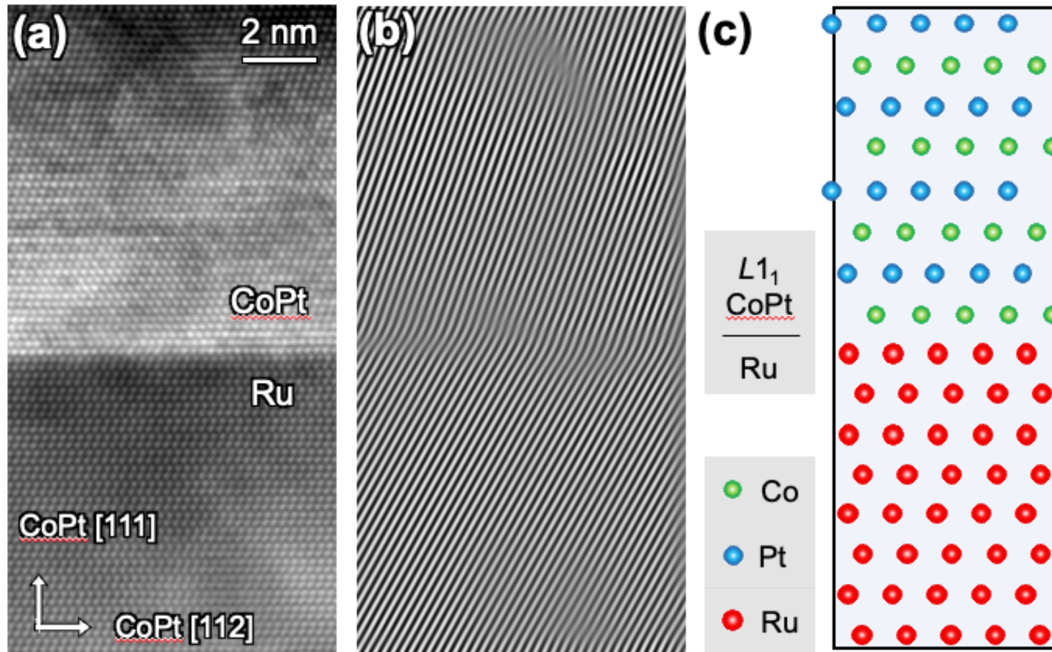

Figure 4.3 (a) Cross-sectional HAADF-STEM images of the Ru (40nm)/(Co 0.2nm/Pt 0.2nm)$_{24}$/Ru 2nm stack observed along $Al_2O_3[10\bar{1}0]$. (b) FFT filter images using (a). (c) Illustration of the interface atomic model.

The cross-sectional HAADF-STEM image of this stack with a 0.2 nm Pt layer is shown in Figure 4.3. From the FFT-filtered image in Figure 4.3(b), a perfect lattice matching with a misfit dislocation-free interface was observed, which follows our designed epitaxial relationship in Figure 4.1(b). The illustration of this misfit dislocation-free structure is also shown in Figure 4.3(c). In this HAADF-STEM image, the atoms such as Pt with higher atomic numbers produce brighter image contrast. At the right-up region of the CoPt layer shown in Fig. 4.3(a), a $L1_1$ like structure of CoPt can be observed from the exchange contrast from Pt and Co with brighter or darker behavior which proved the successfully formed $L1_1$-like ordered structure at this region. Near the bottom interface between Ru and CoPt at the left-bottom part, although the homogenous brightness confirms the disordered fcc structure of CoPt, an atomically flat interface at both the bottom and top is achieved for the CoPt layer which is important as the electrode for an MTJ stack.

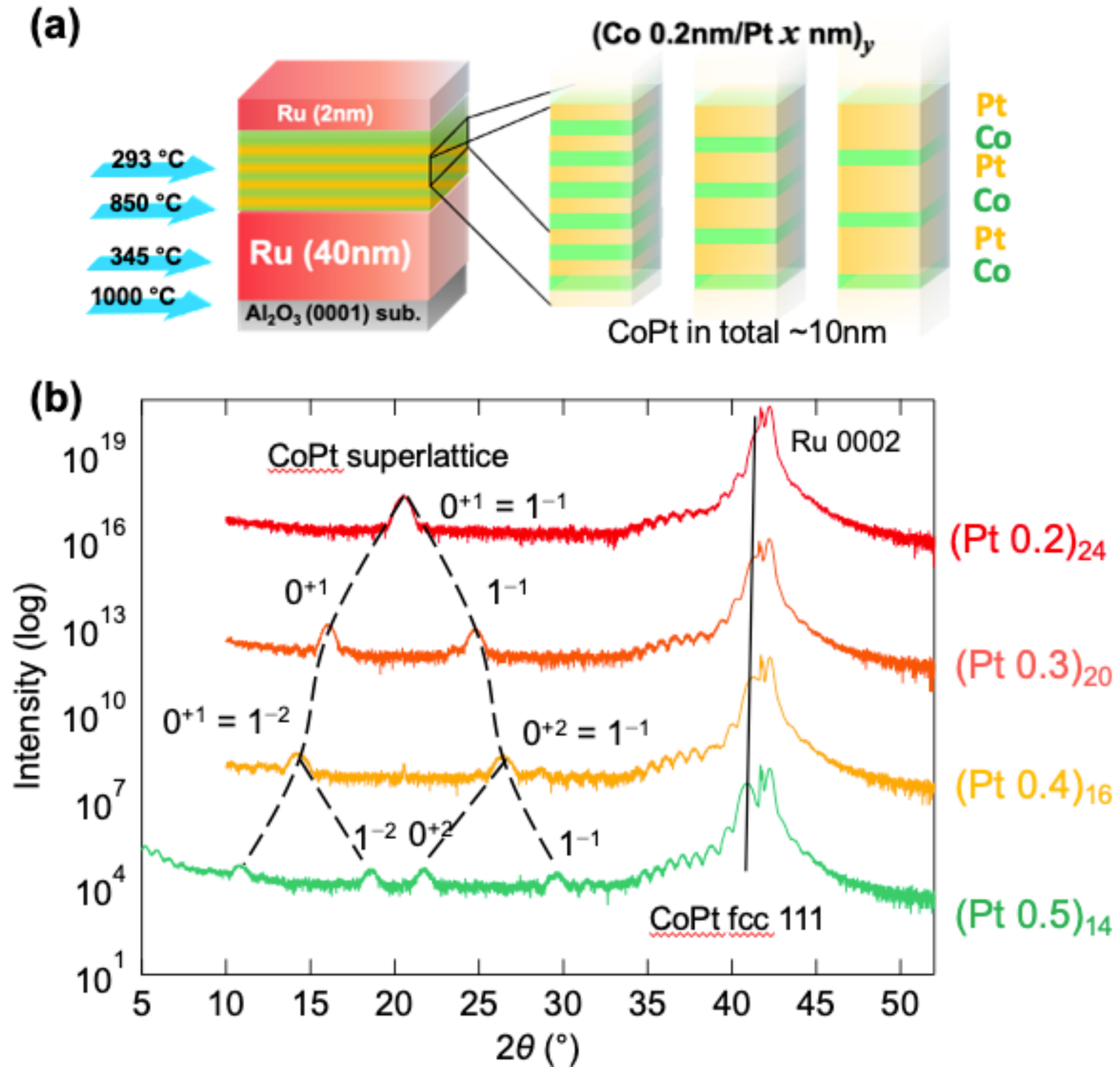

Figure 4.4 (a) illustration of Co/Pt multilayer stack with temperature profile. (b) XRD profiles for substrate/Ru 40nm/(Co 0.2 nm /Pt x nm)$_y$ multilayers (x and y are listed on the graph). The labels 0^{+1} and 1^{-1} represent the 1st-order satellite peak of the fundamental peak and the −1st-order satellite peak of the fundamental peak, respectively.

Figure 4.4(b) shows the XRD out-of-plane results from the CoPt multilayers with various Pt concentrations from 0.2 nm to 0.5nm with the stacking model illustrated in Fig. 4.4(a). The total thickness of CoPt was fixed around 10 nm. The correspondent Pt atomic ratios are calculated as

43%, 53%, 60%, and 65%. One monolayer (ML) for Co is calculated as 0.21 nm and 1 ML for Pt is defined as 0.23 nm, for our results we choose 2 nm for each for simplicity. From the XRD results in Fig. 4.4(b), the superlattice CoPt peak associated with $L1_1$ ordered structure can be observed at 20.7° and the corresponding d spacing is 0.43 nm for Pt 0.2 nm sample, which is consistent with Co 1ML/Pt 1ML. With increasing the Pt thickness, this superlattice peak split into a couple of satellite peaks as indexed on the graph. The labels 0^{+1} and 1^{-1} represent the 1st-order satellite peak of the fundamental peak and the −1st-order satellite peak of the fundamental peak, respectively. For the Pt 0.3 nm sample, the two satellite peaks have d-spacing with 0.55 nm and 0.36 nm which corresponds to the 2θ at 16.1° and 26.7°. This peak splitting behavior with non-integer controlled ML deposition has been observed from some thin films fabricated by molecular beam evaporation (MBE) which confirms the well-defined layer-by-layer growth and very flat interfaces. [93] The results from our multilayered samples revealed that it can also be achieved by our sputtering technique and this well-defined layer-by-layer growth with flat interfaces is desirable for the MTJ stack.

4.3.2 Magnetic properties of Co/Pt multilayers

The magnetic properties with various Pt content of substrate/Ru 40nm/(Co 0.2 nm /Pt x nm)$_y$ multilayer/Ru 2nm cap stack with CoPt deposited at 0.3 Pa was illustrated in Fig. 4.5(a-f). The thickness of Pt and the repeat numbers were listed on each graph. The measurement was conducted by VSM and the magnetization was calculated from the magnetic moment with the nominal thickness and the film area size. The PMA effect can be observed for Pt thickness from 0.2 nm to 0.6 nm. The out-of-plane hysteresis loops show sharp magnetization reversals with nice squareness. Only the (Co 0.2 nm /Pt 1 nm)$_8$ multilayer showed no PMA. The decreased saturated magnetization proved the large amount of Pt which is calculated to be 79%.

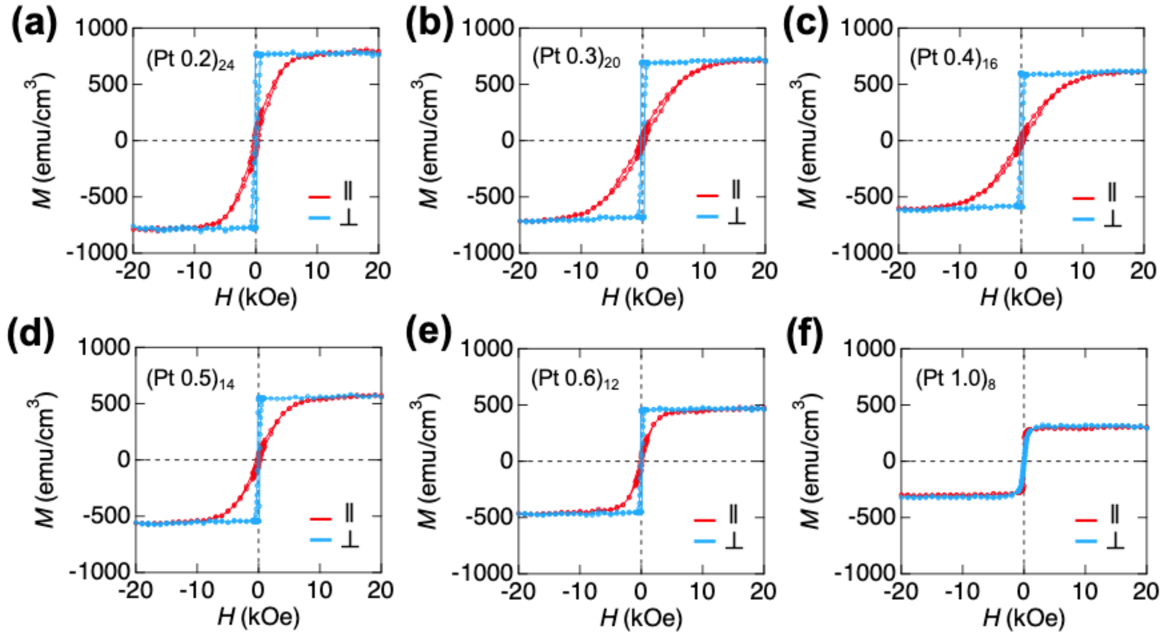

Figure 4.5 (a-f) Hysteresis loops of substrate/Ru 40nm/(Co 0.2 nm /Pt *x* nm)$_y$ multilayers (*x* and *y* are listed on the graph).

The result of H_k, M_s, and K_u as a function of Pt content was plotted in Figure 4.6 and the PMA energy $K_u = M_s H_k/2$ was estimated by the anisotropy filed H_k and the saturation magnetization M_s from the in-plane and out-of-plane magnetization hysteresis loop (*M-H* loop) as illustrated in Fig. 4.5 measured by VSM. The maximum of H_k and M_s showed up at around 50% of Pt content which is consistent with the reference which used a co-sputter method. [92] The saturated magnetization gradually decreased from 796 to 320 emu/cm^3 with an increase in the Pt composition from 43% to 79%. The coercivity varies from 150 to 300 Oe and follows a similar trend as the PMA energy value. This result proved that our multilayer structure reproduced the co-sputter results with well-controlled monolayer growth. This is a fundamental study that can be used for p-MTJ development towards better PMA realization. The current Ku value is equal to 0.35 MJ/m^3 which is still smaller compared with the 3.7 MJ/m^3 from the *L*11 CoPt [92].

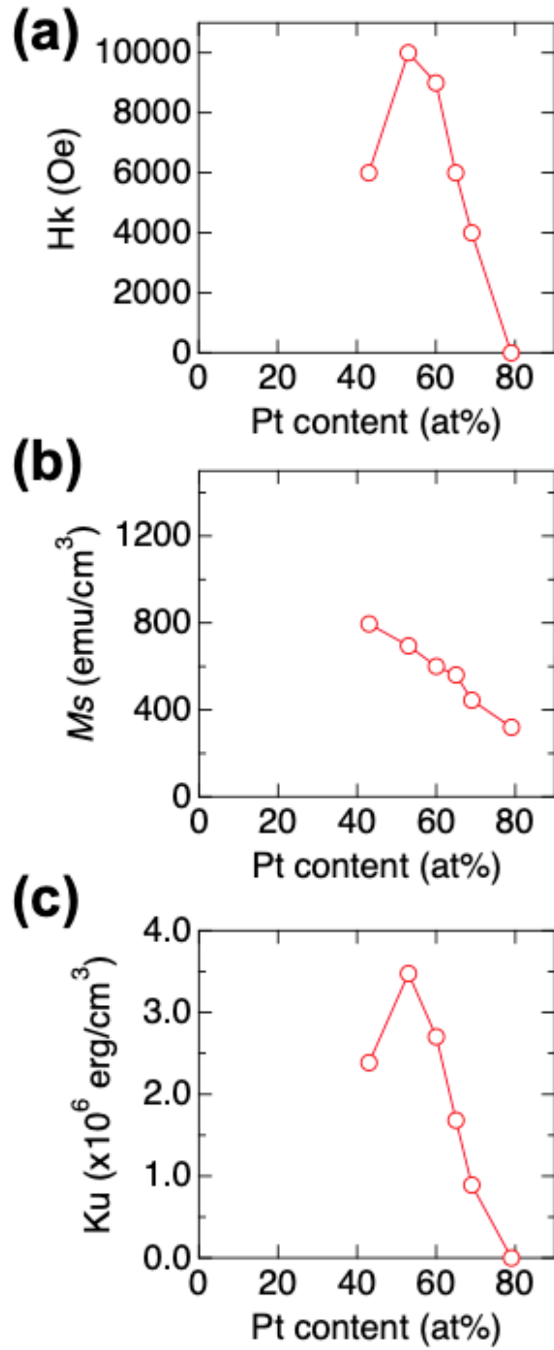

Figure 4.6 (a) H_k, (b) M_s, and (c) K_u as a function of Pt content.

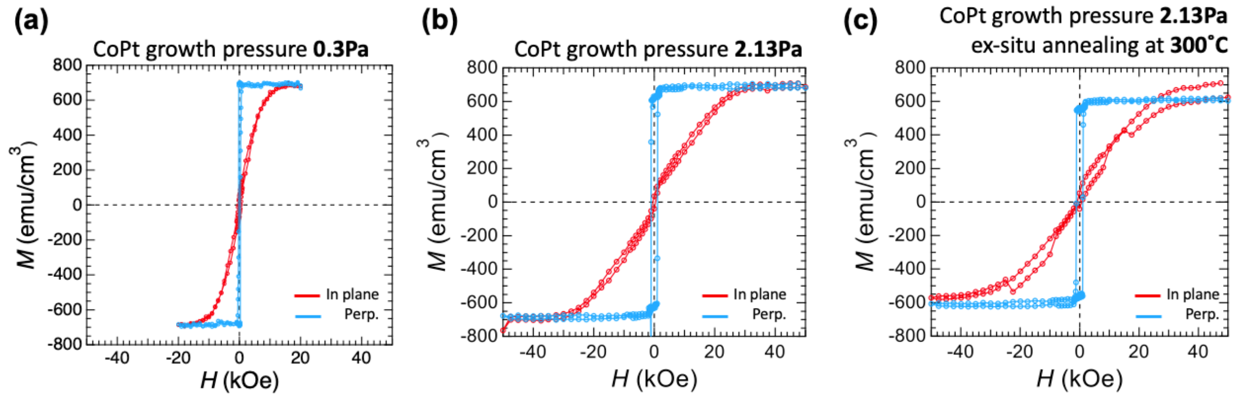

Figure 4.7 Hysteresis loop of substrate/Ru 40nm/(Co 0.2 nm /Pt 0.3 nm)$_{20}$ with different growth temperatures and annealing condition (a) 0.3 Pa growth (b) 2.13 Pa growth (c) 2.13 Pa growth and ex-situ annealed at 300 ˚C

As we mentioned, it is necessary to get a large PMA energy density with several MJ/m^3. The pressure dependence of substrate/Ru 40nm/(Co 0.2 nm /Pt 0.3 nm)$_{20}$ stack which has the maximum PMA with Pt 53% composition was characterized and shown in Figure 4.7 with annealed condition behavior. It is obvious that increasing pressure leads to enhanced PMA energy and annealed at 300 ˚C further yields a maximum of 1.12 MJ/m^3. This value is accessible for the MTJ development and the 1×1 μm^2 AFM result also proved the flat surface of this bottom electrode CoPt with R_a = 0.2 nm and P-V = 2.18 nm which is flat enough for the MTJ demonstration. The enhanced PMA with higher pressure is supposed to be explained by the improved (111) texture or increased interface roughness[94]. The contribution of the PMA with a multilayered structure is rather difficult to determine which may be beyond the scope of our MTJ development.

4.3.3 Structural properties of CoPt/MgO/CoFeB stack

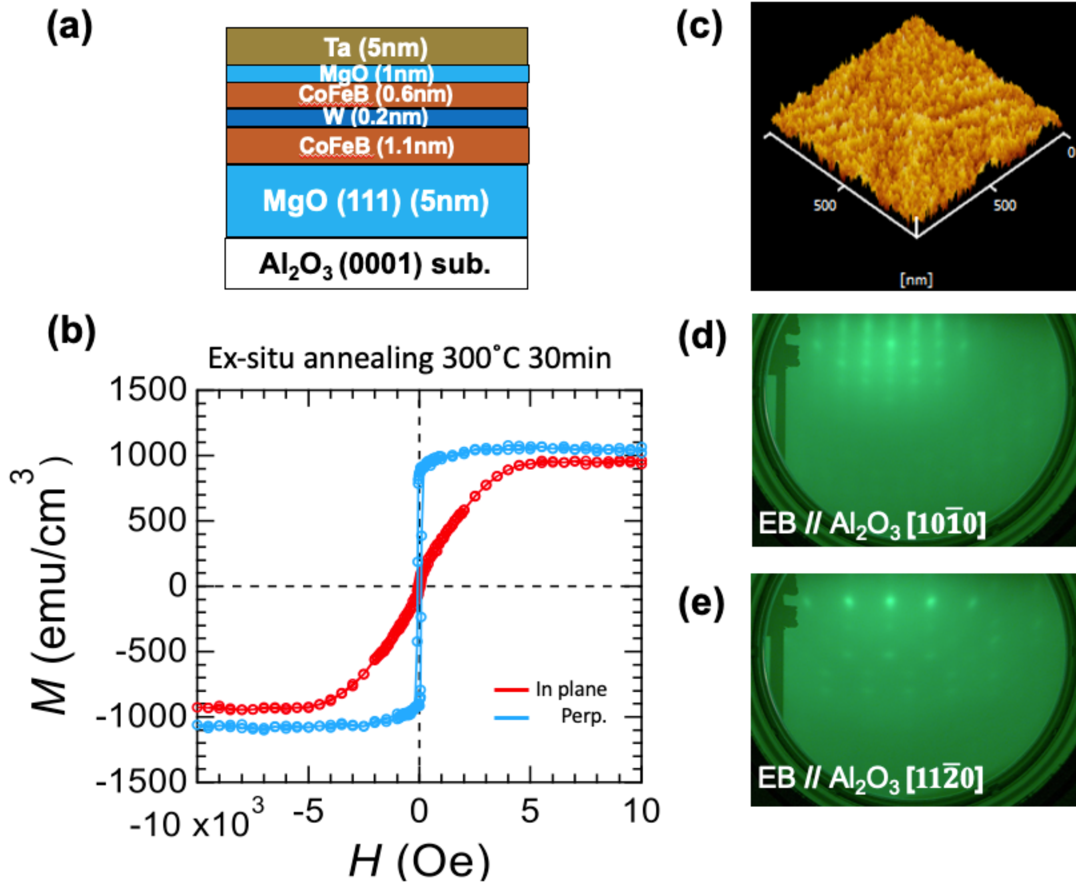

Figure 4.8 (a) Illustration of substrate//MgO 5nm/CoFeB 1.1nm/W 0.2nm/CoFeB 0.6nm/MgO 1nm/Ta 5nm stack. (b) Hysteresis of this stack after ex-situ annealed at 300 ˚C. (c) AFM image of substrate//MgO 5nm (d-e) RHEED pattern of sputtered MgO (111). The incident electron beam is parallel to the (d) $Al_2O_3[10\bar{1}0]$ azimuth and (e) $Al_2O_3[11\bar{2}0]$ azimuth.

To achieve a perpendicular MTJ stack, the MgO barrier and top FM layer also need to be developed. Firstly, 5 nm sputtered MgO was characterized on the flat surface of the baked sapphire substrate. An epitaxial growth was confirmed by the RHEED patterns in Figure 4.8 (d-e) with sapphire//MgO 5nm structure. A flat surface is also shown in Figure 4.8(c) with R_a = 0.06 nm and P-V = 0.64 nm. These results proved again our optimization method for substrate treatment is indispensable for the following layers' growth. On this MgO buffer layer, CoFeB as a top layer was deposited with the double interface for stronger PMA as shown in Figure 4.8(a) with the stacking structure of

CoFeB 1.1nm/W 0.2nm/CoFeB 0.6 nm/MgO 1nm/Ta 5nm. We varied the first CoFeB layer thickness from 0.9 nm to 1.2 nm and all of them showed PMA but the 1.1 nm has the best squress from the out-of-plane VSM measurement. The VSM results were shown in Figure 4.8(b) after *ex-situ* annealed at 300 ˚C for 30 min. The H_k, K_u, and H_c for this top PMA layer are 4500 Oe, 0.23 MJ/m^3, and 100 Oe. Such a small coercivity is essential as a free layer. For achieving a perpendicular MTJ stack, the top PMA was successfully achieved on the MgO (111) layer which proved that even with (111) MgO, the conventional CoFeB top layer is also accessible as a perpendicular top layer.

4.3.4 Microstructure analysis and transport properties of CoPt/MgO/CoFeB stack

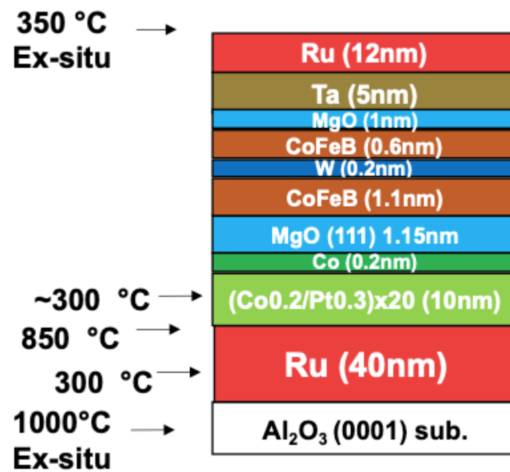

Figure 4.9 Illustration of CoPt/MgO/CoFeB MTJ stack.

A perpendicular MTJ stack was fabricated with CoFeB/W/CoFeB/MgO for top perpendicular magnetization as shown in Fig. 4.9 with the growth condition and *ex-situ* annealed condition. From our previous step-by-step development for this MTJ stack, the perpendicular MTJ was successfully achieved with fcc CoPt (111)/MgO (111) bottom structure.

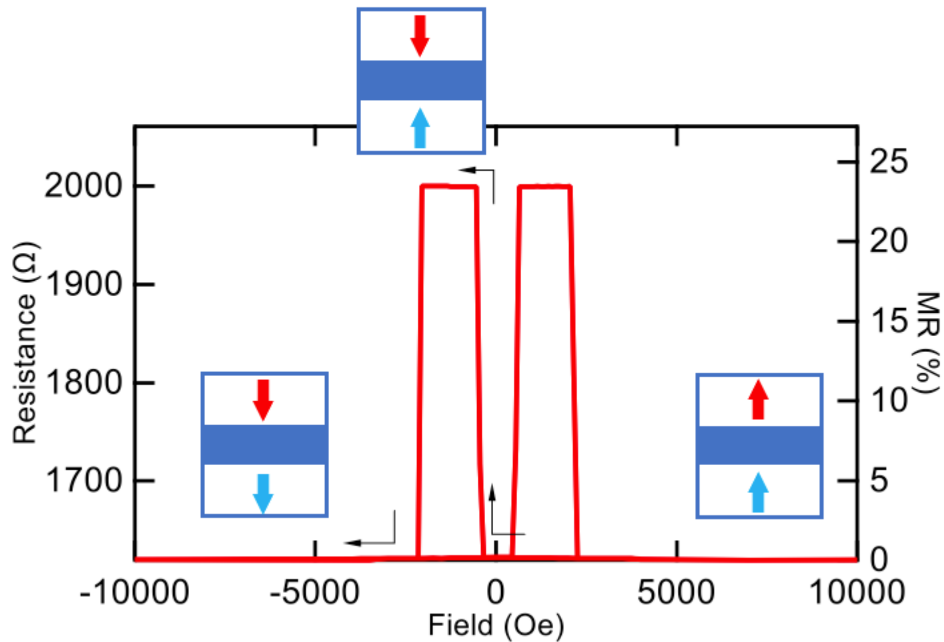

Figure 4.10 Resistance and MR as a function of the magnetic field at RT. The magnetization configuration was illustrated.

TMR value was measured with the four-probe method on a patterned wafer. Figure 4.10 showed the *R*-*H* curve with a flat AP state with a perpendicular magnetic field which confirmed the stable and reliable MR measurement. The TMR value was calculated as 24%. These stable results proved the demonstration of each layer was successfully achieved. Due to the small coercivity of CoFeB compared with bottom CoPt, the AP state was stable enough to maintain a stable TMR observation. To further reveal the microstructure of this MTJ stack and discuss the small TMR ratio compared with the desirable thousand percent value, HAADF-STEM observation was conducted for this MTJ stack as shown on the following page.

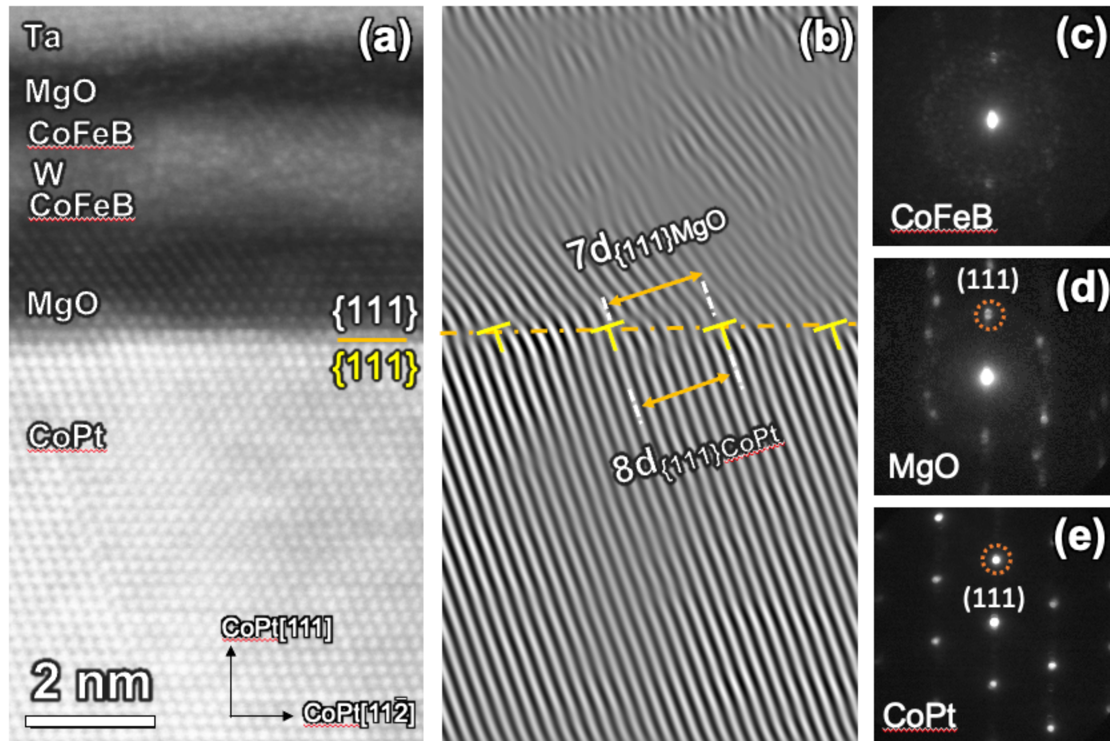

Figure 4.11 (a) Cross-sectional HAADF-STEM images of the MTJ stack observed along Al_2O_3[10$\bar{1}$0], orange lines indicate the {111} planes of CoPt and MgO. (b) FFT filter images using (a). ⊥ Marks in (b) indicate the lattice dislocations at the interface. (c-e) NBED patterns for (c) top CoFeB, (d) MgO barrier, and (e) bottom CoPt.

The cross-sectional HAADF-STEM images are shown in Fig. 4.11. The CoPt (111)/MgO (111) epitaxial growth was successfully observed in Fig. 4.11(a) and a relatively flat interface was also achieved even with a growth pressure of 2 Pa for the bottom layer. The FFT filter image is shown in Figure 4.11(b). The lattice constant for MgO and CoPt are determined to be 0.42 nm and 0.37 nm which is similar to the bulk value. The lattice mismatch is calculated to be 13.5% which is reduced compared with the 20% of the CoFe/MAO in-plane MTJ in Chapter 3. A periodic misfit dislocation was introduced at the CoPt/MgO interface with 7:8 matching and reduced mismatch with 1% which maintains the epitaxial growth of the MgO layer. This epitaxial relationship was confirmed again by NBED observation in Figure 4.11(d-e) for the (111) orientation of the bottom

CoPT and MgO barrier, the top CoFeB is amorphous. Due to the uncompleted (111) MTJ structure with an amorphous CoFeB top layer, the interfacial resonance tunneling mechanism from fully fcc (111) MTJ was not introduced within this MTJ structure which is the main reason for the small TMR ratio. And the demonstration of a fully fcc (111) perpendicular MTJ stack is desirable.

4.3.5 Fully fcc(111) perpendicular MTJ with CoPt/MgO/CoPt stack

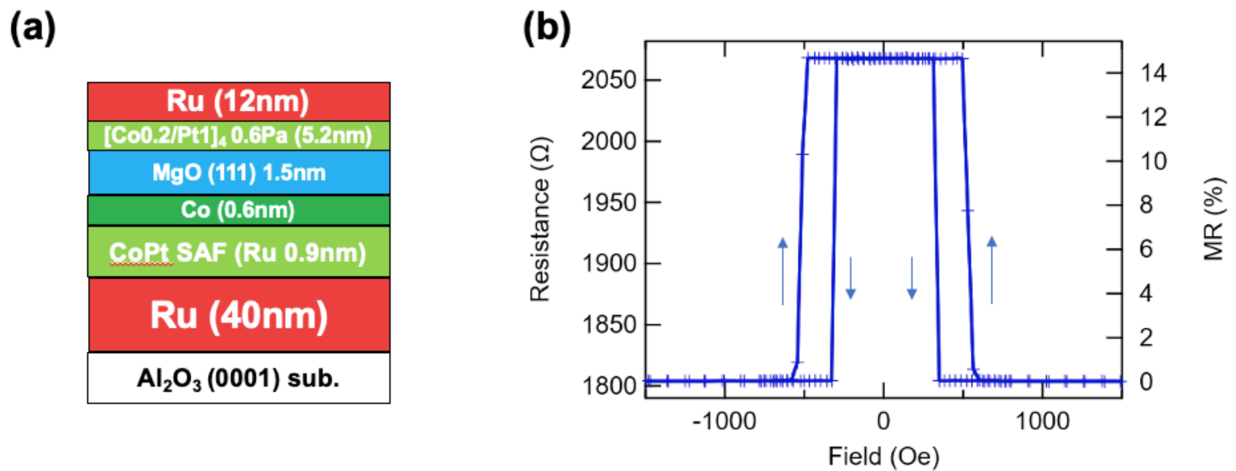

Figure 4.12 (a) Illustration of CoPt/MgO/CoPt MTJ stack. (b) Resistance and MR as a function of the magnetic field at RT. Arrows here represent the measured direction.

Following the demonstration of the CoPt/MgO/CoFeB p-MTJ, a fully fcc (111) structure was fabricated with stacking structure as substrate/Ru 40nm/(Co 0.2 nm /Pt 0.3 nm)$_8$ multilayer/Ru 0.9nm/(Co 0.2 nm /Pt 0.3 nm)$_8$ multilayer/Co 0.6nm/MgO 1.5nm/Co 0.6nm/Pt 1nm/(Co 0.2 nm /Pt 1 nm)$_3$ multilayer/Ru 12 nm. The bottom SAF structure was successfully established as the AP state was realized before the free layer switching. A relatively thick Co insertion layer was used since the interface resonance tunneling was predicted between the Co and O elements. The top CoPt layer was deposited with a relatively thick Pt layer for reducing the repeating sequence at 0.6 Pa, otherwise, a stable PMA on the MgO (111) layer is rather difficult to grow due to the degraded

flatness from the MgO layer. The TMR value shown in Figure 4.12(b) was calculated as 15% from an 8 × 8 μm^2 size pillar, this is the first demonstration of a fully CoPt/MgO/CoPt(111) perpendicular MTJ with observed TMR value. Due to the large lattice mismatch which is over 10% even if we changed from CoFe to CoPt, this large value of mismatch leads to the innegligible interface roughness with a large amount of misfit dislocations and suppresses the interfacial resonance tunneling effect with giant TMR ratio.

4.4 Summary

For downscaling below 10nm for industrial applications, perpendicular MTJ is desirable and the misfit dislocation needs to be reduced by reducing lattice mismatch between FM and barrier. We combine the multilayered CoPt with a monolayer controlled structure with a precisely controlled deposition profile with a high-quality Ru underlayer on a thermal cleaned single crystal sapphire substrate. With different Pt concentration characterization, the peak splitting from XRD out-of-plane observation indicated the non-integer monolayer controlled structure with layer-by-layer growth and sharp interfaces which is suitable for the MTJ stack. The PMA energy up to 1 MJ/m^3 was achieved at high deposition pressure with annealed at 300 °C but maintained the flatness of the surface. Based on the atomically flat surface structure and high crystallinity of the bottom CoPt multilayer, the CoPt(111)/MgO(111)/CoFeB perpendicular MTJ was fabricated with 24% MR observed, and a flat AP state due to the small coercivity from the top CoFeB PMA layer. The discrepancy between the experimental value and the theoretical value can be explained by the imbalanced MTJ structure between the bottom CoPt and the top CoFeB layer which is not a fully fcc (111) MTJ. Furthermore, by utilizing a bottom-SAF structure with a thinner top Pt-rich CoPt and symmetric interface Co layer, a fully perpendicular fcc (111) MTJ with CoPt/MgO/CoPt(111)

structure was achieved and a 15% TMR was observed. Although the 13.5% lattice mismatch still induced a large number of misfit dislocations the formation of interface defects greatly suppressed the interfacial resonance tunneling and the large TMR effect. This first demonstration of a fully fcc (111) perpendicular MTJ paved a new direction for the realization of giant TMR and PMA effect apart from the conventional (001) MTJ with only interface-induced PMA.

Chapter 5 Charge-to-spin conversion in fully epitaxial Ru/Cu hybrid nanolayers with interface control

5.1 Introduction

Recently, light metals with better stability and larger conductivity are attracting attention for the spin current generation, [74,95] which can be considered promising candidates for spin-orbit devices. Generally, most of them exhibit negligible SHE effects in their bulk states, as validated for Cu [96,97], and Ru [98], which have negligible spin Hall efficiencies. However, it has been discovered that the atomic-level oxidation of Cu can generate a large spin current with a comparable ξ_{SH} value to Pt, which can be explained by the spin vorticity coupling (SVC) of the electron mobility gradient [74], or the enhanced interfacial SOIs, such as Rahsba effect. [95,99,100] Furthermore, interfacial and layered structure configuration engineering in light-metal-based heterostructures also produces substantial spin currents. [101–104] Jamali *et al.* reported the enhanced SOTs efficiencies in multilayer Co/Pd stacking, owing to a probable bulk contribution from the multilayers. [101] Theoretically, Amin *et al.* proposed two theoretical mechanisms for the generation of spin current at the interface between two NMs (i.e., NM1/NM2) and the NM/FM interface, namely the spin filtering effect and the spin precession effect. [102] Experimentally, Baek *et al.* reported the interface-generated spin currents in the CoFeB/Ti and NiFe/Ti bilayer structure systems. [103] Additionally, it was demonstrated that the sign and magnitude of the spin currents could be modified by adjusting the electrical conductivity between the two materials forming the interface. [104] These results highlight the significant potential of precisely controlled nanostructures and interfaces in enhancing spin-charge conversion efficiency. To date, most of the above studies have focused on polycrystalline systems, which exhibit less controllable properties due to the grain boundaries and structural

imperfections. It is of scientific interest to explore epitaxial materials with atomic-scale microstructure analysis for the effective control of the nanolayer structures and interfaces in spin-charge conversion.

In this section, highly conductive Ru/Cu epitaxial thin films with nanolayer [Cu (1 nm)/Ru (1 nm)]$_n$ (n = 0, 1, 2) insertions were prepared for inducing a spin current generation. The atomic-scale crystal structures were characterized in detail. A sizable effective damping-like spin Hall efficiency (ξ_{DL}) with a significant effective spin Hall conductivity in a similar range with Pt was demonstrated by the measurements of unidirectional spin Hall magnetoresistance (USMR) and spin-torque ferromagnetic resonance (ST-FMR) methods. The sharp interface between Ru and Cu, as well as the nanolayer-insertion structures, demonstrated the substantial ability to convert charge current to spin current in this fully epitaxial Ru/Cu system [73].

5.2 Experiment procedures

The Ru/Cu thin films were deposited on single-crystal sapphire Al_2O_3(0001) substrates using a magnetron sputtering apparatus (ULVAC, Inc.) at a base pressure of 4 × 10^{-7} Pa with depositing Ru and Cu multiple times. The substrates were baked *ex-situ* at 1000 °C for 1 hour in a conventional muffle furnace (AS ONE HPN-ON) to perform the thermal cleaning, which removed the surface contamination of the substrates and improved a better flatness. In the vacuum chamber, the substrates were degassed at 300 °C for 1 hour, then the deposition was performed with an Ar pressure of 0.1 Pa. The sputtering power for each target was as follows: Ru: direct current (DC) 38 W, Cu: radio frequency (RF) 30 W, and $Ni_{81}Fe_{19}$ (NiFe): DC 18 W. The corresponding deposition rates are 0.41 Å/s for Ru, 0.25 Å/s for Cu, and 0.21 Å/s for NiFe. To enhance the surface morphology and crystallinity, each deposition step was meticulously controlled using different

temperature treatments, as depicted in Fig. 1(a). The Ru bottom layer was deposited at 300 °C. The $[Cu/Ru]_n$ layer as well as the Cu, and NiFe layers were deposited at room temperature (RT), where n represents the number of periods. *In-situ* post-annealing was performed at 550 °C for the Ru bottom layer, 300 °C for the thick Cu layer, and 200 °C for the NiFe layer. The post-annealing was carefully controlled with various conditions as we did in the previous chapters. The summary of 5×5 μm^2 area AFM results with annealing temperature varied from 500 ~ 600°C for the Cu (1nm)/Ru (1nm) layer was shown in Table. 5.1. The lowest value was obtained from the 550°C annealing and this condition was utilized for the Ru/Cu heterostructure stacks.

5×5 μm^2 AFM	**500 °C**	**550 °C**	**600 °C**
R_a (nm)	0.19	**0.16**	0.51
P-V (nm)	2.82	**2.03**	20.42

Table 5.1. Summary of the 5×5 μm^2 AFM results of Al_2O_3 substrate//Ru (9nm)/Cu (1nm)/Ru (1nm)/Cu (9nm)/$Ni_{81}Fe_{19}$ (5nm)/MgO (2nm) with different annealing temperatures for the Cu (1nm)/Ru (1nm) layer. The lowest values were made in bold font.

All samples were characterized using *in-situ* reflection high energy electron diffraction (RHEED) and *ex-situ* atomic force microscopy (AFM) measurement. The microstructure analysis was carried out using high-resolution high-angle annular dark-field scanning transmission electron microscopy (HAADF-STEM), nano-beam electron diffraction (NBED), and the energy dispersive X-ray spectroscopy (EDS) utilizing an FEI Titan G2 80–200 ChemiSTEM instrument.

Through the microfabrication using photolithography and Ar-ion milling, the films were patterned into Hall bar structures (width: 10 μm, length: 25 μm) for USMR measurements and rectangular

structures (width: 10 μm, length: 40 μm) for ST-FMR measurements. For the USMR measurements, an alternating current at a frequency of f = 227 Hz was applied, along with an external in-plane magnetic field varying between –3000 and 3000 Oe. Then, the longitudinal resistance $R_{xx}^{2\omega}$ and the transverse resistance $R_{xy}^{2\omega}$ were measured using a lock-in amplifier (nf LI5660). As for the ST-FMR measurements, a 15 dBm RF power in the frequency range of f = 7–15 GHz was applied from a signal generator (Keysight E8257D), with an external in-plane magnetic field swept from 0 to 3000 Oe. Additionally, in-plane angular dependence was performed with φ = 0–360°. All transport measurements were conducted at RT.

5.3 Results and Discussions

5.3.1 Structural properties of Ru/Cu heterostructure

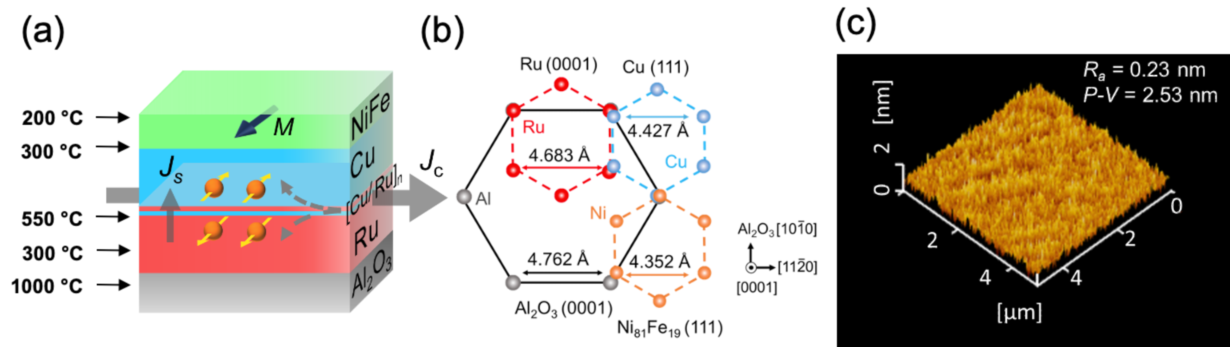

Figure 5.1 (a) Illustration of the sample stack. (b) Epitaxial orientation relationships between Al_2O_3 (0001)/Ru (0001)/Cu (111)/$Ni_{81}Fe_{19}$ (111). (c) AFM image for the Al_2O_3 substrate//Ru (10nm)/Cu (10nm)/$Ni_{81}Fe_{19}$ (5nm)/MgO (2nm) sample surface. R_a and *P-V* indicate the average roughness and the peak-to-valley values, respectively.

We prepared three samples with [Cu (1 nm)/Ru (1 nm)]$_n$ nanolayer insertion between a typical bilayer consisting of Ru and Cu with similar thickness, where n is 0, 1, and 2. The total thickness

of the bottom Ru-Cu NM layer was fixed at 20 nm. A 5 nm NiFe layer was deposited as the FM layer for the detection of spin current. The schematic stacking structure is shown in Fig. 5.1(a). Figure 5.1(b) indicates the epitaxial relationship of Al_2O_3(0001)/Ru(0001)/Cu(111)/NiFe(111). From bottom to top, only small bulk lattice mismatches were shown between these atomic planes, and the values are –1.66%, –5.47%, and +2.62%, respectively. The optimized fabrication conditions for each layer were shown in the graph and a flat surface was achieved for the Al_2O_3 substrate//Ru (10 nm)/Cu (10 nm)/NiFe (5 nm)/MgO cap (2 nm) heterostructure, as shown in Fig. 5.1(c). The average roughness (R_a) is around 0.23 nm and the peak-to-valley (P-V) value is ~2.53 nm obtained from the AFM image for a 1×1 μm^2 area scan. The other two stacks also have the same flatness quality with R_a < 0.3 nm and P-V < 2.6 nm values.

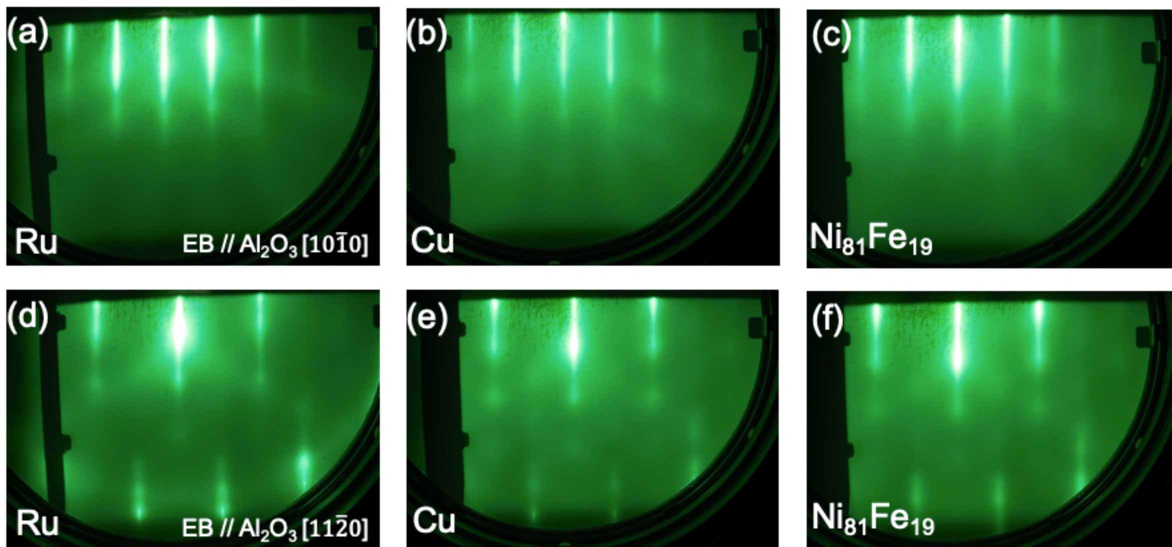

Figure 5.2 (a) RHEED patterns of Ru layer, (b) Cu layer, and (c) $Ni_{81}Fe_{19}$ layer, the incident electron beam is parallel to the Al_2O_3 $[10\bar{1}0]$ direction. (d) RHEED patterns of the Ru layer, (e) Cu layer, and (f) $Ni_{81}Fe_{19}$ layer, the incident electron beam is parallel to the Al_2O_3 $[11\bar{2}0]$ direction. All observations were performed after the post-annealing process.

Figures 5.2(a-c) are the RHEED patterns with incident electron beam parallel to $Al_2O_3[10\bar{1}0]$ direction. The Ru, Cu, and NiFe layers exhibit sharp streaks with obvious Kikuchi lines, indicating

a single crystal structure of the film stacks. The RHEED patterns observed along the $Al_2O_3[11\bar{2}0]$ direction are shown in Figs. 5.2(d-f), where the different positions of the streaks confirm the six-fold epitaxial growth of hcp Ru(0002)/fcc Cu(111)/fcc NiFe(111) structure, consistent with the designed stacking (Fig. 5.1(b)). The well-defined surface flatness and crystallinity are crucial for the steadiness and reliability of the following spin-transport measurements.

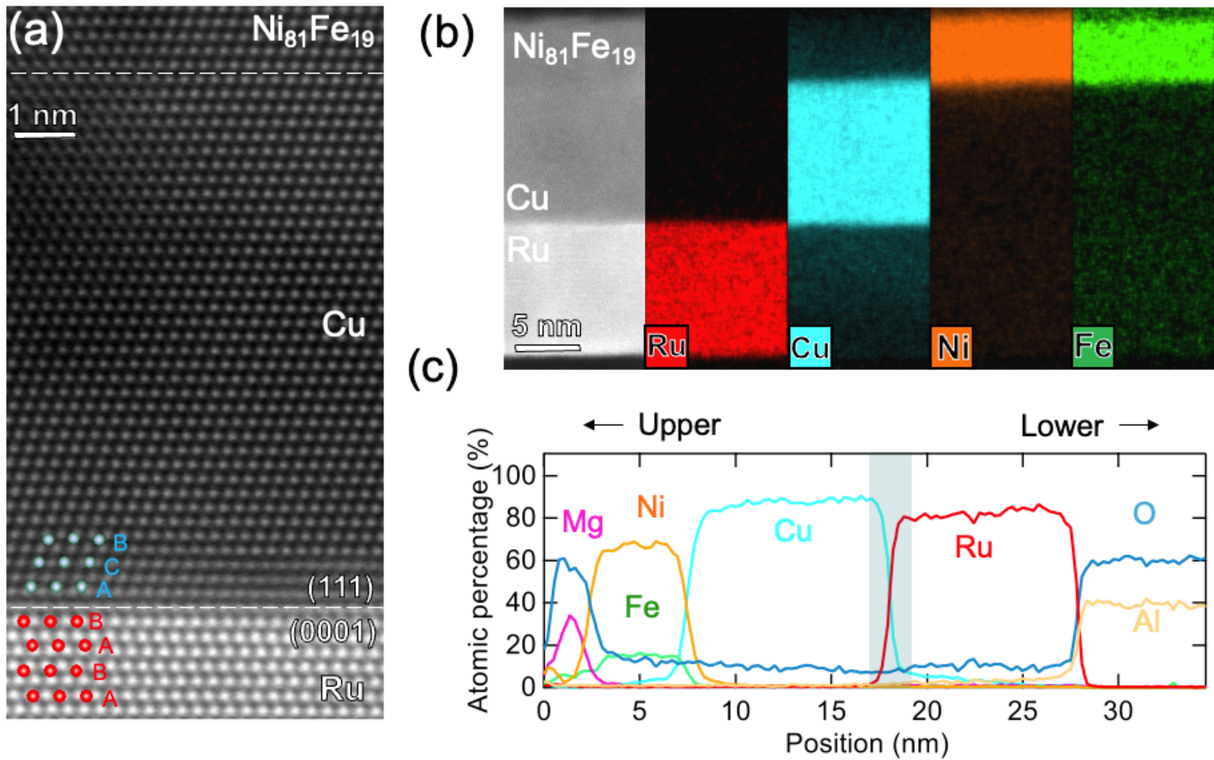

Figure 5.3 (a) Cross-sectional HAADF-STEM images. (b) EDS elemental maps and (c) elemental depth profiles for Al_2O_3 substrate//Ru (10nm)/Cu (10nm)/$Ni_{81}Fe_{19}$ (5nm)/MgO (2nm) stack.

To analyze the microstructure of the films, HAADF-STEM observations were conducted for the Ru/Cu heterostructures with a [Cu (1 nm)/Ru (1 nm)]$_n$ (n = 0, 1) nanolayer insertion along the $Al_2O_3[10\bar{1}0]$ direction. The cross-sectional HAADF-STEM image in Fig. 5.3(a) shows the microstructure of Al_2O_3 substrate//Ru (10 nm)/Cu (10 nm)/NiFe (5 nm)/MgO (2 nm) stack with no nanolayer insertion, displaying the atomic-resolution structure at Ru/Cu/NiFe interfaces. An

atomically sharp interface was observed between Ru and Cu layers where typical stacking sequences of hcp-structured ABAB and fcc-structured ABCABC were clearly shown for Ru and Cu layers, respectively. As for the Cu/NiFe interface, a perfect lattice matching (no misfit dislocation) was achieved between the Cu and NiFe layers. The EDS elemental maps and element depth profiles are shown in Figs. 5.3(b) and 5.3(c). These results confirmed the high quality of the film growth, i.e., sharp interfaces between different layers and no element interdiffusion occurred.

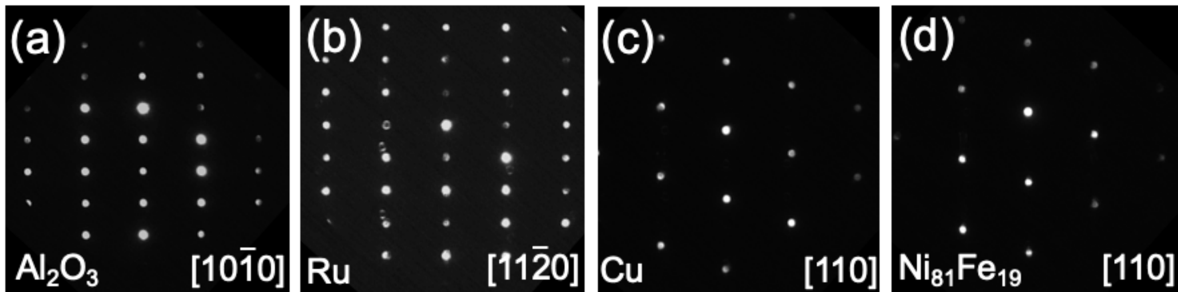

Figure 5.4 (a) NEBD patterns for Al_2O_3 layer, (b) Ru layer, (c) Cu layer, and (d) $Ni_{81}Fe_{19}$ layer of Al_2O_3 substrate//Ru (10nm)/Cu (10nm)/$Ni_{81}Fe_{19}$ (5nm)/MgO (2nm).

Figures 5.4(a-d) display the NBED patterns of each layer, which are collected along the orientation of $Al_2O_3[10\bar{1}0]$, Ru$[11\bar{2}0]$, Cu[110], and NiFe[110], respectively. This identified the epitaxial relationship which is consistent with the RHEED observations shown in the previous graphs and the illustration as we design these stacks.

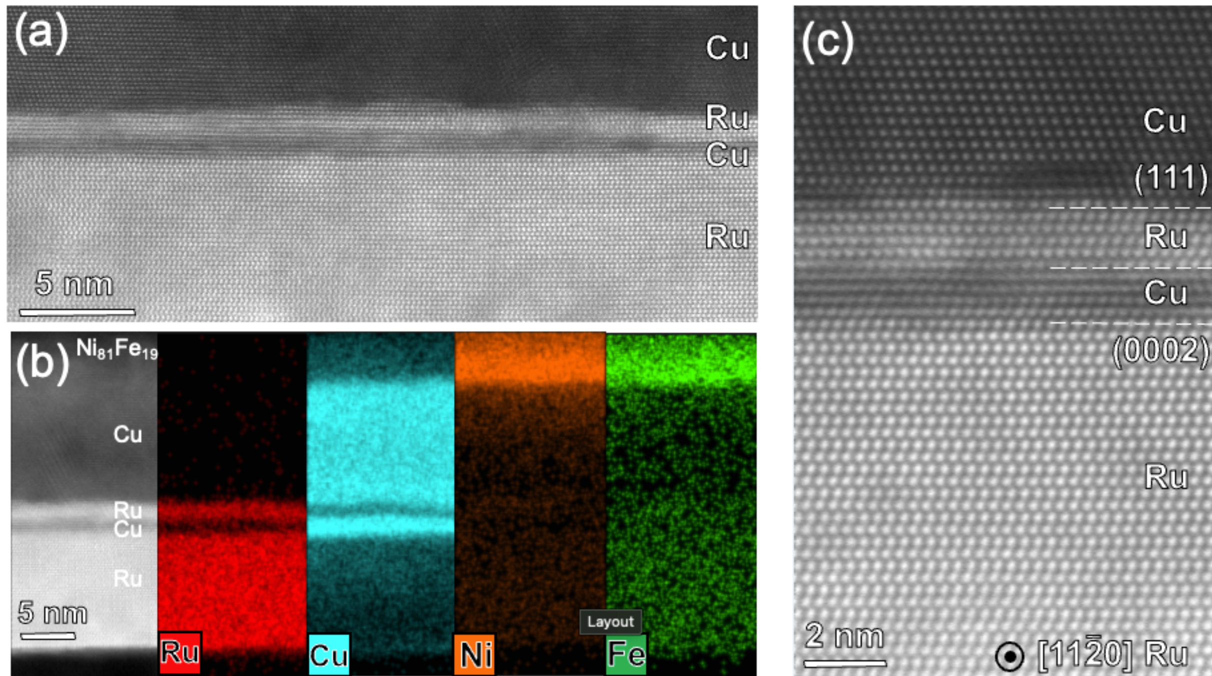

Figure 5.5 (a) Cross-sectional HAADF-STEM images for Al_2O_3 substrate//Ru (9nm)/Cu (1nm)/Ru (1nm)/Cu (9nm)/$Ni_{81}Fe_{19}$ (5nm)/MgO (2nm). (b) EDS elemental maps. (c) Magnified HAADF-STEM image near the Ru (1nm)/Cu (1nm) interface.

Microstructure characterization of Al_2O_3//Ru (9 nm)/[Cu (1 nm)/Ru (1 nm)]$_1$/Cu (9 nm)/NiFe (5 nm)/MgO (2 nm) sample where n = 1 with one nanolayer insertion was shown in Fig. 5.5. The relative flat interfaces between or inside the [Cu (1 nm)/Ru (1 nm)]$_1$ nanolayer can be observed in Fig. 5.5(a) from bottom to top. The alternate structure of the [Cu (1 nm)/Ru (1 nm)]$_1$ nanolayer can also be observed in the EDS elemental maps in Fig. 5.5(b) without interdiffusion occurring. The corresponding NBED patterns of each layer are shown in Figs. 5.6(a-d). These patterns demonstrate that the epitaxial relationship and crystallinity remained nearly similar to the Ru (10 nm)/Cu (10 nm) stack without nanolayer insertion.

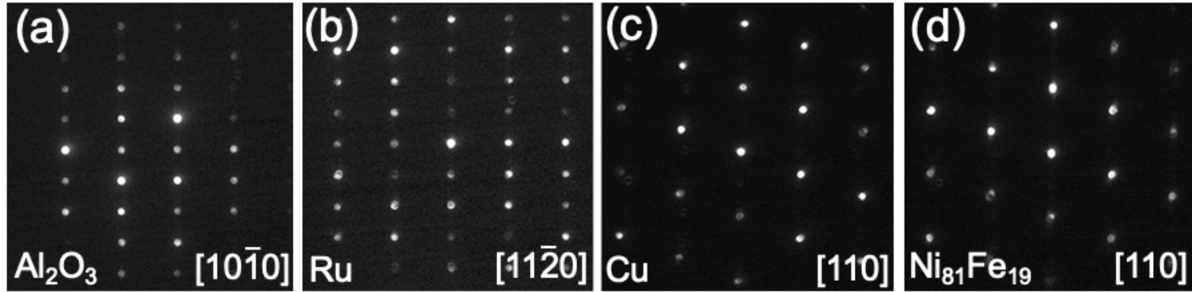

Figure 5.6 (a) NEBD patterns for Al_2O_3 layer, (b) Ru layer, (c) Cu layer, and (d) $Ni_{81}Fe_{19}$ layer of Al_2O_3 substrate//Ru (9nm)/Cu (1nm)/Ru (1nm)/Cu (9nm)/$Ni_{81}Fe_{19}$ (5nm)/MgO (2nm).

A magnified HAADF-STEM is shown in Fig. 5.5(c) to reveal the detailed atomic-scale structure at the multilayered Ru/Cu interfaces. Although the bulk lattice mismatch between Ru and Cu is 5.47%, the Ru/Cu interface was relatively sharp and distinguishable with a detectable stacking sequence of ABCABC for Cu and ABAB for Ru. It is suggested that the bottom Ru was well-grown which serves as a foundation for the flatness and epitaxial growth of the film. After inserting the nanolayer structure, the top Cu layer kept a single crystal growth mode continuously, similar to the Ru (10 nm)/Cu (10 nm) stack. By forming this well-controlled sample series, we may discuss the contribution from the [Cu (1 nm)/Ru (1 nm)]$_n$ insertion nanolayers in the following spin-transport measurements.

5.3.2 USMR measurement

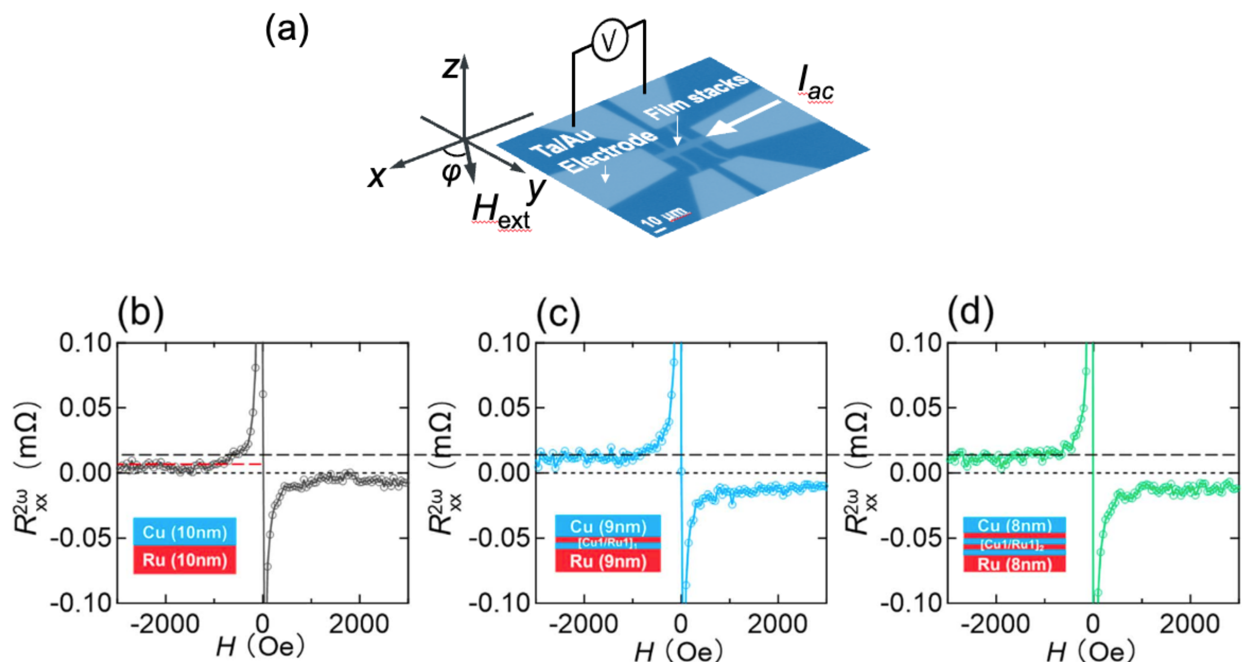

Figure 5.7 (a) Measurement setup for the unidirectional spin Hall magnetoresistance (USMR) with the microscope image of a Hall bar device. (b) Current dependence of normalized resistance $\Delta R_{xx(USMR)}^{2\omega}/R$. (c) $R_{xx}^{2\omega}$ for Ru (10nm)/Cu (10nm), Ru (9nm)/[Cu (1nm)/Ru (1nm)]$_1$/Cu (9nm) and (d) Ru (8nm)/[Cu (1nm)/Ru (1nm)]$_2$/Cu (8nm) measured during a field sweep along *y* direction with a current density $j = 1.4 \times 10^7$ A cm^{-2}.

For detecting the generation of spin current, we performed the second harmonic measurements to evaluate the USMR effect in the Ru/Cu samples on patterned Hall bar structures. The experimental configuration setup is shown in Fig. 5.7(a). The USMR effect is a phenomenon arising from the spin accumulation at the NM/FM interface with parallel or antiparallel alignment between the direction of spin polarization of the spin current and the magnetization direction of the FM layer.[71,72] This effect can be used for identifying the generation of spin current from the NM layer. In Figs. 5.7(b-d), the second harmonic components of the longitudinal resistance ($R_{xx}^{2\omega}$) measured at a constant current density $j = 1.4 \times 10^7$ A cm^{-2} are shown for the three samples of Ru/[Cu(1 nm)/Ru (1 nm)]$_n$ ($n = 0, 1, 2$)/Cu, respectively with insertion layer 0, 1 and 2. Here we can see that the $R_{xx}^{2\omega}$

signal was saturated when the field exceeds 1000 Oe. And the peaks near zero fields that jumped were attributed to the multidomain structures. [71] It is observed that the interface-engineered samples (n = 1, 2) in Figs. 5.7(c) and 5.7(d) have a much larger difference in $R_{xx}^{2\omega}$ between positive and negative saturation magnetic fields, compared to the Ru (10 nm)/Cu (10 nm) sample without an insertion layer shown in Fig. 5.7(b).

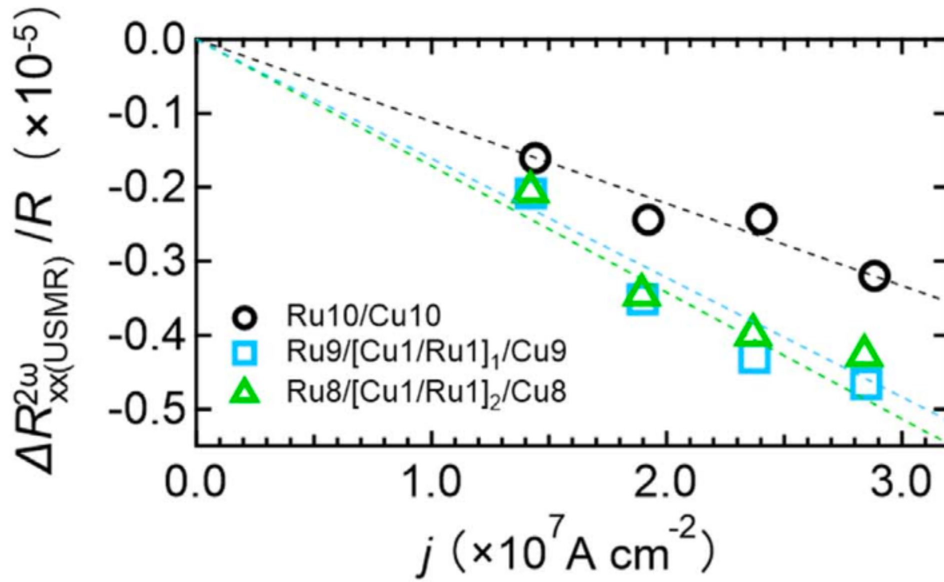

Figure 5.8 Charge current density dependence of $\Delta R_{xx(\mathrm{USMR})}^{2\omega}/R$.

As we mentioned in chapter 2.4.3, by measuring the transverse second-harmonic resistance component ($R_{xy}^{2\omega}$), the anomalous Nernst effect (ANE) which has the same angular dependence as the USMR signal and was subtracted from the $R_{xx}^{2\omega}$, then we can obtain the extracted USMR signal $R_{xx(\mathrm{USMR})}^{2\omega}$. The relative resistance difference $\Delta R_{xx(\mathrm{USMR})}^{2\omega}$ can be defined as follows,

$$\Delta R_{xx(\mathrm{USMR})}^{2\omega} = R_{xx(\mathrm{USMR})}^{2\omega}(\pm\boldsymbol{M}, \pm\boldsymbol{j}) - R_{xx(\mathrm{USMR})}^{2\omega}(\pm\boldsymbol{M}, \mp\boldsymbol{j}). \quad (1)$$

Then the current density dependence of a USMR ratio, i.e., $\Delta R_{xx(\mathrm{USMR})}^{2\omega}/R$, is shown in Fig. 5.8. The experimental data for the three stacks are well fitted to a linear response, which indicates that

in Ru/Cu samples, the USMR signal arises from a spin-dependent accumulation at the vicinity of the interface. This result indicates that although there are weak SOIs of both Ru and Cu, it is clear that the spin current can be generated in these Ru/Cu samples.

For the three samples of Ru/[Cu (1 nm)/Ru (1 nm)]$_n$ (n = 0, 1, 2)/Cu, the slopes of the fitting lines are –0.11, –0.17, and –0.16 ($\times10^{-12}$A cm^{-2}), respectively. In comparison with the value of -1.9×10^{-12}A cm^{-2} in the Pt/NiFe sample [74], the USMR signal of the RuCu samples is relatively small. Nevertheless, the stacks with inserted Cu (1 nm)/Ru (1 nm) nanolayers have larger slope values than the sample without insertion, indicating that the Cu/Ru nanolayer insertion improved the spin-charge conversion efficiency.

5.3.3 ST-FMR measurement

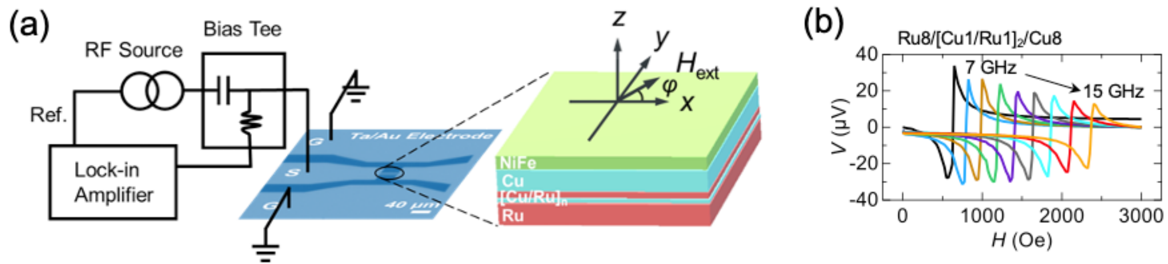

Figure 5.9 (a) Measurement setup for the ST-FMR for the Ru/[Cu/Ru]$_n$/Cu/$Ni_{81}Fe_{19}$ structure. (b) ST-FMR spectra with frequency f varies from 7–15 GHz with φ = 45° for Ru (8nm)/[Cu (1nm)/Ru (1nm)]$_2$/Cu (8nm) sample.

We further measured the ST-FMR signal to quantitively identify the efficiency of the spin current generation in this chapter. Figure 5.9(a) shows the experimental setup for a rectangular Ru/Cu thin film device integrated with a Ta/Au coplanar waveguide with an RF current applied to the device, resulting in an oscillating transverse spin current.

The detailed ST-FMR effect can be simply explained as follows. The spin current exerts spin-orbital torques on the magnetization of the FM layer, which leads to the FMR occurring. Then a DC voltage can be induced by the ST-FMR due to the anisotropic magnetoresistance (AMR) effect of the FM layer. The generated DC voltage has two mixed contributions, including a symmetric Lorentzian line shape component (V_S), and an antisymmetric Lorentzian line shape component (V_A) derived by the following equation, [55]

$$V = V_S \frac{\Delta^2}{(H-H_{res})^2+\Delta^2} + V_A \frac{\Delta(H-H_{res})}{(H-H_{res})^2+\Delta^2} + C, \quad (2)$$

where, V_S is related to the damping-like (DL) SOT from the oscillating spin current and V_A is related to the Oersted field and the field-like (FL) spin torque. Δ is the resonance linewidth, H_{res} is the resonance field, and C is a constant representing the offset for the voltage. In Fig. 5.9(b), clear resonance spectra are observed in the magnetic field dependence of voltage value with different frequency f varied from 7 GHz to 15 GHz at $\varphi = 45°$ for the Ru (8 nm)/[Cu (1 nm)/Ru (1 nm)]$_2$/Cu (8 nm) sample. The resonance field increases with the increase in frequency.

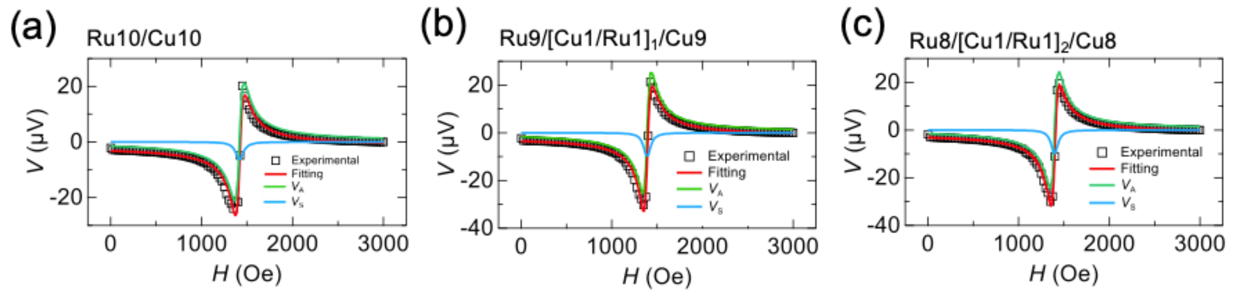

Figure 5.10 (a) Representative ST-FMR spectra (φ = 45° and f = 11 GHz), (b) extracted H_{res} for 8–15 GHz, (c) φ dependence of V_S and V_A for Ru (10nm)/Cu (10nm) stack.

Detailed fitting results of the voltage value based on Eq. (2) are plotted in Fig. 5.10(a-c) with the condition of frequency f = 11 GHz for the three samples, respectively. A negative V_S signal was

observed for each sample which is in agreement with the USMR results shown in the previous chapter.

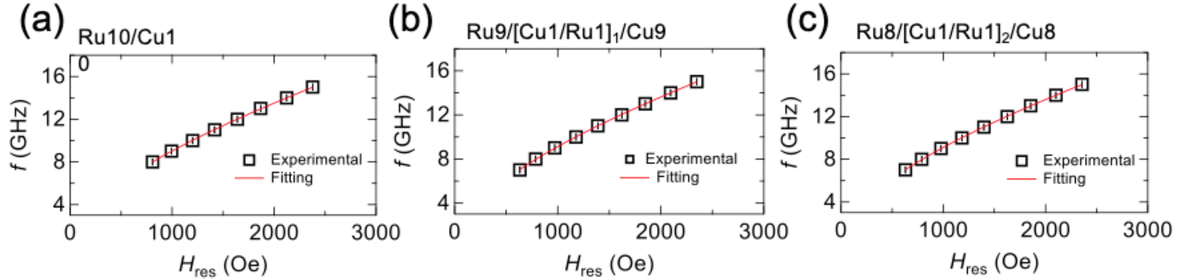

Figure 5.11 (a) Representative ST-FMR spectra (φ = 45° and f = 11 GHz), (b) extracted H_{res} for 7–15 GHz, (c) φ dependence of V_S and V_A for Ru (9nm)/[Cu (1nm)/Ru (1nm)]$_1$/Cu (9nm) stack.

In Figs. 5.11(a-c), here, the Kittel formula is shown:

$$f = (\gamma/2\pi)[(H_{\rm res} + H_{\rm ani})(H_{\rm res} + 4\pi M_{\rm eff})]^{1/2} \quad (3)$$

This equation was used to fit the results between the frequency f and the resonance field H_{res} extracted from the V-H curves at different frequencies. Here, γ is the gyromagnetic ratio, H_{ani} is the in-plane anisotropy field, and $4\pi M_{eff}$ represents the effective demagnetization field.

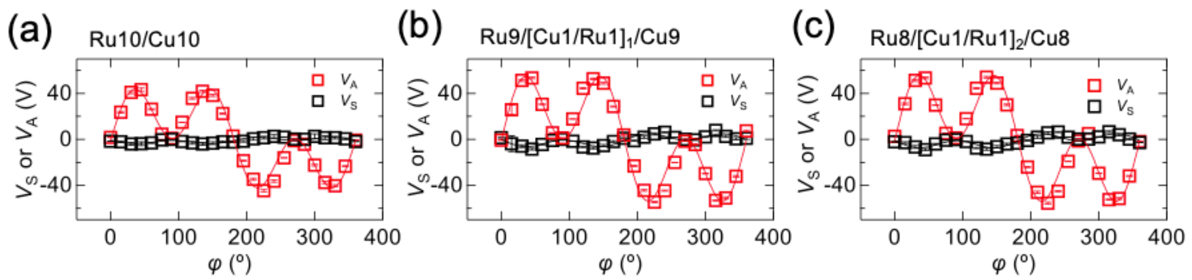

Figure 5.12 (a) Representative ST-FMR spectra (φ = 45° and f = 11 GHz), (b) extracted H_{res} for 7–15 GHz, (c) φ dependence of V_S and V_A for Ru (8nm)/[Cu (1nm)/Ru (1nm)]$_2$/Cu (8nm) stack.

Then the in-plane angular dependence measurements with fixed f = 11 GHz were also performed for the three stacks and shown in Figs. 5.12(a-c). The V_S (V_A) signal was fitted with the relationship

of $\sin2\varphi\cos\varphi$. With the ratio value from V_S/V_A, the effective spin Hall efficiency can be given by the following equation: [105]

$$\xi_{\mathrm{STFMR}} = \frac{V_S}{V_A}\frac{e\mu_0 M_s t_{\mathrm{NiFe}} t_{\mathrm{RuCu}}}{\hbar}\sqrt{\frac{H_{\mathrm{res}}+4\pi M_{\mathrm{eff}}}{H_{\mathrm{res}}+H_{\mathrm{ani}}}}, \quad (4)$$

where the μ_0 is the vacuum permeability. This equation was often used in several bilayer systems. As for this study, the Ru/Cu multilayer structure of the NM layer with interface engineering can be treated as a single layer. Therefore, using this equation will not lose the certainty for making comparisons among the three samples.

Further evaluation of the field-like (FL) and damping-like (DL) distinguishment is necessary to determine the appropriate value of the effective spin Hall efficiency. The FM thickness dependence of ST-FMR signals can be used to separate the DL component (ξ_{DL}) and FL component (ξ_{FL}) by following this equation:

$$\frac{1}{\xi_{\mathrm{STFMR}}} = \frac{1}{\xi_{\mathrm{DL}}}\left(1+\frac{\hbar}{e}\frac{\xi_{\mathrm{FL}}}{\mu_0 M_s t_{\mathrm{RuCu}} t_{\mathrm{NiFe}}}\right), \quad (5)$$

The fitting results with linear response are shown in Fig. 5.13. The ξ_{DL} can be obtained from the y-axis intercept and the ξ_{FL} can be evaluated from the slope of the fitted curves. [105,106]

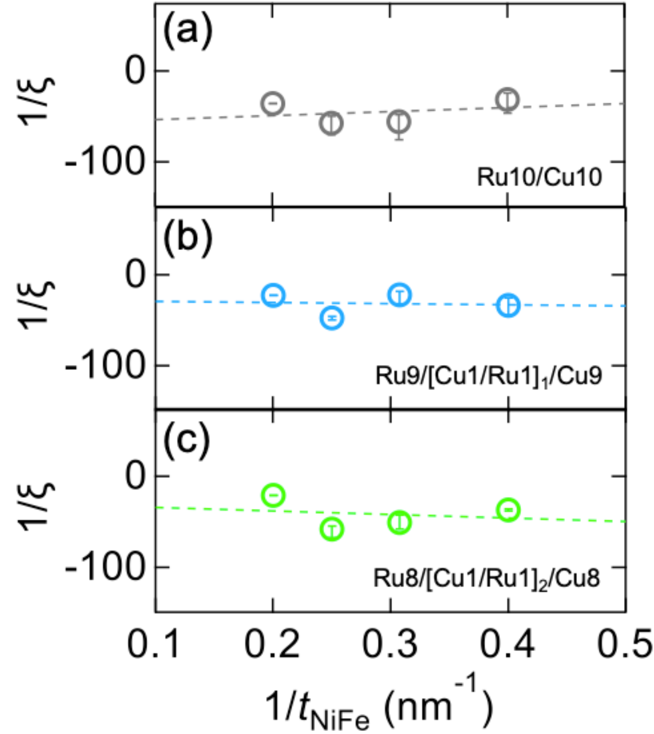

Figure 5.13 Inverse ξ as a function of inverse NiFe thickness for (a) Ru (10nm)/Cu (10nm), (b) Ru (9nm)/[Cu (1nm)/Ru (1nm)]$_1$/Cu (9nm) and (c) Ru (8nm)/[Cu (1nm)/Ru (1nm)]$_2$/Cu (8nm) stacks.

Thus, we determine the ξ_{DL} and ξ_{FL} of each stack and summarized the values with the longitudinal conductivity (σ_{xx}) and the effective spin Hall conductivity (σ_{SH}) in Table 5.2. The values for Pt from a reference are also shown for comparison and the discussion is in the next chapter.

Sample structure (nm)	ξ_{DL} (%)	ξ_{FL} (%)	σ_{xx} (Ω^{-1} m^{-1})	σ_{SH} ($\frac{\hbar}{2e}\Omega^{-1}$ m^{-1})
Ru(10)/Cu(10)	−2.2	0.5	176.5×10^5	−3.9×10^5
Ru(9)/[Cu(1)/Ru(1)]$_1$/Cu(9)	−3.6	1.4	133.1×10^5	−4.8×10^5
Ru(8)/[Cu(1)/Ru(1)]$_2$/Cu(8)	−3.7	5.9	127.4×10^5	−4.7×10^5
Pt ([55])	8	-	42×10^5	3.4×10^5

Table 5.2. Summary of the effective damping-like (ξ_{DL}) and field-like (ξ_{FL}) spin Hall efficiencies, longitudinal conductivity σ_{xx}, and the effective spin Hall conductivity σ_{SH} in this study and Pt from [55].

5.3.4 Discussion

Here, we focus on the impact of interface control on the charge-to-spin conversion efficiency in the samples. We compare the trends and relative changes in the effective spin Hall efficiency of three systems associated with different engineered interfaces. From Table 5.1, when there is no insertion layer, the effective damping-like spin Hall efficiency of the Ru (10 nm)/Cu (10 nm) sample is determined to be −2.2%, which is much larger than the reference value of +0.6% of a single Ru layer [98] and the negligible value (~0%) from a single Cu layer [74]. To explain the mechanism of this phenomenon, given it is a bilayer structure with a sharp interface, the sizeable ξ_{DL} could originate from the interfacial spin-orbit effects. Due to the weak bulk SOIs of Ru and Cu material, no significant Rashba effect at the Ru/Cu interface has been reported. Another interface effect, known as the spin-orbit filtering effect, [102,103] may play an important role in the spin current generation at the Ru/Cu interface. The spin-orbit filtering effect describes that the incoming unpolarized carriers can become spin-polarized through the spin-dependent reflection and transmission at the interface. Moreover, recent work reported that the sign of the spin current from the spin-orbit filtering effect is related to the magnitude of the charge current in the two interface materials. [104] The resistivities of the Ru (10 nm) layer and Cu (10 nm) layer in this study are about 9.4 and 3.8 μΩ·cm, respectively. So the charge current in the top Cu layer is more than two times higher than that in the lower Ru layer, leading to a spin current with a negative sign in the spin filtering process at the Ru/Cu interface.

As for the [Cu (1 nm)/Ru (1 nm)]$_n$ nanolayer-inserted stacks, the ξ_{DL} values are −3.6% and −3.7% for $n = 1$ and 2, respectively. Inserting the nanolayer increases the ξ_{DL} in the Ru/Cu heterostructure by almost 1.7 times while additional repetitions do not notably enhance it further. The reason behind this lack of enhancement can be explained by the interfacial effect in symmetrically

successive Ru/Cu and Cu/Ru structures, which can cancel each other out. As a result, increasing the repetition numbers of interfaces does not significantly impact the efficiency of spin-charge conversion. The observed increase in ξ_{DL} following the nanolayer insertion may result from the contributions of the intrinsic spin Hall effect, which is induced by the alterations in the local electronic structures. [101] The lattice distortions that arise in the nano-inserted layers due to the lattice mismatch between Ru and Cu (~5.5%) can potentially influence the local band electronic structures near the interface. The field-like spin Hall efficiency also increases from 0.5% to 5.9% with the interface-engineered sample, which could be attributed to the change in spin-dependent disorder scattering in the samples. [107] The effective damping-like spin Hall conductivity for each stack is determined to be -3.9×10^5, -4.8×10^5, and -4.7×10^5 $\frac{\hbar}{2e}\Omega^{-1}\mathrm{m}^{-1}$ for n = 0, 1, and 2, respectively, as presented in Table 1. The substantial effective spin Hall conductivities, which are comparable to that found in Pt, [55] may have significant implications for the development of spintronic devices.

5.4 Summary

In this chapter, fully epitaxial Ru/Cu multilayers were fabricated with interface-controlled structures by nanolayer insertion. Then the spin-charge conversion in these systems was studied. The atomically resolved microstructures of the Ru/Cu layers and their interfaces were confirmed through STEM observation, and the epitaxial growth was confirmed even with the insertion of the Cu/Ru nanolayers. The spin current generation was characterized by USMR measurements, where a linear response from the current density dependence of the USMR ratio was observed. The quantitative evaluation was further performed by the ST-FMR method and the damping-like and field-like components were evaluated by the thickness dependence of the NiFe layer as a

ferromagnetic layer. The effective damping-like efficiencies of spin-charge conversion of these sample stacks were achieved to be −2.2% to −3.7% for [Cu (1 nm)/Ru (1 nm)]$_n$ nanolayer insertion stacks with n varying from 0 to 2. The interfacial spin-orbit filtering effect could explain the spin current generated at the sharp Ru/Cu interface sample, and the local band structure tuning involved in the lattice distortion of the Cu/Ru nanolayer insertions further improved the effective spin Hall efficiencies. The effective spin Hall conductivities of these film stacks are characterized by the value of 3~5 $\times 10^5 \frac{\hbar}{2e} \Omega^{-1} m^{-1}$, which is as large as that value of Pt. A high conductivity application utilizing a common material system has been established, which may significantly enhance the development of SOT-MRAM technology.

Chapter 6 Summary and Outlook

Towards the development of next-generation memory systems with the nonvolatile candidate MRAM, MTJ, and SOT devices concerns of data reading and writing are important keys desired great efforts to study. In this thesis, we demonstrated both MTJ and SOT devices based on high-quality hcp Ru underlayer on single crystal sapphire substrate with epitaxial fcc (111) materials including CoFe/Mg-Al-O/CoFe, CoPt/MgO, and Ru/Cu material system. The main part is the first demonstration of fcc (111) MTJ with carefully engineered layer structure and optimized growth condition under the guidance of a novel interfacial resonant tunneling mechanism which predicts a giant TMR value and a strong bulk PMA effect. In this thesis, we studied the MTJ and SOT thin films and devices towards better performance SOT-MRAM application.

For MTJ development, an fcc(111)-type MTJ using a fully epitaxial $Co_{90}Fe_{10}$ (CoFe)/$Mg_4Al\text{-}O_x$ (MAO)/CoFe structure with flat interfaces were observed with periodic misfit dislocations at CoFe/MAO interface to minimize their large lattice mismatch (~20%). A TMR ratio of 37% at RT (47% at 10 K) was observed along with the symmetric TMR-*H* curves indicating the well-balanced CoFe/MAO interface. This is the first demonstration of a fully fcc (111) MTJ structure. The small TMR ratios suggest our MTJ does not show significant TMR enhancement due to the novel interfacial resonance tunneling mechanism. Nevertheless, our TMR demonstration is a fundamental study towards further fcc (111) MTJ development.

For downscaling below 10nm for industrial applications, perpendicular MTJ is desirable and the misfit dislocation needs to be reduced by reducing lattice mismatch between FM and barrier. Then the multilayered CoPt with different Pt concentrations was characterized and the peak splitting indicated the non-integer monolayer controlled structure. PMA energy up to 1 MJ/m^3 was achieved

at high deposition pressure. Based on the atomically flat surface structure and high crystallinity of the bottom CoPt multilayer, the CoPt(111)/MgO(111)/CoFeB perpendicular MTJ was fabricated with 24% MR observed, and a flat AP state due to the small coercivity from the top CoFeB PMA layer. Further, a fully perpendicular fcc (111) MTJ with CoPt/MgO/CoPt(111) was achieved with a bottom-SAF structure, and a 15% TMR was observed.

For the SOT device, fully epitaxial Ru/Cu heterostructures were fabricated with interface engineering structure and nanolayer insertions. The Ru/Cu film with a sharp interface has a sizeable ξ_{DL} of −2.2% due to the interface spin-orbit filtering effect. The insertion of Cu/Ru nanolayers increases the ξ_{DL} value further to −3.7% due to the intrinsic contribution from the local electronic structure tuning of the lattice distortion near the interface. A large effective spin Hall conductivity is achieved to be $(3\sim5)\times10^5$ $\hbar/2e$ $\Omega^{-1}m^{-1}$, which is in the same region as that of platinum.

This research demonstrates the novel fcc (111) MTJ in an experiment with technically engineered layer structure and precisely controlled deposition process and the characterization of flatness, crystallinity, microstructure, and transport properties were well established which path the promising future of TMR development beyond the conventional bcc (001) MTJ. The SOT study with an engineered nanolayer structure also expands the current study toward the next level of SOT-MRAM application.

Reference

1. Yuasa, S. & Djayaprawira, D. D. Giant tunnel magnetoresistance in magnetic tunnel junctions with a crystalline MgO(0 0 1) barrier. *J. Phys. D: Appl. Phys.* **40**, R337–R354 (2007).
2. Hirohata, A. *et al.* Review on spintronics: Principles and device applications. *J. Magn. Magn. Mater.* **509**, 166711 (2020).
3. Swagten, H. J. M. Chapter One Spin-Dependent Tunneling in Magnetic Junctions. in *Handbook of Magnetic Materials* vol. 17 1–121 (Elsevier, 2007).
4. Bhatti, S. *et al.* Spintronics based random access memory: a review. *Mater. Today* **20**, 530–548 (2017).
5. Binasch, G., Grünberg, P., Saurenbach, F. & Zinn, W. Enhanced magnetoresistance in layered magnetic structures with antiferromagnetic interlayer exchange. *Phys. Rev. B* **39**, 4828–4830 (1989).
6. Baibich, M. N. *et al.* Giant Magnetoresistance of (001)Fe/(001)Cr Magnetic Superlattices. *Phys. Rev. Lett.* **61**, 2472–2475 (1988).
7. Moodera, J. S., Kinder, L. R., Wong, T. M. & Meservey, R. Large Magnetoresistance at Room Temperature in Ferromagnetic Thin Film Tunnel Junctions. *Phys. Rev. Lett.* **74**, 3273–3276 (1995).
8. Julliere, M. Tunneling between ferromagnetic films. *Phys. Lett. A* **54**, 225–226 (1975).
9. Chappert, C., Fert, A. & Van Dau, F. N. The emergence of spin electronics in data storage. in *Nanoscience and Technology* 147–157 (Co-Published with Macmillan Publishers Ltd, UK, 2009). doi:10.1142/9789814287005_0015.
10. Mazumdar, D. *et al.* Field sensing characteristics of magnetic tunnel junctions with (001) MgO tunnel barrier. *J. Appl. Phys.* **103**, 113911 (2008).
11. Masuda, K., Itoh, H. & Miura, Y. Interface-driven giant tunnel magnetoresistance in (111)-oriented junctions. *Phys. Rev. B* **101**, 144404 (2020).
12. Miyazaki, T. & Tezuka, N. Giant magnetic tunneling effect in Fe/Al_2O_3/Fe junction. *J. Magn. Magn. Mater.* **139**, L231–L234 (1995).
13. Wang, D., Nordman, C., Daughton, J. M., Qian, Z. & Fink, J. 70% TMR at room temperature for SDT sandwich junctions with CoFeB as free and reference Layers. *IEEE Trans. Magn.* **40**, 2269–2271 (2004).

14. Butler, W. H., Zhang, X.-G., Schulthess, T. C. & MacLaren, J. M. Spin-dependent tunneling conductance of Fe | MgO | Fe sandwiches. *Phys. Rev. B* **63**, 054416 (2001).
15. Mathon, J. & Umerski, A. Theory of tunneling magnetoresistance of an epitaxial Fe/MgO/Fe(001) junction. *Phys. Rev. B* **63**, 220403 (2001).
16. Yuasa, S., Fukushima, A., Nagahama, T., Ando, K. & Suzuki, Y. High Tunnel Magnetoresistance at Room Temperature in Fully Epitaxial Fe/MgO/Fe Tunnel Junctions due to Coherent Spin-Polarized Tunneling. *Jpn. J. Appl. Phys.* **43**, L588–L590 (2004).
17. Yuasa, S., Nagahama, T., Fukushima, A., Suzuki, Y. & Ando, K. Giant room-temperature magnetoresistance in single-crystal Fe/MgO/Fe magnetic tunnel junctions. *Nat. Mater.* **3**, 868–871 (2004).
18. Scheike, T. *et al.* Exceeding 400% tunnel magnetoresistance at room temperature in epitaxial Fe/MgO/Fe(001) spin-valve-type magnetic tunnel junctions. *Appl. Phys. Lett.* **118**, 042411 (2021).
19. Djayaprawira, D. D. *et al.* 230% room-temperature magnetoresistance in CoFeB/MgO/CoFeB magnetic tunnel junctions. *Appl. Phys. Lett.* **86**, 092502 (2005).
20. Yuasa, S., Suzuki, Y., Katayama, T. & Ando, K. Characterization of growth and crystallization processes in CoFeB/MgO/CoFeB magnetic tunnel junction structure by reflective high-energy electron diffraction. *Appl. Phys. Lett.* **87**, 242503 (2005).
21. Scheike, T., Wen, Z., Sukegawa, H. & Mitani, S. 631% room temperature tunnel magnetoresistance with large oscillation effect in CoFe/MgO/CoFe(001) junctions. *Appl. Phys. Lett.* **122**, 112404 (2023).
22. Sukegawa, H. *et al.* Enhanced tunnel magnetoresistance in a spinel oxide barrier with cation-site disorder. *Phys. Rev. B* **86**, 184401 (2012).
23. Scheike, T. *et al.* Chemical ordering and large tunnel magnetoresistance in $Co_2FeAl/MgAl_2O_4/Co_2FeAl(001)$ junctions. *Appl. Phys. Express* **9**, 053004 (2016).
24. Miura, Y., Muramoto, S., Abe, K. & Shirai, M. First-principles study of tunneling magnetoresistance in $Fe/MgAl_2O_4/Fe(001)$ magnetic tunnel junctions. *Phys. Rev. B* **86**, 024426 (2012).
25. Zhang, J., Zhang, X.-G. & Han, X. F. Spinel oxides: Δ_1 spin-filter barrier for a class of magnetic tunnel junctions. *Appl. Phys. Lett.* **100**, 222401 (2012).

26. Scheike, T., Wen, Z., Sukegawa, H. & Mitani, S. Enhanced tunnel magnetoresistance in Fe/Mg_4Al-O_x/Fe(001) magnetic tunnel junctions. *Appl. Phys. Lett.* **120**, 032404 (2022).
27. Dieny, B., Goldfarb, R. B. & Lee, K.-J. *Introduction to Magnetic Random-Access Memory*. (John Wiley & Sons, 2016).
28. Shiota, Y. *et al.* Evaluation of write error rate for voltage-driven dynamic magnetization switching in magnetic tunnel junctions with perpendicular magnetization. *Appl. Phys. Express* **9**, 013001 (2015).
29. Ikeda, S. *et al.* A perpendicular-anisotropy CoFeB–MgO magnetic tunnel junction. *Nat. Mater.* **9**, 721–724 (2010).
30. Igarashi, J. *et al.* Single-nanometer CoFeB/MgO magnetic tunnel junctions with high-retention and high-speed capabilities. *Npj Spintron.* **2**, 1–9 (2024).
31. Yakushiji, K. *et al.* Ultrathin Co/Pt and Co/Pd superlattice films for MgO-based perpendicular magnetic tunnel junctions. *Appl. Phys. Lett.* **97**, 232508 (2010).
32. Yakushiji, K., Kubota, H., Fukushima, A. & Yuasa, S. Perpendicular magnetic tunnel junctions with strong antiferromagnetic interlayer exchange coupling at first oscillation peak. *Appl. Phys. Express* **8**, 083003 (2015).
33. Tezuka, N. *et al.* Perpendicular Magnetic Tunnel Junctions With Low Resistance-Area Product: High Output Voltage and Bias Dependence of Magnetoresistance. *IEEE Magn. Lett.* **7**, 1–4 (2016).
34. Choi, J.-Y., Lee, D., Baek, J.-U. & Park, J.-G. Double MgO-based Perpendicular Magnetic-Tunnel-Junction Spin-valve Structure with a Top Co2Fe6B2 Free Layer using a Single SyAF [Co/Pt]n Layer. *Sci. Rep.* **8**, 2139 (2018).
35. Okamoto, S. *et al.* Chemical-order-dependent magnetic anisotropy and exchange stiffness constant of FePt (001) epitaxial films. *Phys. Rev. B* **66**, 024413 (2002).
36. Klemmer, T., Hoydick, D., Okumura, H., Zhang, B. & Soffa, W. A. Magnetic hardening and coercivity mechanisms in L10 ordered FePd ferromagnets. *Scr. Metall. Mater.* **33**, 1793–1805 (1995).
37. Mizukami, S. *et al.* Long-Lived Ultrafast Spin Precession in Manganese Alloys Films with a Large Perpendicular Magnetic Anisotropy. *Phys. Rev. Lett.* **106**, 117201 (2011).
38. Yang, H. X. *et al.* First-principles investigation of the very large perpendicular magnetic anisotropy at Fe | MgO and Co | MgO interfaces. *Phys. Rev. B* **84**, 054401 (2011).

39. Ikeda, S. *et al.* A perpendicular-anisotropy CoFeB–MgO magnetic tunnel junction. *Nat. Mater.* **9**, 721–724 (2010).
40. Hallal, A., Yang, H. X., Dieny, B. & Chshiev, M. Anatomy of perpendicular magnetic anisotropy in Fe/MgO magnetic tunnel junctions: First-principles insight. *Phys. Rev. B* **88**, 184423 (2013).
41. Yang, H. X. *et al.* First-principles investigation of the very large perpendicular magnetic anisotropy at Fe|MgO and Co|MgO interfaces. *Phys. Rev. B* **84**, 054401 (2011).
42. Hauch, J. O. *et al.* Fully epitaxial Fe(110)/MgO(111)/Fe(110) magnetic tunnel junctions: Growth, transport, and spin filtering properties. *Appl. Phys. Lett.* **93**, 083512 (2008).
43. Ohtake, M., Suzuki, D., Futamoto, M., Kirino, F. & Inaba, N. Preparation of L11-CoPt/MgO/L11-CoPt tri-layer film on Ru(0001) underlayer. *AIP Adv.* **6**, 056103 (2016).
44. Masuda, K. *et al.* Interfacial giant tunnel magnetoresistance and bulk-induced large perpendicular magnetic anisotropy in (111)-oriented junctions with fcc ferromagnetic alloys: A first-principles study. *Phys. Rev. B* **103**, 064427 (2021).
45. Waldron, D., Timoshevskii, V., Hu, Y., Xia, K. & Guo, H. First Principles Modeling of Tunnel Magnetoresistance of Fe/MgO/Fe Trilayers. *Phys. Rev. Lett.* **97**, 226802 (2006).
46. Rungger, I., Reily Rocha, A., Mryasov, O., Heinonen, O. & Sanvito, S. Electronic transport through Fe/MgO/Fe(100) tunnel junctions. *J. Magn. Magn. Mater.* **316**, 481–483 (2007).
47. Rungger, I., Mryasov, O. & Sanvito, S. Resonant electronic states and I-V curves of Fe/MgO/Fe(100) tunnel junctions. *Phys. Rev. B* **79**, 094414 (2009).
48. Song, J. *et al.* Fully epitaxial fcc(111) magnetic tunnel junctions with a $Co_{90}Fe_{10}$/MgAlO/$Co_{90}Fe_{10}$ structure. Preprint at https://doi.org/10.48550/arXiv.2308.04149 (2023).
49. Kato, Y. K., Myers, R. C., Gossard, A. C. & Awschalom, D. D. Observation of the Spin Hall Effect in Semiconductors. *Science* **306**, 1910–1913 (2004).
50. Valenzuela, S. O. & Tinkham, M. Direct electronic measurement of the spin Hall effect. *Nature* **442**, 176–179 (2006).
51. Cheng, L., Li, Z., Zhao, D. & Chia, E. E. M. Studying spin–charge conversion using terahertz pulses. *APL Mater.* **9**, 070902 (2021).
52. Shao, Q. *et al.* Roadmap of Spin–Orbit Torques. *IEEE Trans. Magn.* **57**, 1–39 (2021).

53. Han, X., Wang, X., Wan, C., Yu, G. & Lv, X. Spin-orbit torques: Materials, physics, and devices. *Appl. Phys. Lett.* **118**, 120502 (2021).
54. Liu, L. *et al.* Spin-Torque Switching with the Giant Spin Hall Effect of Tantalum. *Science* **336**, 555–558 (2012).
55. Liu, L., Moriyama, T., Ralph, D. C. & Buhrman, R. A. Spin-Torque Ferromagnetic Resonance Induced by the Spin Hall Effect. *Phys. Rev. Lett.* **106**, 036601 (2011).
56. Liu, L., Pai, C.-F., Ralph, D. C. & Buhrman, R. A. Magnetic Oscillations Driven by the Spin Hall Effect in 3-Terminal Magnetic Tunnel Junction Devices. *Phys. Rev. Lett.* **109**, 186602 (2012).
57. Li, R. *et al.* A spin–orbit torque device for sensing three-dimensional magnetic fields. *Nat. Electron.* **4**, 179–184 (2021).
58. Wen, Z. *et al.* Spin-charge conversion in NiMnSb Heusler alloy films. *Sci. Adv.* **5**, eaaw9337 (2019).
59. Garello, K. *et al.* Ultrafast magnetization switching by spin-orbit torques. *Appl. Phys. Lett.* **105**, 212402 (2014).
60. Tang, K. *et al.* Spin Hall effect in a spin-1 chiral semimetal. *Phys. Rev. Res.* **3**, 033101 (2021).
61. Tang, K., Wen, Z., Seki, T., Sukegawa, H. & Mitani, S. Elemental Doping and Interface Effects on Spin–Orbit Torques in CoSi-Based Topological Semimetal Thin Films. *Adv. Mater. Interfaces* 2201332 (2022) doi:10.1002/admi.202201332.
62. Kim, J. *et al.* Layer thickness dependence of the current-induced effective field vector in Ta|CoFeB|MgO. *Nat. Mater.* **12**, 240–245 (2013).
63. Suzuki, T. *et al.* Current-induced effective field in perpendicularly magnetized Ta/CoFeB/MgO wire. *Appl. Phys. Lett.* **98**, 142505 (2011).
64. Kim, J. *et al.* Anomalous temperature dependence of current-induced torques in CoFeB|MgO heterostructures with Ta-based underlayers. *Phys. Rev. B* **89**, 174424 (2014).
65. Emori, S., Bauer, U., Ahn, S.-M., Martinez, E. & Beach, G. S. D. Current-driven dynamics of chiral ferromagnetic domain walls. *Nat. Mater.* **12**, 611–616 (2013).
66. Miron, I. M. *et al.* Perpendicular switching of a single ferromagnetic layer induced by in-plane current injection. *Nature* **476**, 189–193 (2011).
67. Pi, U. H. *et al.* Tilting of the spin orientation induced by Rashba effect in ferromagnetic metal layer. *Appl. Phys. Lett.* **97**, 162507 (2010).

68. Pai, C.-F. *et al.* Spin transfer torque devices utilizing the giant spin Hall effect of tungsten. *Appl. Phys. Lett.* **101**, 122404 (2012).
69. Pai, C.-F. *et al.* Enhancement of perpendicular magnetic anisotropy and transmission of spin-Hall-effect-induced spin currents by a Hf spacer layer in W/Hf/CoFeB/MgO layer structures. *Appl. Phys. Lett.* **104**, 082407 (2014).
70. Worledge, D. C. & Trouilloud, P. L. Magnetoresistance measurement of unpatterned magnetic tunnel junction wafers by current-in-plane tunneling. *Appl. Phys. Lett.* **83**, 84–86 (2003).
71. Avci, C. O. *et al.* Unidirectional spin Hall magnetoresistance in ferromagnet/normal metal bilayers. *Nat. Phys.* **11**, 570–575 (2015).
72. Zhang, S. S.-L. & Vignale, G. Theory of unidirectional spin Hall magnetoresistance in heavy-metal/ferromagnetic-metal bilayers. *Phys. Rev. B* **94**, 140411 (2016).
73. Song, J. *et al.* Charge-to-spin conversion in fully epitaxial Ru/Cu hybrid nanolayers with interface control. *Nanotechnology* **34**, 365704 (2023).
74. Okano, G., Matsuo, M., Ohnuma, Y., Maekawa, S. & Nozaki, Y. Nonreciprocal Spin Current Generation in Surface-Oxidized Copper Films. *Phys. Rev. Lett.* **122**, 217701 (2019).
75. Ning, T., Yu, Q. & Ye, Y. Multilayer relaxation at the surface of fcc metals: Cu, Ag, Au, Ni, Pd, Pt, Al. *Surf. Sci.* **206**, L857–L863 (1988).
76. Yu, H. K. & Lee, J.-L. Growth Mechanism of MgO Film on Si (100): Domain Matching Epitaxy, Strain Relaxation, Preferred Orientation Formation. *Cryst. Growth Des.* **10**, 5200–5204 (2010).
77. Godel, F. *et al.* Epitaxy of MgO magnetic tunnel barriers on epitaxial graphene. *Nanotechnology* **24**, 475708 (2013).
78. Posadas, A. *et al.* Epitaxial MgO as an alternative gate dielectric for SiC transistor applications. *Appl. Phys. Lett.* **92**, 233511 (2008).
79. Nozaki, T., Konoto, M. & Nozaki, T. Control of the magnetic domain of Pt/Co/Ru/MgO multilayer: Effect of Co thickness and Ru insertion. *AIP Adv.* **10**, 035130 (2020).
80. Miceli, P. F., Palmstrøm, C. J. & Moyers, K. W. X-ray scattering study of lattice relaxation in ErAs epitaxial layers on GaAs. *Appl. Phys. Lett.* **58**, 1602–1604 (1991).
81. Ohtake, M., Yabuhara, O., Nukaga, Y. & Futamoto, M. Preparation of Co(0001)hcp and (111)fcc Films on Single-Crystal Oxide Substrates. *J. Phys. Conf. Ser.* **303**, 012016 (2011).

82. He, C. *et al.* Nano-crystal domains in Co-based fcc(111) epitaxial magnetic junctions and their impact on tunnel magnetoresistance. *Acta Mater.* **261**, 119394 (2023).
83. Belmoubarik, M., Sukegawa, H., Ohkubo, T., Mitani, S. & Hono, K. MgAl2O4 (001) based magnetic tunnel junctions made by direct sputtering of a sintered spinel target. *Appl. Phys. Lett.* **108**, 132404 (2016).
84. Zhang, S., Levy, P. M., Marley, A. C. & Parkin, S. S. P. Quenching of Magnetoresistance by Hot Electrons in Magnetic Tunnel Junctions. *Phys. Rev. Lett.* **79**, 3744–3747 (1997).
85. Drewello, V. *et al.* Inelastic electron tunneling spectra of MgO-based magnetic tunnel junctions with different electrode designs. *Phys. Rev. B* **79**, 174417 (2009).
86. Miao, G.-X. *et al.* Inelastic tunneling spectroscopy of magnetic tunnel junctions based on CoFeB/MgO/CoFeB with Mg insertion layer. *J. Appl. Phys.* **99**, 08T305 (2006).
87. Teixeira, J. M. *et al.* Electrode band structure effects in thin MgO magnetic tunnel junctions. *Appl. Phys. Lett.* **100**, 072406 (2012).
88. Ringer, S., Vieth, M., Bär, L., Rührig, M. & Bayreuther, G. Conductance anomalies of CoFeB/MgO/CoFeB magnetic tunnel junctions. *Phys. Rev. B* **90**, 174401 (2014).
89. Heiliger, C., Zahn, P., Yavorsky, B. Yu. & Mertig, I. Interface structure and bias dependence of Fe/MgO/Fe tunnel junctions: Ab initio calculations. *Phys. Rev. B* **73**, 214441 (2006).
90. Sukegawa, H. *et al.* Tunnel magnetoresistance with improved bias voltage dependence in lattice-matched Fe/spinel $MgAl_2O_4$/Fe(001) junctions. *Appl. Phys. Lett.* **96**, 212505 (2010).
91. Ikhtiar *et al.* Giant tunnel magnetoresistance in polycrystalline magnetic tunnel junctions with highly textured $MgAl_2O_4$(001) based barriers. *Appl. Phys. Lett.* **112**, 022408 (2018).
92. Sato, H. *et al.* Fabrication of L11 type Co-Pt ordered alloy films by sputter deposition. *J. Appl. Phys.* **103**, 07E114 (2008).
93. Mitani, S. *et al*. Coherent Layered Structures in Fe/Au Monatomic Multilayers with Addition of Fractional Atomic Layers. *Jpn. J. Appl. Phys.* **36**, L1045 (1997).
94. Bertero, G. A. & Sinclair, R. Structure-property correlations in Pt/Co multilayers for magneto-optic recording. *J. Magn. Magn. Mater.* **134**, 173–184 (1994).
95. An, H., Kageyama, Y., Kanno, Y., Enishi, N. & Ando, K. Spin–torque generator engineered by natural oxidation of Cu. *Nat. Commun.* **7**, 13069 (2016).
96. Wang, H. L. *et al.* Scaling of Spin Hall Angle in 3d, 4d, and 5d Metals from $Y_3Fe_5O_{12}$/Metal Spin Pumping. *Phys. Rev. Lett.* **112**, 197201 (2014).

97. Sinova, J., Valenzuela, S. O., Wunderlich, J., Back, C. H. & Jungwirth, T. Spin Hall effects. *Rev. Mod. Phys.* **87**, 1213–1260 (2015).

98. Wen, Z., Kim, J., Sukegawa, H., Hayashi, M. & Mitani, S. Spin-orbit torque in Cr/CoFeAl/MgO and Ru/CoFeAl/MgO epitaxial magnetic heterostructures. *AIP Adv.* **6**, 056307 (2016).

99. Gao, T. *et al.* Intrinsic Spin-Orbit Torque Arising from the Berry Curvature in a Metallic-Magnet/Cu-Oxide Interface. *Phys. Rev. Lett.* **121**, 017202 (2018).

100. Kageyama, Y. *et al.* Spin-orbit torque manipulated by fine-tuning of oxygen-induced orbital hybridization. *Sci. Adv.* **5**, eaax4278 (2019).

101. Jamali, M. *et al.* Spin-Orbit Torques in Co/Pd Multilayer Nanowires. *Phys. Rev. Lett.* **111**, 246602 (2013).

102. Amin, V. P., Zemen, J. & Stiles, M. D. Interface-Generated Spin Currents. *Phys. Rev. Lett.* **121**, 136805 (2018).

103. Baek, S. C. *et al.* Spin currents and spin–orbit torques in ferromagnetic trilayers. *Nat. Mater.* **17**, 509–513 (2018).

104. Choi, G. *et al.* Thickness Dependence of Interface-Generated Spin Currents in Ferromagnet/Ti/CoFeB Trilayers. *Adv. Mater. Interfaces* **9**, 2201317 (2022).

105. Pai, C.-F., Ou, Y., Vilela-Leão, L. H., Ralph, D. C. & Buhrman, R. A. Dependence of the efficiency of spin Hall torque on the transparency of Pt/ferromagnetic layer interfaces. *Phys. Rev. B* **92**, 064426 (2015).

106. Chen, T.-Y., Peng, C.-W., Liao, W.-B. & Pai, C.-F. Characterization of Spin-Orbit Torque Efficiency in the RF Regime for MRAM Applications. in *2021 IEEE International Symposium on Radio-Frequency Integration Technology (RFIT)* 1–6 (IEEE, Hualien, Taiwan, 2021). doi:10.1109/RFIT52905.2021.9565262.

107. Ando, K. Generation and manipulation of current-induced spin-orbit torques. *Proc. Jpn. Acad. Ser. B* **97**, 499–519 (2021).

List of publications and presentations

Publication

1. J. Song, C. He, T. Scheike, Z. Wen, H. Sukegawa, T. Ohkubo, Y. Nozaki, and S. Mitani Charge-to-spin conversion in fully epitaxial Ru/Cu hybrid nanolayers with interface control Nanotechnology. 34, 365704 (2023)
2. J. Song, T. Scheike, C. He, Z. Wen, T. Ohkubo, K. Hono, H. Sukegawa, and S. Mitani Fully epitaxial fcc(111) magnetic tunnel junctions with a $Co_{90}Fe_{10}$/MgAlO/$Co_{90}Fe_{10}$ structure Adv. Funct. Mater. (Submitted in Aug., 2024)
3. J. Song, T. Scheike, C. He, Z. Wen, T. Ohkubo, K. Kim, H. Sukegawa, and S. Mitani Incommensurate superlattice modulation surviving down to an atomic scale in sputter-deposited Co/Pt(111) epitaxial multilayered films APL Mater. (Submitted in Aug., 2024)
4. C. He, K. Masuda, J. Song, T. Scheike, Z. Wen, Y. Miura, T. Ohkubo, K. Hono, S. Mitani, and H. Sukegawa Nano crystal domains in Co-based fcc(111) epitaxial magnetic junctions: Impact on tunnel magnetoresistance of three types of domains Acta Mater. 261, 119394 (2023).

Presentation

1. J. Song, T. Scheike, C. He, Z. Wen, H. Sukegawa, T. Ohkubo, K. Hono and S. Mitani $Co_{90}Fe_{10}$/Mg-Al-O/$Co_{90}Fe_{10}$ “Magnetic tunnel junctions with a fully epitaxial fcc (111) structure” INTERMAG 2023, 2023
2. J. Song, T. Scheike, C. He, Z. Wen, T. Ohkubo, K. Kim, H. Sukegawa, and S. Mitani “Perpendicular Magnetic Tunnel Junctions with a Monoatomic-Layer-Controlled CoPt(111)

layer and a MgO(111) Barrier” The 68th Annual Conference on Magnetism and Magnetic Materials, 2023

3. J. Song, T. Scheike, C. He, Z. Wen, H. Sukegawa, T. Ohkubo, K. Hono and S. Mitani “Epitaxial (111) Barrier Magnetic Tunnel Junctions with Fcc-CoFe Electrodes” MRM2023/IUMRS-ICA2023 Grand Meeting, 2023
4. J. Song, T. Scheike, C. He, Z. Wen, H. Sukegawa, T. Ohkubo, K. Hono and S. Mitani “Fcc(111) epitaxial magnetic tunnel junctions with a $Co_{90}Fe_{10}$/Mg-Al-O/$Co_{90}Fe_{10}$ structure” The 69th JSAP spring meeting and The 83th JSAP Autum meeting, 2022

Acknowledgments

It is with great pleasure to acknowledge the invaluable support and guidance as a Junior Researcher at the University of Tsukuba-NIMS Joint Graduate School. First and foremost, I extend my sincerest gratitude to my supervisor, Prof. Seiji Mitani, for his invaluable support, insightful feedback, and kind guidance throughout my research life.

I am grateful to the members of my dissertation committee: Prof. Hideto Yanagihara, Prof. Seiji Mitani, Prof. Yoshihiko Takeda, Prof. Yuya Sakuraba, and Dr. Hiroaki Sukegawa. Their constructive feedback and fruitful discussions have significantly enhanced the quality of this work.

A special note of thanks goes to Dr. Hiroaki Sukegawa and Dr. Zhenchao Wen, whose assistance during my research life has been invaluable. They always gave me a lot of suggestion and guidance during every step of my research work no matter the experiment process or the preparation for slides and manucripts. I always enjoyed the discussion and always learn a lot from the comment from them.

I also wish to extend my heartfelt thanks to the members of the Spintronics Group: Dr. Thomas Scheike, Dr. Qingyi Xiang, Dr. Yuki Iida, Dr. Cong He, Dr. Kresna B. Fathoni, Ms. Hiromi Ikeda, Mr. Ke Tang, Mr. Rombang R. Sihombing, Mr. Tomoki Kanazawa, Ms. Mouli R. Chowdhury, Ms. Chika Shigaki, Ms. Naoko Yoshimoto, and Ms. Akiko Tomaru. Their collaboration, assistance, and suggestions have been crucial in both my research and administrative tasks.

In addition, I am deeply appreciative of the support from the collaborators of this work: Prof. Kazuhiro Hono, Dr. Tadakatsu Ohkubo, Dr Yoshio Miura, Dr. Keisuke Masuda, and Dr.

Kwangseok Kim. I am also deeply grateful for the support from other CMSM members who have contributed to my experiments and daily life.

Finally, I would like to acknowledge the financial support provided by the NIMS Junior Research Assistantship.